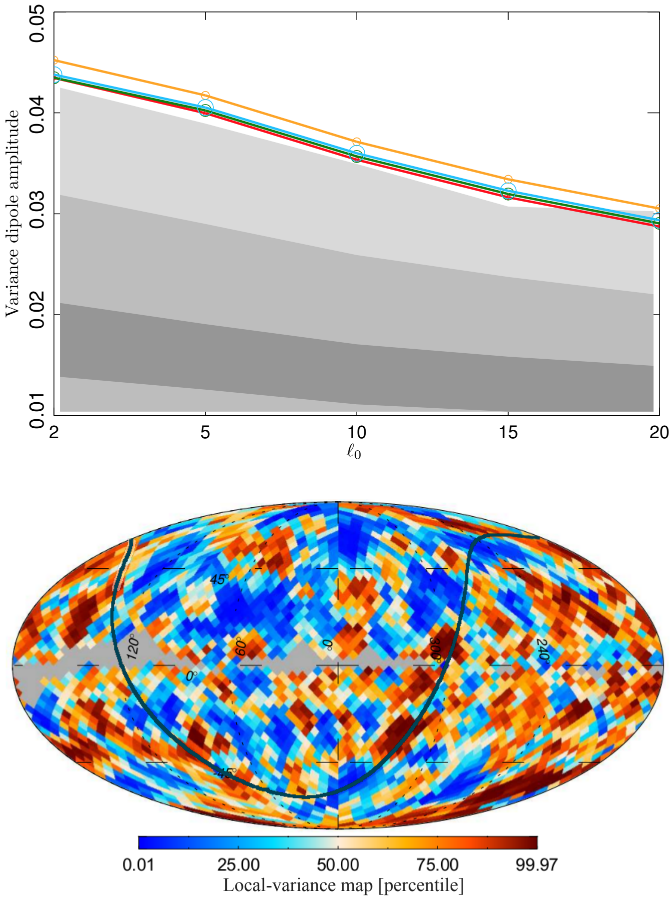

**Fig. 28.** *Upper panel*: local-variance dipole amplitude for 8° discs as a function of the central multipole of the high-pass filter, $\ell_0$, for the four component-separation methods, `Commander` (red), `NILC` (orange), `SEVEM` (green), and `SMICA` (blue). The grey regions, from dark to light, correspond, respectively, to $1\sigma$, $2\sigma$, and $3\sigma$ percentiles from the 1000 FFP8 simulations processed by the `Commander` method. *Lower panel*: mean-subtracted and inverse-variance-weighted local-variance map for the 8° discs and for the `Commander` component-separation method; each pixel is given in terms of the lower- and upper-tail probability of the measured value on that pixel compared to the values from the simulations. The pixels in grey correspond to the centres of the 8° discs on which the number of unmasked pixels in the full resolution map is lower than our threshold. The black curve superposed on the map indicates the boundary of the opposing hemispheres along the asymmetry axis. It is clear that the largest fraction of >95% outliers (red pixels) lie on the positive amplitude hemisphere of the local variance dipole, while the <5% outliers (blue pixels) are on the opposite hemisphere. The corresponding maps for `NILC`, `SEVEM`, and `SMICA` are very similar to the one shown here.

In the upper panel of Fig. 28, we show the local-variance dipole amplitudes for the 8° discs as a function of the central multipole of the high-pass filter, $\ell_0$. In the lower panel of the same figure we show, as an example, the mean-subtracted and inverse-variance-weighted local-variance map using 8° discs for the `Commander` component-separation method. The pixels of the map are given in terms of the lower- and upper-tail probabilities of the values from the data compared to the values from the simulations. The maps for `NILC`, `SEVEM`, and `SMICA` are very similar. The numerical values of the local-variance dipole amplitudes and directions for the `Commander` method are given in Table 21; the values for the `NILC`, `SEVEM`, and `SMICA` methods are similar.

**Table 21.** Local-variance dipole amplitudes and directions.

| $\ell_0$ | $A^a$ | Direction $(l, b)$ [°] |
|---|---|---|
| Unfiltered . . | $0.052 \pm 0.016$ | (210, −26) |
| 5 . . . . . . . . . | $0.046 \pm 0.014$ | (208, −24) |
| 10 . . . . . . . . | $0.040 \pm 0.014$ | (199, −16) |
| 15 . . . . . . . . | $0.038 \pm 0.012$ | (206, −16) |
| 20 . . . . . . . . | $0.028 \pm 0.010$ | (202, −18) |
| 30 . . . . . . . . | $0.025 \pm 0.010$ | (199, −19) |

**Notes.** All values quoted here are for 8° discs. This table is for the `Commander` component-separation method, but the results are similar for the other methods. $^{(a)}$ $A = 2(A_{\text{Planck}} - \langle A_{\text{FFP8}} \rangle)$, where $A_{\text{Planck}}$ and $A_{\text{FFP8}}$ are the local-variance dipole amplitudes of the data and the FFP8 simulations, respectively. The quoted errors are the dispersion of the simulation amplitudes. Assuming a pure dipole modulation model, $A$ to first order would correspond to the modulation amplitude.

### *6.2. Dipole modulation: pixel-based likelihood*

In PCIS13 we presented an analysis of the apparent anisotropic distribution of large-scale power in the *Planck* 2013 temperature data within the parametric framework defined by Gordon (2007) and Hoftuft et al. (2009), who introduced an explicit dipole modulation field to model potential hemispherical power asymmetry. The following is a direct update of that analysis using the *Planck* 2015 CMB data at $N_{\text{side}} = 32$, retaining the 2013 common mask to explicitly test for consistency with the earlier study. All results are found to be in excellent agreement. In the following, we therefore only consider a smoothing scale of 5° FWHM as a representative example. This is the highest angular resolution accessible for an $N_{\text{side}} = 32$ map.

Recall first the basic data model adopted in the dipole modulation approach: rather than assuming the CMB sky to be a statistically isotropic Gaussian field, we allow for an additional dipole modulation, resulting in a data model of the form $\boldsymbol{d} = \mathsf{BM}\boldsymbol{s} + \boldsymbol{n}$, where $\mathsf{M}_{\text{ij}} = (1 + \alpha\, \hat{\boldsymbol{p}} \cdot \hat{\boldsymbol{n}}_i)\delta_{ij}$ is an offset dipole field multiplying an intrinsically isotropic signal $\boldsymbol{s}$ with a dipole of amplitude $\alpha$ pointing towards some preferred direction $\hat{\boldsymbol{p}}$. $\mathsf{B}$ denotes convolution with an instrumental beam, and $\boldsymbol{n}$ denotes instrumental noise. Additionally, we model the power spectrum of the underlying statistically isotropic field in terms of a two-parameter amplitude–tilt model of the form $C_\ell(q, n) = q\ (\ell/30)^n\ C_\ell^{\Lambda\text{CDM}}$, where $C_\ell^{\Lambda\text{CDM}}$ is the best-fit *Planck* 2015 ΛCDM spectrum (Planck Collaboration XI 2016). The two parameters $q$ and $n$ can accommodate a deficit in power at low $\ell$ as compared to the best-fit cosmology that would otherwise create a tension with the underlying statistically isotropic model and result in the analysis measuring a combination of both asymmetry and power mismatch.

In the absence of any dipole modulation, $\alpha = 0$, the total data covariance matrix is given by $\mathsf{C} = \mathsf{BS}_{\text{iso}}\mathsf{B}^{\text{T}} + \mathsf{N}$, where $\mathsf{S}_{\text{iso}}$ is the standard statistically isotropic CMB covariance matrix given by the power spectrum, $C_\ell$, $\mathsf{N}$ is the noise covariance matrix, and the corresponding likelihood is given by the usual expression for a multivariate Gaussian distribution. With dipole modulation, this generalizes straightforwardly to $\mathsf{C} = \mathsf{BMS}_{\text{iso}}\mathsf{M}^{\text{T}}\mathsf{B}^{\text{T}} + \mathsf{N}$, with the likelihood given by

$$\mathcal{L}(\alpha, \hat{p}, q, n) \propto \frac{\exp\left[-\frac{1}{2}\boldsymbol{d}^t(\mathsf{BMSM}^{\text{T}}\mathsf{B}^{\text{T}} + \mathsf{N})^{-1}\boldsymbol{d}\right]}{\sqrt{|\mathsf{BMSM}^{\text{T}}\mathsf{B}^{\text{T}} + \mathsf{N}|}}. \tag{43}$$

Figure 29 and Table 22 summarize this five-dimensional likelihood in terms of marginal parameters for each of the four

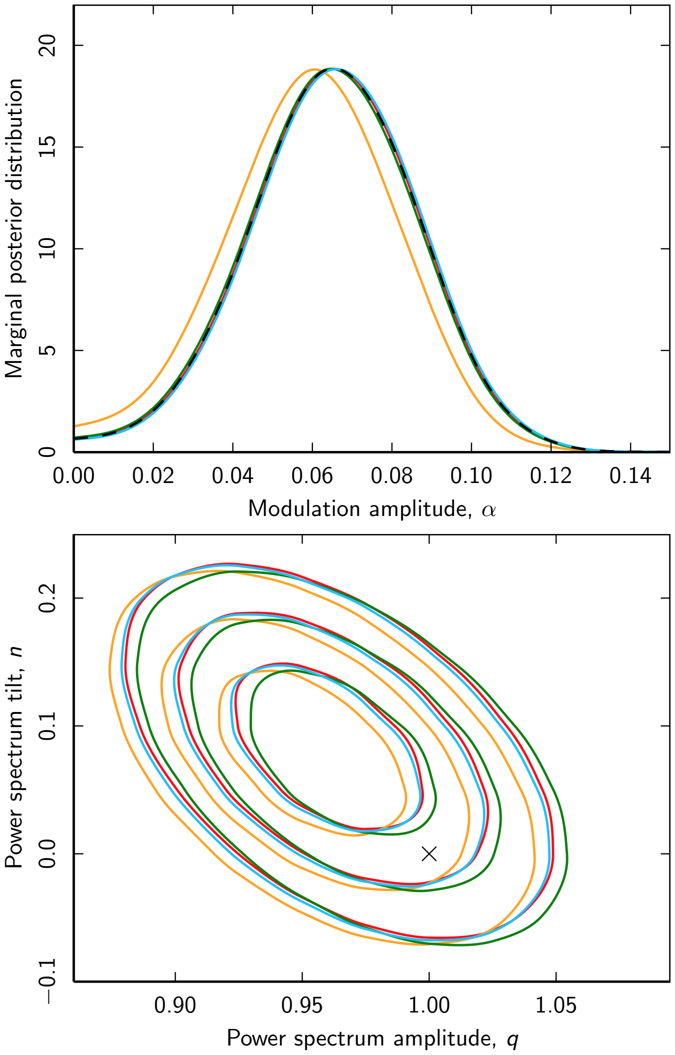

**Fig. 29.** *Top*: marginal constraints on the dipole modulation amplitude, as derived from *Planck* 2015 temperature observations at a smoothing scale of 5° FWHM for `Commander` (red), `NILC` (orange), `SEVEM` (green), and `SMICA` (blue). The plot corresponds directly to Fig. 32 of Planck Collaboration XXIII (2014). The `Commander`, `SEVEM`, and `SMICA` posteriors coincide almost perfectly both internally, and with the corresponding `SMICA` 2013 posterior, shown as a dashed black line. *Bottom*: corresponding marginal two-dimensional constraints on the low-$\ell$ power spectrum amplitude and tilt, $(q, n)$, defined relative to the best-fit *Planck* 2015 ΛCDM model.

*Planck* CMB maps, as evaluated over the common mask using the multi-dimensional grid-based `Snake` algorithm (Mikkelsen et al. 2013). All results correspond to a smoothing scale of 5° FWHM, the highest resolution supported by an $N_{\rm side} = 32$ `HEALPix` grid, but, as in 2013, we consider all smoothing scales between 5° and 10° FWHM, reaching similar conclusions in each case: the dipole modulation results derived from the *Planck* 2015 temperature maps are essentially identical to the 2013 results, with improved internal consistency between the four CMB maps due to better mitigation of systematic errors. The best-fit dipole modulation amplitude at 5° FWHM is 6–7% whilst the low-$\ell$ power spectrum has an approximately 3–5% lower amplitude compared to the best-fit ΛCDM prediction. These results are fully consistent with expectations given that the *Planck* 2013 sky maps were already cosmic-variance-limited on these angular scales, and the 2015 maps differ from the 2013 maps at the level of only a few microkelvin (Planck Collaboration IX 2016).

**Table 22.** Summary of dipole modulation results at a smoothing scale of 5° for all *Planck* 2015 CMB temperature solutions, as derived by the brute-force likelihood given by Eq. (43).

| Method | 2013 | 2015 |
|---|---|---|
| Dipole modulation amplitude, $\alpha$ | | |
| `Commander` . . . . . | $0.078 \pm 0.021$ | $0.066 \pm 0.021$ |
| `NILC` . . . . . . . . . . | $0.069 \pm 0.021$ | $0.061 \pm 0.022$ |
| `SEVEM` . . . . . . . . . | $0.066 \pm 0.021$ | $0.065 \pm 0.021$ |
| `SMICA` . . . . . . . . . | $0.065 \pm 0.021$ | $0.066 \pm 0.021$ |
| Dipole modulation direction, $(l, b)$ [°] | | |
| `Commander` . . . . . | $(227, -15) \pm 19$ | $(230, -16) \pm 24$ |
| `NILC` . . . . . . . . . . | $(226, -16) \pm 22$ | $(228, -19) \pm 29$ |
| `SEVEM` . . . . . . . . . | $(227, -16) \pm 24$ | $(226, -17) \pm 25$ |
| `SMICA` . . . . . . . . . | $(226, -17) \pm 24$ | $(225, -18) \pm 24$ |
| Power spectrum amplitude, $q$ | | |
| `Commander` . . . . . | ··· | $0.961 \pm 0.025$ |
| `NILC` . . . . . . . . . . | ··· | $0.954 \pm 0.024$ |
| `SEVEM` . . . . . . . . . | ··· | $0.966 \pm 0.025$ |
| `SMICA` . . . . . . . . . | ··· | $0.960 \pm 0.025$ |
| Power spectrum tilt, $n$ | | |
| `Commander` . . . . . | ··· | $0.082 \pm 0.043$ |
| `NILC` . . . . . . . . . . | ··· | $0.077 \pm 0.043$ |
| `SEVEM` . . . . . . . . . | ··· | $0.077 \pm 0.043$ |
| `SMICA` . . . . . . . . . | ··· | $0.081 \pm 0.043$ |

### 6.3. Dipole modulation: QML analysis

In this section we use the QML estimator introduced in Moss et al. (2011) and described in Appendix C to assess the level of dipole modulation in our estimates of the CMB sky at $N_{\rm side} = 2048$. The specific implementation is essentially identical to that used in Hanson & Lewis (2009), Planck Collaboration XVII (2014), and Planck Collaboration XXVII (2014), and exploits the fact that dipole modulation of any cosmological parameter is equivalent to coupling of $\ell$ to $\ell \pm 1$ modes in the CMB covariance matrix to leading order (see Appendix C). Planck Collaboration XX (2016) presents an alternate analysis for a specific isocurvature model.

Since we are interested in dipole modulation there are three independent estimators. For our particular approach, these are a real-valued $m = 0$ and a complex-valued $m = 1$ estimator, and take the form

$$\tilde{X}_0 = \frac{6}{f_{10}} \frac{\sum_{\ell m} \delta C_{\ell \ell+1} A_{\ell m} \left( T^*_{\ell m} T_{\ell+1\, m} - \left\langle T^*_{\ell m} T_{\ell+1\, m} \right\rangle \right)}{\sum_\ell \delta C^2_{\ell \ell+1} (\ell+1) F_\ell F_{\ell+1}}, \tag{44}$$

$$\tilde{X}_1 = \frac{6}{f_{11}} \frac{\sum_{\ell m} \delta C_{\ell \ell+1} B_{\ell m} \left( T^*_{\ell m} T_{\ell+1\, m+1} - \left\langle T^*_{\ell m} T_{\ell+1\, m+1} \right\rangle \right)}{\sum_\ell \delta C^2_{\ell \ell+1} (\ell+1) F_\ell F_{\ell+1}}. \tag{45}$$

Here $T_{\ell m}$ are $C$-inverse filtered data and $F_\ell \equiv \left\langle T_{\ell m} T^*_{\ell m} \right\rangle$. We adopt the inverse-variance filter from Planck Collaboration XVII (2014), where the approximate filter functions are also specified. We define $\delta C_{\ell \ell+1} \equiv dC_\ell/dX + dC_{\ell+1}/dX$, where $X$ is the parameter modulated, and $A_{\ell m}$ and $B_{\ell m}$ are numerical coefficients (details can be found in Appendix C). The factor $f_{1m}$ corrects the normalization for errors introduced by masking:

$$f_{1m} \equiv \int \mathrm{d}\Omega\, Y^*_{1m}(\Omega) M(\Omega), \tag{46}$$

where $M(\Omega)$ is the mask. Finally, we correct the direction for the effects of inhomogeneous noise which is not accounted for in the

**Table 23.** Amplitude ($A$) and direction of the low-$\ell$ dipole modulation signal determined from the QML analysis for the range $\ell \in [2, 64]$.

| Method | $A$ | Direction $(l, b)$ [°] |
|---|---|---|
| `Commander` . . . . . | $0.063^{+0.025}_{-0.013}$ | $(213, -26) \pm 28$ |
| `NILC` . . . . . . . . . . | $0.064^{+0.027}_{-0.013}$ | $(209, -25) \pm 28$ |
| `SEVEM` . . . . . . . . . | $0.063^{+0.026}_{-0.013}$ | $(211, -25) \pm 28$ |
| `SMICA` . . . . . . . . . | $0.062^{+0.026}_{-0.013}$ | $(213, -26) \pm 28$ |

**Notes.** The errors are calculated from the cosmic variance expected for statistically isotropic CMB realizations.

filtering process, by weighting the $\tilde{X}_m$ by the inverse of the variance derived from filtered and mean-field corrected simulations.

The physics is readily accessible in this estimator: the $\ell$-dependence in modulation determined by the parameter $X$ is expressed in the $\delta C_{\ell\ell+1}$ factor, and the relevant scales appear directly in the limits of the sum. We consider the estimator over the range $\ell_{\min} = 2 \leq \ell \leq \ell_{\max}$. The modulation amplitude and direction are then given by

$$\tilde{A} = \sqrt{\tilde{X}_0^2 + 2|\tilde{X}_1|^2}, \tag{47}$$

$$\tilde{\theta} = \cos^{-1}\left(\frac{\tilde{X}_0}{\tilde{A}}\right), \tag{48}$$

$$\tilde{\phi} = -\tan^{-1}\left(\frac{\mathrm{Im}[\tilde{X}_1]}{\mathrm{Re}[\tilde{X}_1]}\right). \tag{49}$$

It is worth re-emphasizing that the quantities $\tilde{A}$, $\tilde{\theta}$, and $\tilde{\phi}$ are all dependent on the $\ell$ range considered.

As a consequence of the central limit theorem, for sufficiently large $\ell_{\max}$ the $\tilde{X}$s are Gaussian-distributed with mean zero, so that the amplitude parameter has a Maxwell-Boltzmann distribution. We fit to this distribution for $\ell_{\max} \geq 10$ when computing the $p$-value, so as not to be influenced by Poisson noise in the tails of the empirical distribution (and we have determined that this is a good fit to the simulations by applying a KS test). For the case of scalar amplitude modulation (i.e., $X = A_\mathrm{s}$), and $\ell_{\min} = 2$, the cosmic-variance-limited expectation for the modulation amplitude from statistically isotropic skies is

$$\left\langle \frac{\Delta A_\mathrm{s}}{A_\mathrm{s}} \right\rangle \approx \sqrt{\frac{48}{\pi(\ell_{\max}+4)(\ell_{\max}-1)}}. \tag{50}$$

This is the cosmic variance for a scale-invariant dipole modulation, and gives a more explicit expression than the $\ell_{\max}^{-1}$ scaling discussed in Hanson & Lewis (2009).

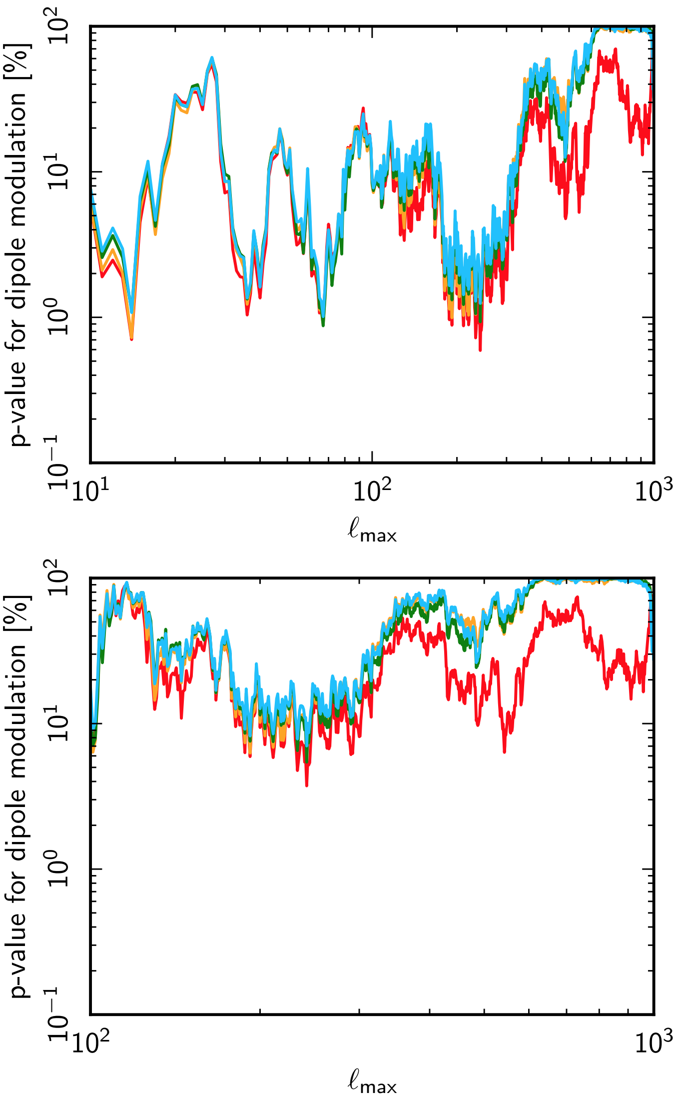

**Fig. 30.** Probability determined from the QML analysis for a Monte Carlo simulation to have a larger dipole modulation amplitude than the `Commander` (red), `NILC` (orange), `SEVEM` (green), or `SMICA` (blue) data sets, with (*top panel*) $\ell_{\min} = 2$ or (*bottom panel*) $\ell_{\min} = 100$. No significant modulation is found once the low-$\ell$ signal is removed. We emphasize that the statistic here is cumulative and apparent trends in the curves can be misleading.

The top panel of Fig. 30 presents results for the $p$-value of the fitted modulation amplitude as a function of $\ell_{\max}$. Note that there are several peaks, at $\ell \approx 40$ and $\ell \approx 67$ (the focus of most attention in the literature), and $\ell \approx 240$. The latter peak, while not previously emphasized, is also present in the WMAP results (see Fig. 15 in Bennett et al. 2011). It is also interesting to note that a modulation amplitude is observed at $\ell_{\max} \approx 800$ that is somewhat lower than what one would typically expect for a statistically isotropic sky. However, the significance is not at the level of the excess dipole modulation at low $\ell$ and will not be discussed further. The dip at $\ell_{\max} \approx 67$, with a $p$-value of 0.9–1.0%, corresponds to the well-known low-$\ell$ dipole modulation[6]. Table 23 presents the corresponding dipole modulation parameters, which are seen to be consistent with previous studies. Note that the mean amplitude expected for a set of statistically isotropic simulations at this $\ell_{\max}$ is 2.9% (in close agreement with the expected value due to cosmic variance, Eq. (50)).

We have therefore determined a phenomenological signature of modulation for $\ell = 2$–67 with a $p$-value of 0.9–1.0%. If such a signal had been predicted by a specific model, then we could claim a significance of about $3\sigma$. However, in the absence of such an a priori model, we can assess how often we might find a $3\sigma$ effect by chance, given that it could have occurred over any

---

[6] Actually only `SEVEM` and `SMICA` achieve their minimum at $\ell_{\max} = 67$, whereas `NILC` and `Commander` achieve theirs at $\ell_{\max} = 14$ and 240, respectively. Such scatter is expected when searching over a large number of possible $\ell$ ranges. The reconstructed amplitudes for each component-separation method are well within the error budgets of the estimator.

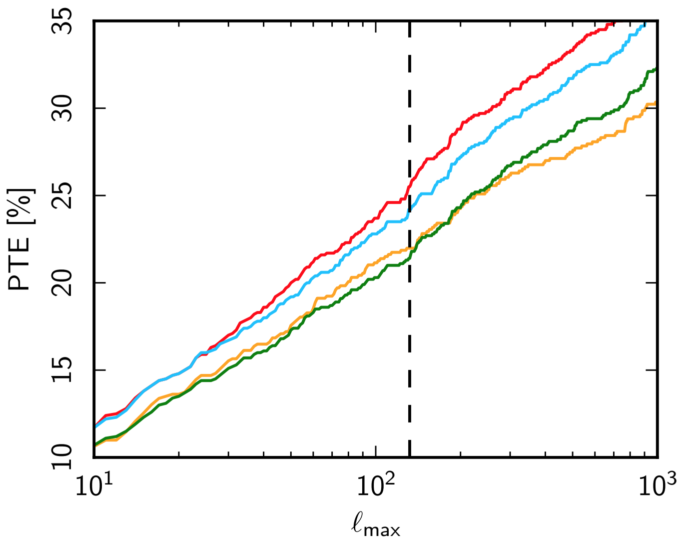

**Fig. 31.** Probability determined from the QML analysis for obtaining a dipole modulation amplitude at least as anomalous as the `Commander` (red), `NILC` (orange), `SEVEM` (green), and `SMICA` (blue) data sets, for the range $\ell \in [10, \ell_{\rm max}]$. The vertical line corresponds to $\ell_{\rm max} = 132$ which was used as the search limit in Bennett et al. (2011). The probability grows approximately logarithmically with $\ell_{\rm max}$. This means that the adopted probability to exceed is fortunately not very sensitive to $\ell_{\rm max}$, and for any reasonable choice is above 10%.

$\ell$ range. Since we are looking for a large-scale phenomenon, we assume that the analysis should include the corresponding low-$\ell$ modes and start at $\ell = 2$. In order to correct for a posteriori effects we then adopt the following scheme.

1. We calculate the modulation of each simulation on the scales 2–$\ell$, where $\ell \in [10, \ell_{\rm max}]$. For each simulation we find the modulation that gives the smallest probability, $\eta$ (in the same way that was done for the data).
2. With the distribution of $\eta$s given by the simulations we then compare this to the data. That is, we calculate the probability that one would find oneself in a Hubble patch with a modulation amplitude up to $\ell \in [10, \ell_{\rm max}]$ that is as significant as (or more significant than) the modulation in the real data.

If $\ell_{\rm max} = 132$ (as chosen by Bennett et al. 2011), the probability of achieving a modulation as large as the *Planck* data in this range is higher than 10% (see Fig. 31). This is in agreement with the findings of the WMAP team (which found 10% and 13% in the same $\ell$-range, using two different masks). Here, we do not quote a specific PTE for the dipole modulation since it depends on the choice of both $\ell_{\rm max}$ (albeit not so sensitively) and $\ell_{\rm min}$ (which we have decided not to marginalize over). However, it appears to be the case that the dipole modulation that we observe is quite unremarkable. That is, Gaussian fluctuations in a statistically isotropic Universe will reasonably often result in a dipole modulation with a comparable level of significance to that presented here.

Beyond this, evidence for dipole modulation is found at $\ell \approx 200$–$300$, with a smaller dip at $\ell \approx 500$. Given that the dipole modulation estimator is a cumulative quantity, it is possible that these features are statistically enhanced by the usual low-$\ell$ signal. To test this we analyse the dipole modulation as a function of $\ell_{\rm max}$ again, with the restriction $\ell_{\rm min} = 100$ applied in order to completely remove any low-$\ell$ influence. The outcome is presented in Fig. 30 (bottom). It is clear that even before introducing posterior corrections no significant modulation is found, indicating that the $p$-values of the features at $\ell > 100$ were indeed exaggerated by the low-$\ell$ modulation.

### 6.4. Bipolar spherical harmonics

In the absence of the assumption of statistical isotropy, the CMB two-point correlation function $C(\hat{n}_1, \hat{n}_2) \not\equiv C(\hat{n}_1 \cdot \hat{n}_2)$ can be most generally expanded in the bipolar spherical harmonic (BipoSH) basis representation as follows:

$$C(\hat{n}_1, \hat{n}_2) = \sum_{LM\ell_1\ell_2} \tilde{A}^{\rm LM}_{\ell_1\ell_2} \{Y_{\ell_1}(\hat{n}_1) \otimes Y_{\ell_2}(\hat{n}_2)\}_{\rm LM}. \qquad (51)$$

The BipoSH basis functions, $\{Y_{\ell_1}(\hat{n}_1) \otimes Y_{\ell_2}(\hat{n}_2)\}_{\rm LM}$ are tensor products of ordinary spherical harmonic functions, and the corresponding expansion coefficients are termed BipoSH coefficients (Hajian & Souradeep 2003; Hajian & Souradeep 2006). The BipoSH basis provides a complete representation of any form of statistical isotropy violation with the key advantage of separating the angular scale-dependence of the signal in spherical harmonic multipoles, $\ell$, from the nature of the violation indexed in the bipolar multipole space by $L$. Consequently, it is possible to simultaneously determine that such a signal is dipolar ($L = 1$), quadrupolar ($L = 2$), octopolar ($L = 3$), and so on, in nature and that the power is restricted to specific ranges of angular scales.

The estimation of BipoSH coefficients from CMB maps is a natural generalization of the more routinely undertaken estimation of the angular power spectrum $C_l$. To allow a direct connection to the angular power, we further introduce a set of BipoSH spectra at every bipolar harmonic moment, $(L, M)$, labelled by a difference index $d$, defined as follows:

$$A^{\rm LM}_{\ell\ell+d} = \tilde{A}^{\rm LM}_{\ell\ell+d} \frac{\Pi_L}{\Pi_{\ell(\ell+d)} C^{L0}_{\ell0(\ell+d)0}}, \quad (0 \le d \le L), \qquad (52)$$

where $C^{\rm LM}_{\ell_1 m_1 \ell_2 m_2}$ are the Clebsch-Gordon coefficients and for brevity the notation $\Pi_{\ell_1\ell_2..\ell_n} = \prod_{i=1}^{n} \sqrt{(2\ell_i + 1)}$. BipoSH spectra, clearly, are then simply a generalized set of CMB angular power spectra, with the standard CMB angular power spectrum $C_\ell = A^{00}_{\ell\ell}$ being one of them[7]. While $A^{00}_{\ell\ell}$ quantifies the properties of the statistically isotropic part of the CMB fluctuations, the additional BipoSH coefficients quantify the statistically anisotropic part of the CMB two-point correlation function.

Thus BipoSH provides a mathematically complete description of all possible violations of statistical isotropy in a Gaussian CMB sky map. It is then always possible to translate any specific model for such a signal into the language of BipoSH and provide a common approach for the multiple specialized tests that have been implemented previously in this paper and elsewhere. However, improving on the analysis of the 2013 *Planck* data, a new formalism is developed in order to reliably analyse a masked sky, as concisely described in Appendix D. Aluri et al. (2015) provides a more detailed description of the approach and includes an explicit demonstration of its validity using simulations.

---

[7] The BipoSH spectra, as defined in Eq. (52), restrict us to working with only even-parity BipoSH coefficients ($L+d$ is even) due to the vanishing of $C^{L0}_{\ell0\ell+d0}$ otherwise. While most known isotropy-violating phenomena like weak lensing, Doppler boost, non-circular beams, etc., can only produce even-parity BipoSH spectra, measurement of odd-parity BipoSH spectra can be used to test for systematic effects, or to search for the signatures of exotic effects such as the lensing of CMB photons by tensor metric perturbations.

**Table 24.** Amplitude ($A$) and direction of the dipole modulation in Galactic coordinates as estimated for the multipole range $\ell \in [2, 64]$ using a BipoSH analysis.

| Method | $A$ | Direction $(l, b)$ [°] |
|---|---|---|
| `Commander` . . | $0.067 \pm 0.023$ | $(230, -18) \pm 31$ |
| `NILC` . . . . . . . | $0.069 \pm 0.022$ | $(228, -17) \pm 30$ |
| `SEVEM` . . . . . . | $0.067 \pm 0.023$ | $(230, -17) \pm 31$ |
| `SMICA` . . . . . . | $0.069 \pm 0.022$ | $(228, -18) \pm 30$ |
| `SEVEM-100` . . | $0.070 \pm 0.023$ | $(231, -19) \pm 30$ |
| `SEVEM-143` . . | $0.068 \pm 0.023$ | $(230, -17) \pm 31$ |
| `SEVEM-217` . . | $0.069 \pm 0.023$ | $(229, -20) \pm 31$ |

**Notes.** The measured values of the dipole amplitude and direction are consistent for all maps.

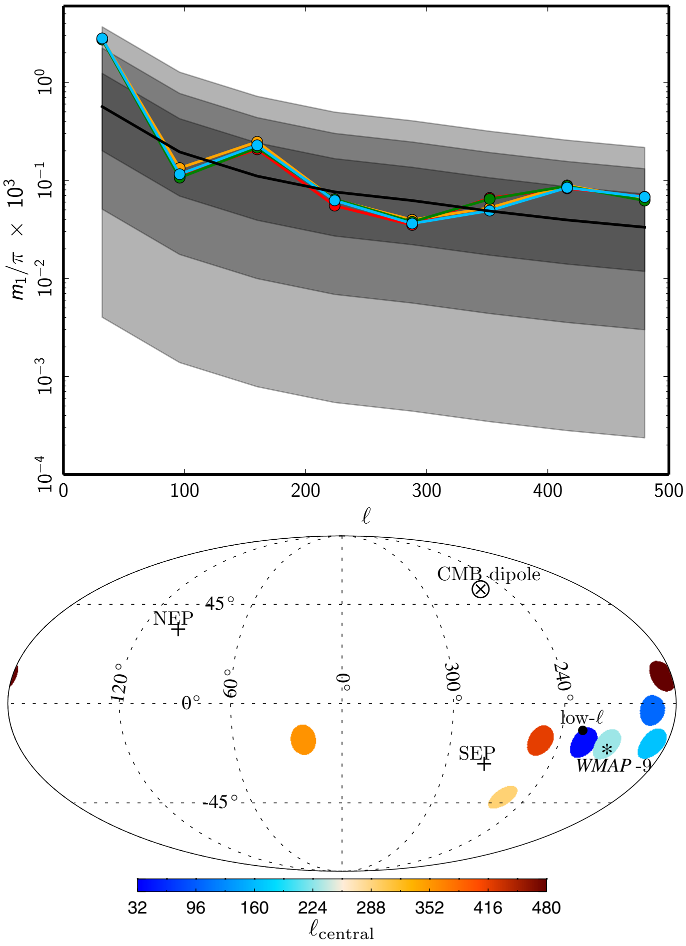

**Fig. 32.** *Top*: measured dipole modulation ($L = 1$) power in non-overlapping CMB multipole bins for `Commander` (red), `NILC` (orange), `SEVEM` (green), and `SMICA` (blue) as determined from a BipoSH analysis of the data. The power in the dipole of the modulation field is a $\chi^2$-distributed variable with 3 degrees of freedom. The shaded regions in the plot depict, in dark-grey, grey, and light-grey respectively, the 1, 2, and $3\sigma$ equivalent intervals of the distribution function derived from simulations, while the solid black line denotes its median. Significant power in the dipole modulation is seen to be limited to $\ell = 2$–64 and does not extend to higher multipoles. *Bottom*: dipole modulation direction as determined from the `SMICA` map. The directions found from the other component separation maps are consistent with this analysis. The coloured circles denote the central value of the multipole bin used in the analysis, as specified in the colour bar. The low-$\ell$ and WMAP-9 directions are identical to those in Fig. 35.

Initially, we revisit the simple phenomenological model of dipole modulation of the CMB sky from Sect. 6.2,

$$T(\hat{\boldsymbol{n}}) = T_0(\hat{\boldsymbol{n}})\,(1 + \mathcal{M}(\hat{\boldsymbol{n}}))\,, \tag{53}$$

where $T(\hat{\boldsymbol{n}})$ represents the modulated CMB sky, $T_0(\hat{\boldsymbol{n}})$ is the underlying (statistically isotropic) random CMB sky, and $\mathcal{M}(\hat{\boldsymbol{n}})$ is a dipolar field. The BipoSH coefficients resulting from such a modulation are given by

$$A^{1M}_{\ell\ell+1} = \bar{A}^{1M}_{\ell\ell+1} + m_{1M} G^{1}_{\ell\ell+1}, \tag{54}$$

$$G^{1}_{\ell\ell+1} = \frac{C_\ell + C_{\ell+1}}{\sqrt{4\pi}} \sqrt{\frac{(2\ell+1)(2\ell+3)}{3}}\, C^{10}_{\ell 0(\ell+1)0}. \tag{55}$$

Here $\bar{A}^{1M}_{\ell\ell+1}$ corresponds to the BipoSH coefficients of the unknown, but statistically isotropic, unmodulated CMB field, $m_{1M}$ are the spherical harmonic coefficients of the modulation field, and $C_\ell$ is the best-fit CMB angular power spectrum.

The BipoSH representation further enables an estimate of the modulation field to be made over specific angular scales by windowing regions in multipole space in the sum over multipoles $\ell$ in Eq. (55). This additional information is important for identifying the origin of the isotropy-breaking signal, which could be either cosmological or due to systematic artefacts.

We perform the analysis for the $N_{\rm side} = 2048$ component separated CMB maps with an apodized version of the common mask at that resolution and reconstruct the modulation signal in independent bins of width $\Delta\ell = 64$ up to $\ell_{\rm max} = 512$. The application of the common mask introduces a mean field bias in the BipoSH coefficients derived from the data. This bias is estimated from the FFP8 simulations and subtracted from the derived coefficients. The process of masking induces a coupling between the modulation field and the mask that results in a modification of the spectral shape of the modulation signal by the modified shape function (MSF; see Appendix D for details). Further, the covariance of the bias-subtracted BipoSH coefficients is not easy to derive analytically in this case. To overcome this problem, we consider the diagonal approximation to the covariance matrix and estimate it from simulations.

The results presented in the top panel of Fig. 32 indicate that the dipole modulation signal is most significant in the lowest multipole window $\ell \in [2, 64]$. Note that the power in the dipole modulation field $m_1 = (|m_{11}|^2 + |m_{10}|^2 + |m_{1-1}|^2)/3$ is related to the dipole amplitude by $A = 1.5\sqrt{m_1/\pi}$. The best-fit amplitude ($A$) and direction corresponding to the reconstructed dipole modulation field from this lowest multipole bin is quoted in Table 24 for each component-separation method. Also shown are the corresponding results for the cleaned frequency maps `SEVEM-100`, `SEVEM-143`, and `SEVEM-217`. As expected for signals with a cosmological origin, no evidence for frequency dependence is seen.

Since the amplitude of the dipole modulation field is consistent with zero within $2\sigma$ for all of the higher $\ell$-bins considered, it is plausible that the simple modulation model in Eq. (53) is inadequate to describe the features seen in the BipoSH spectra and should minimally allow for the amplitude, $A(\ell)$, of the dipole to depend on CMB multipole, $\ell$. Although this may appear to be a more complex model, it does not necessarily lack motivation. It is readily conceivable that physical mechanisms that cause a dipolar modulation of the random CMB sky would be

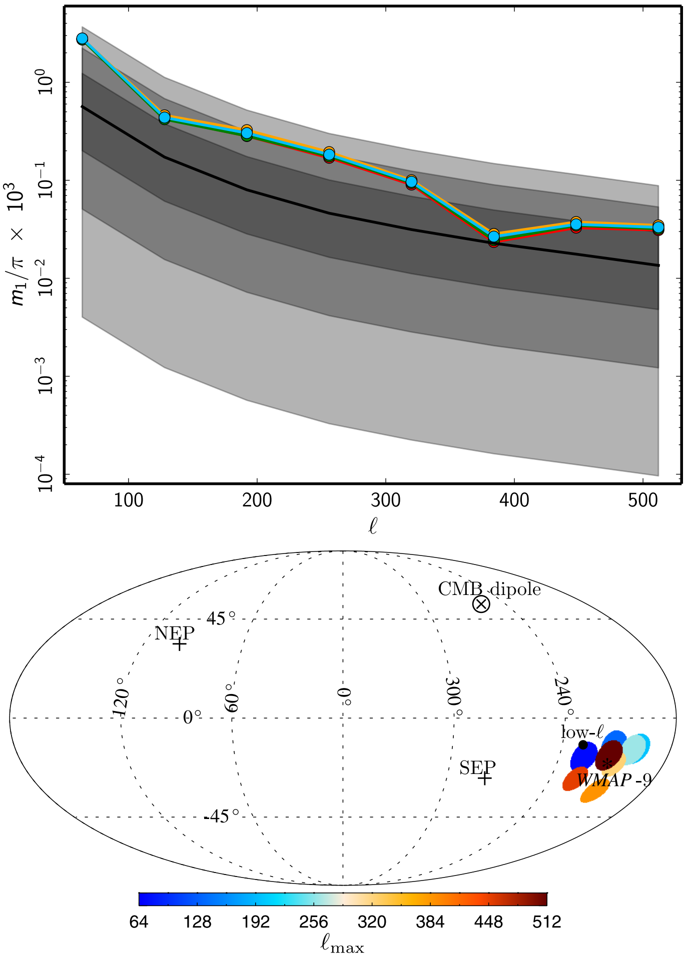

**Fig. 33.** *Top*: measured dipole modulation power in cumulative CMB multipole bins for `Commander` (red), `NILC` (orange), `SEVEM` (green), and `SMICA` (blue) as determined from a BipoSH analysis of the data.. Colour coding as in Fig. 32. Note that the measurements in cumulative bins indicate a power in excess of $2\sigma$ up to multipole $\ell_{\max} \sim 320$. The value on the horizontal axis denotes the maximum multipole used in the analysis, with $\ell_{\min} = 2$. *Bottom*: modulation dipole direction as recovered from the `SMICA` map. The directions found from the other component-separation maps are consistent with these directions. The colour-coded points represent the directions recovered for the specific $\ell_{\max}$ used in the analysis, with $\ell_{\min} = 2$. The low-$\ell$ and WMAP-9 directions are identical to those in Fig. 35.

scale-dependent and possibly significant only at low wavenumbers. It is also intriguing to note that, although in most cases the amplitude of the modulation dipole is seen at low significance, the directions in the first four bins, $\ell_{32} \in [2, 64]$, $\ell_{96} \in [65, 128]$, $\ell_{160} \in [129, 192]$, and $\ell_{224} \in [193, 256]$, are seen to be clustered together, as shown in the bottom panel of Fig. 32. Note that the lower significance of the modulation for the multipole bins at $\ell > 64$ results in larger errors for their respective directions than the value quoted for the $\ell \in [2, 64]$ bin recorded in Table 24.

We extend our analysis to carry out the dipole modulation reconstruction in cumulative bins up to $\ell_{\max} = 512$, making cumulative increments in the multipole in steps of $\Delta\ell = 64$. The results of this analysis are summarized in Fig. 33.

As noted previously, as a consequence of our motion with respect to the CMB rest frame, the observed CMB map is expected to be statistically anisotropic, as has been demonstrated in Planck Collaboration XXVII (2014) and Appendix B. Reassuringly, in PCIS13 it was established that such a signal would not contaminate a dipole modulation signal up to $\ell_{\max} \approx 700$. We now confirm the Doppler boost signal using the BipoSH methodology.

**Table 25.** Doppler boost amplitude ($|\boldsymbol{\beta}|$) and direction in Galactic coordinates derived over the multipole range $\ell \in [640, 1024]$ as evaluated from a BipoSH analysis.

| Method | $\lvert\boldsymbol{\beta}\rvert \times 10^{-3}$ | Direction $(l, b)$ [°] |
|---|---|---|
| `SEVEM-100` . . . . | $1.24 \pm 0.66$ | $(277, 40) \pm 50$ |
| `SEVEM-143` . . . . | $1.35 \pm 0.56$ | $(264, 39) \pm 39$ |
| `SEVEM-217` . . . . | $1.28 \pm 0.45$ | $(257, 42) \pm 32$ |

**Notes.** The errors are estimated from an identical analysis of a set of 1000 Doppler boosted simulations for each frequency.

An equivalent description of the Doppler boost in terms of BipoSH coefficients is given by

$$A^{1M}_{\ell_1\ell_2} = \tilde{A}^{1M}_{\ell_1\ell_2} + \beta_{1M} G^1_{\ell_1\ell_2}, \tag{56}$$

$$G^1_{\ell_1\ell_2} = \left\{ b_\nu [G^1_{\ell_1\ell_2}]^{\mathcal{M}} - [G^1_{\ell_1\ell_2}]^{\phi} \right\} \times \sqrt{\frac{(2\ell_1+1)(2\ell_2+1)}{12\pi}} C^{10}_{\ell_1 0 \ell_2 0}, \tag{57}$$

$$\left[G^1_{\ell_1\ell_2}\right]^{\mathcal{M}} = \left[C_{\ell_1} + C_{\ell_2}\right], \tag{58}$$

$$\left[G^1_{\ell_1\ell_2}\right]^{\phi} = \left[C_{\ell_1} + C_{\ell_2}\right] + \left[C_{\ell_1} - C_{\ell_2}\right]\left[\ell_1(\ell_1+1) - \ell_2(\ell_2+1)\right]/2, \tag{59}$$

where $\beta_{1M} = \int \mathrm{d}n Y_{1M}(\hat{\boldsymbol{n}}) \boldsymbol{\beta} \cdot \hat{\boldsymbol{n}}$, $\boldsymbol{\beta} = \boldsymbol{v}/c$ denotes the peculiar velocity of our local rest frame with respect to the CMB, and $b_\nu$ is the frequency-dependent boost factor, as discussed in more detail in Planck Collaboration XXVII (2014).

Since the Doppler boost signal has a frequency dependence, we perform our analysis on the `SEVEM-100`, `SEVEM-143`, and `SEVEM-217` maps at $N_{\mathrm{side}} = 2048$, and adopt values of $b_\nu = 1.51, 1.96$, and $3.07$, respectively. A minimum variance estimator for $\beta_{1M}$, as discussed in Appendix D, is adopted with the shape function $G^L_{\ell_1\ell_2}$ replaced by the corresponding Doppler boost term given in Eq. (56). Corresponding unboosted CMB simulations were also used, in particular to correct for the mean field bias. However, we use a set of Doppler-boosted simulations in order to estimate the error on the reconstructed Doppler boost vector.

Since it is expected that the low multipole modes of the $A^{1M}_{l,l+1}$ spectrum are contaminated by the dipolar signal reported previously, in order to monitor the impact of this anomalous signal on the Doppler reconstruction we implement a cumulative analysis using multipoles with a varying $\ell_{\min}$ from 2 to 640 in increments of $\Delta\ell_{\min} = 128$ and a fixed $\ell_{\max} = 1024$[8]. The recovered Doppler amplitudes from the three `SEVEM` frequency cleaned maps as a function of $\ell_{\min}$ are shown in the top panel of Fig. 34, while the lower panel indicates the corresponding direction $\hat{\beta}$ in Galactic coordinates determined from the `SEVEM-217` data. Table 25 records the best-fit amplitudes and directions for $\ell \in [640, 1024]$.

---

[8] We fix $\ell_{\max} = 1024$ since at higher $\ell$ values the mismatch between the data and simulation power spectra becomes more important and is a concern for the bias subtraction applied when reconstructing the Doppler boost signal.

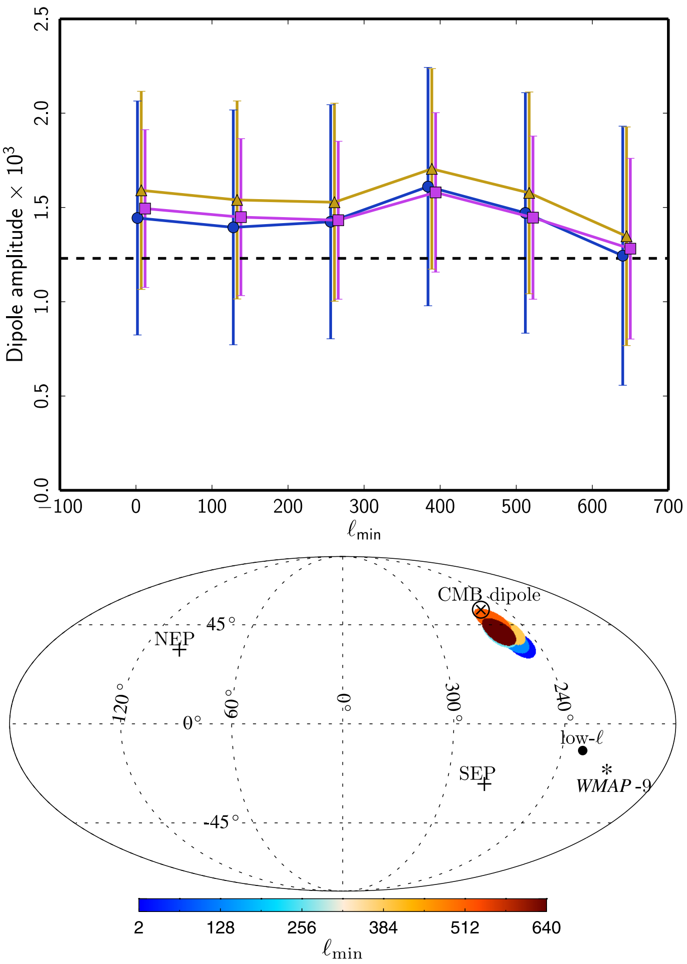

**Fig. 34.** *Top*: amplitude $|\beta|$ of the Doppler boost from the `SEVEM-100`, `SEVEM-143`, and `SEVEM-217` maps for different multipole bins determined using a BipoSH analysis. The maximum multipole of each bin is fixed at $\ell_{\rm max} = 1024$, while $\ell_{\rm min}$ is incremented from $\ell = 2$ to $\ell = 640$ in steps of $\Delta\ell = 128$. The dashed line corresponds to the actual dipole boost amplitude, $|\beta| = 1.23 \times 10^{-3}$. *Bottom*: Doppler boost direction $\hat{\beta}$ measured in Galactic coordinates from `SEVEM-217`. The coloured circles denote $\ell_{\rm min}$ used in the analysis, while $\ell_{\rm max} = 1024$ is held fixed. The low-$\ell$ and WMAP-9 directions are identical to those in Fig. 35.

### 6.5. Angular clustering of the power distribution

In the *Planck* 2013 data release we reported a possible deviation from statistical isotropy in the multipole range $\ell = 2$–600, thus confirming earlier findings based on the WMAP data (Hansen et al. 2009; Axelsson et al. 2013). This claim of asymmetry extending to higher multipoles was made only on the basis of the alignment of preferred directions as determined from maps of the power distribution on the sky for specific multipole ranges. In particular, it was found that the directions of the dipoles fitted to such maps in the multipole range $\ell = 2$–600 were significantly more aligned than in simulations. In addition, we showed that the ratio of the power spectra in the two opposite hemispheres defined by the asymmetry axis for $\ell = 2$–600 was not statistically anomalous (as later confirmed over the extended multipole range $\ell = 2$–2000 by Quartin & Notari 2015).

Here, we test for the alignment in the *Planck* 2015 data set. We adopt the approach for the estimation of the dipole alignment that was described in detail in PCIS13, a brief summary of which follows.

1. Local power spectra are estimated from the data at $N_{\rm side} = 2048$ for 12 patches of the sky corresponding to the $N_{\rm side} = 1$ `HEALPix` base pixels. Only those high-resolution pixels surviving the application of the common mask are included in the analysis[9]. As a consequence of this masking, when patches based on `HEALPix` pixels with $N_{\rm side} > 1$ are used, the available sky fraction for those patches close to the Galactic plane is too small for power-spectrum estimation. For most of the analysis, we use the cross-spectra determined from half-mission data sets[10]. Due to a mismatch between the noise level in the data and the simulated maps, the results based on auto-spectra are less reliable and also more prone to other systematic effects than the cross-spectra. We therefore do not consider such results here. The spectra are binned over various bin sizes between $\Delta\ell = 8$ and $\Delta\ell = 32$.
2. For each power spectrum multipole bin, an $N_{\rm side} = 1$ `HEALPix` map with the local power distribution is constructed.
3. The best-fit dipole amplitude and direction are estimated from this map using inverse-variance weighting, where the variance is determined from the local spectra computed from the simulations. We do not compute error bars for the direction, but expect this to be accounted for in part by the use of equivalently treated simulations in the clustering analysis.
4. A measure of the alignment of the different multipole blocks is then constructed. In PCIS13, we considered the mean angle between all possible pairs of dipole directions up to a given $\ell_{\rm max}$. Here, for greater consistency with Sect 6.6, we use the mean of the cosine of the angles, rather than of the angles themselves, between all pairs of dipoles. This effectively corresponds to the Rayleigh statistic (RS) introduced formally in Sect. 6.6, and we will refer to it as such, although it differs by ignoring all amplitude information. Clearly, smaller values of the RS correspond to less clustering.
5. The clustering as a function of $\ell_{\rm max}$ is then assessed using $p$-values determined as follows. We first construct the RS using all multipoles up to $\ell_{\rm max}$. The $p$-value is then given by the fraction of simulations with a higher RS than for the data for this $\ell_{\rm max}$. A small $p$-value therefore means that there are few simulations that exhibit as strong clustering as the data. Note that the $p$-values are highly correlated as the RS is a cumulative function of $\ell_{\rm max}$.
6. We then define two measures of significance. To achieve this, it is necessary to reduce the 1499 different $p$-values determined for $\ell_{\rm max} \in [2, 1500]$ to a single measure of clustering. We do this in two different ways, using the mean of these $p$-values, and by finding the minimum of the $p$-values, for both the data and for each available simulation. We then determine the percentage of simulations with (i) a lower mean $p$-value and (ii) a lower minimum $p$-value than the data. Note that these two measures of significance take into account different aspects of the data. Note further that since the RS is cumulative and the $p$-values therefore correlated, different scales are weighted unequally and a detection in the mean

---

[9] Departing from the analysis in PCIS13, we do not use an apodized version of the common mask. Simulations indicate that the error on the power spectrum for those multipoles in the range 300 to 500 where the significance is highest is up to 20% larger in this case, with the corresponding error on preferred direction being typically 8% larger.

[10] Note that simulated half-mission noise maps were generated by adjusting the properties of the existing 1000 (10 000 in the case of `SMICA`) noise simulations appropriately, thus explaining why only 500 (5000) simulations are used in this analysis.

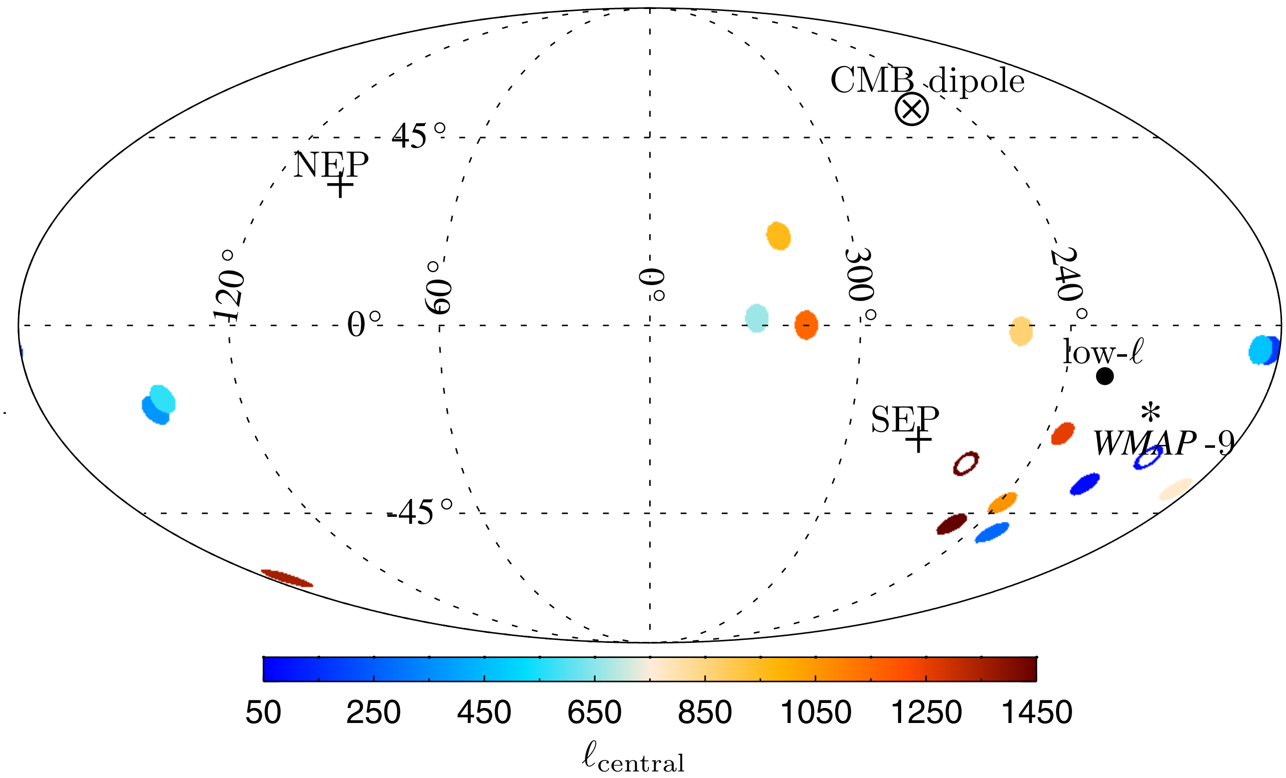

**Fig. 35.** Dipole directions for independent 100-multipole bins of the local power spectrum distribution from $\ell = 2$ to 1500 in the SMICA map with the common mask applied. We also show the preferred dipolar modulation axis (labelled as "low-$\ell$") derived in Sect. 6.2, as well as the total direction for $\ell_{\rm max} = 600$ determined from WMAP-9 (Axelsson et al. 2013). The average directions determined from the two multipole ranges $\ell \in [2, 300]$ and $\ell \in [750, 1500]$ are shown as blue and red rings, respectively. The error on the derived direction that results from masking the data is about 60°, with only small variations related to bin size.

and/or minimum $p$-value may be difficult to interpret and to correct for the multiplicity of tests effect (LEE).

Note that the statistics defined in step 6 above correspond to two choices of what were referred to as "global statistics" in PCIS13 in order to assess the degree to which the significance of the results depends on a specific choice for $\ell_{\rm max}$. The mean $p$-value over all available $\ell_{\rm max}$ measures the degree to which clustering is present over large multipole ranges independently of whether the clustering is strongly focused in one given direction. Clearly the $p$-values for different $\ell_{\rm max}$ are strongly correlated, but if the clustering is present only over a small multipole range, the RS will drop and the corresponding $p$-values will eventually rise. By comparing this value to simulations, we test not only whether the dipole alignment in the data is stronger than in statistically isotropic random simulations, but also whether it is present over larger ranges of multipoles than expected. The minimum $p$-value will give strong detections if there is a strong asymmetry over a limited multipole range or weaker clustering over larger multipole ranges when the clustering is strongly focused in a given direction.

For `Commander`, `NILC`, and `SEVEM`, only 500 simulations are available. However, 5000 simulations are available for `SMICA`, which allows a better estimate of significance to be determined when the probabilities obtained are very low. In this case, we use half of the 5000 simulations to calibrate the statistic (obtain $p$-values following step 5 above) and the remaining half to determine significance levels (compute the mean and minimum over these $p$-values as a function of $\ell_{\rm max}$ following step 6). When using 500 simulations, it is necessary to use the same set of simulations to calibrate as well as to obtain probabilities. A related issue with these results is that this set of simulations (corresponding to the first 500 out of the 5000 available for `SMICA`) are observed to yield higher $p$-values for the clustering angle due to a statistical fluctuation. Another 9 sets of 500 simulations that can be obtained from partitioning the 5000 available `SMICA` simulations all result in lower $p$-values. As a consequence, we observe that results based on the larger number of simulations often give lower $p$-values than when only 500 simulations are used.

In Fig. 35 we show the dipole directions of the 15 lowest 100-multipole bins for the `SMICA` map. Here, the binning has been chosen for visualization purposes; in further analysis of the *Planck* data we use finer $\ell$-intervals. The preferred low-$\ell$ modulation direction determined in Sect. 6.2 is also indicated, along with the WMAP-9 result determined over the range $\ell = 2$ to 600 (Axelsson et al. 2013). The observed clustering of the dipole directions is similar to that shown in figure 27 of PCIS13. Note that differences in masking, foreground subtraction, and residual systematic effects will displace the direction of a given dipole with respect to the previous analysis. Similar behaviour is seen for all of the *Planck* component-separated maps.

In PCIS13, we calculated the mean angle between all possible pairs of dipole directions determined from maps of the local power in multipole bins of size $\Delta\ell = 16$. Here we test the possible bias arising from such a choice by considering bin sizes between $\Delta\ell = 8$ and $\Delta\ell = 32$ in steps of 2. The lower limit avoids significant bin-to-bin coupling in the power spectra for smaller binnings, whilst the upper limit excludes cases where there are an insufficient number of derived dipoles from which the mean angle can be calculated, this leading to poor statistics. In addition to showing results for each bin size, we also calculate the

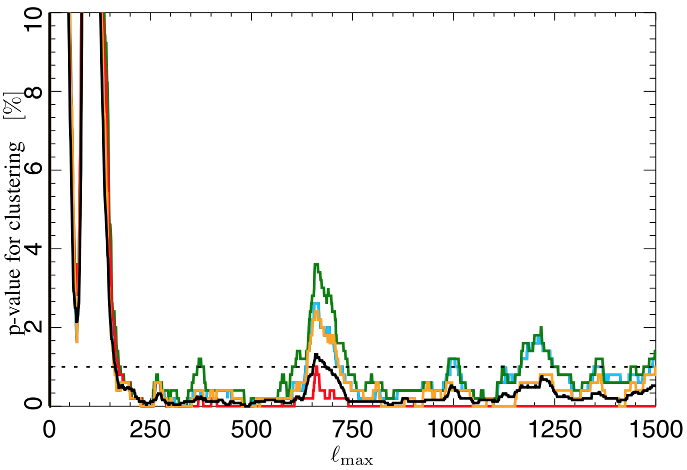

**Fig. 36.** Derived $p$-values for the angular clustering of the power distribution as a function of $\ell_{\max}$, determined for `Commander` (red), `NILC` (orange), `SEVEM` (green), and `SMICA` (blue), based on 500 simulations. For SMICA, the $p$-values based on 2500 simulations are also shown (black). The $p$-values are based on the fraction of simulations with a higher RS, determined over the $\ell$-range up to the given $\ell_{\max}$, compared to the data. The results shown here have been marginalized over bin sizes in the range $\Delta\ell = 8$ to $\Delta\ell = 32$.

variance-weighted mean of the power spectra over all bin sizes (the $C_\ell$ for a given bin size is weighted by $1/\sqrt{N_{\rm b}}$ where $N_{\rm b}$ is the bin size). In this way, we marginalize over bin sizes to obtain local power spectra and thereby the RS for each single multipole.

Figure 36 shows the $p$-values for the different component-separated maps, derived as described in step 5 above. We see that the results based on 500 simulations for `NILC`, `SEVEM`, and `SMICA` are in good agreement. The `Commander` results are less consistent, but this may be related to the fact that component separation was performed independently for the half-mission solutions, in contrast to the other methods, where component-separation solutions were obtained from the full mission data only. For `SMICA`, we also show $p$-values based on 2500 simulations. These more accurate results show lower $p$-values, and may indicate that those determined from only 500 simulations are not sufficiently stable. Note also that for $\ell < 100$ the $p$-values are not consistent with the detection of a low-$\ell$ asymmetry/modulation, as seen by other methods in this paper. However, for $\ell < 100$, there are very few bins and the variance of the RS might therefore be too high for this effect to be visible.

In agreement with the conclusions in PCIS13, a large degree of alignment is seen at least to $\ell_{\max} \approx 600$. However, in contrast to the earlier results where the $p$-values started increasing systematically for $\ell_{\max} > 1000$, the current $p$-values remain low for $\ell_{\max} > 750$. The full component-separated maps which have higher resolution and sensitivity are used for the current analysis, instead of the single-frequency foreground-cleaned map (`SEVEM-143`) used in PCIS13. We note that the results for the updated `SEVEM-143` map are consistent with the earlier analysis, both with and without correction for the Doppler modulation. Note also that the `SMICA` results with improved statistics (based on 2500 simulations) generally show lower $p$-values than the corresponding results based on 500 simulations.

Table 26 presents the fraction of simulations with a lower mean/minimum $p$-value than in the data for a number of different cases. The table shows probabilities for `SMICA` with different bin sizes (showing only every second bin size since these are correlated), as well as for the results marginalized over bin sizes. We also show results for the different component-separated maps, results based on half-ring cross-spectra instead of half-mission cross-spectra, and results using a different $\ell$-weighting scheme, specifically $(2\ell+1)C_\ell$ instead of $\ell(\ell+1)C_\ell$, the former being a measure of the variance of the temperature fluctuations. The table indicates probabilities of approximately 0–2% for most of these cases, although results for the smallest bin size show much less significant results. This could be due to the strong anticorrelations between adjacent bins found for this bin size in those Galactic $N_{\rm side} = 1$ patches with very small available sky fraction. For the other bin sizes, these correlations are much weaker. Note that many of the significances based on minimum $p$-value are only upper limits. This is due to the fact that the limited number of simulations in some cases results in the lowest minimum $p$-value being zero. When the minimum $p$-value in the data is zero, we show the percentage of simulations which also have zero as the minimum $p$-value. Clearly this fraction is only an upper limit on the real significance.

In order to further investigate the $\ell$-dependence of the asymmetry, we follow two approaches from PCIS13. Firstly,

**Table 26.** Significance of the angular clustering of the power distribution.

| Method | Bin size | Mean $p$-value | % (mean) | Min. $p$-value | % (min) |
|---|---|---|---|---|---|
| `SMICA` . . . . . . | 8 | 261/2500 | 1.60 | 35/2500 | 16.2 |
| `SMICA` . . . . . . | 10 | 51/2500 | 0.08 | 3/2500 | 2.36 |
| `SMICA` . . . . . . | 12 | 75/2500 | 0.20 | 1/2500 | 0.96 |
| `SMICA` . . . . . . | 14 | 83/2500 | 0.16 | 2/2500 | 1.52 |
| `SMICA` . . . . . . | 16 | 78/2500 | 0.24 | 4/2500 | 2.00 |
| `SMICA` . . . . . . | 18 | 51/2500 | 0.04 | 1/2500 | 0.68 |
| `SMICA` . . . . . . | 20 | 21/2500 | <0.04 | 1/2500 | 0.76 |
| `SMICA` . . . . . . | 22 | 60/2500 | 0.08 | 2/2500 | 1.24 |
| `SMICA` . . . . . . | 24 | 34/2500 | 0.08 | 2/2500 | 1.00 |
| `SMICA` . . . . . . | 26 | 38/2500 | 0.08 | 1/2500 | 0.96 |
| `SMICA` . . . . . . | 28 | 42/2500 | 0.20 | 0/2500 | <0.52 |
| `SMICA` . . . . . . | 30 | 27/2500 | 0.20 | 0/2500 | <0.60 |
| `SMICA` . . . . . . | 32 | 21/2500 | 0.04 | 0/2500 | <0.52 |
| `SMICA` . . . . . . | marg. | 43/2500 | <0.04 | 0/2500 | <1.00 |
| `SMICA`$^{a}$ . . . . . | marg. | 48/2500 | <0.04 | 1/2500 | 1.70 |
| `SMICA`$^{b}$ . . . . . | marg. | 47/2500 | <0.04 | 0/2500 | <1.16 |
| `SMICA`$^{c}$ . . . . . | marg. | 50/2500 | <0.04 | 0/2500 | <0.76 |
| `SMICA`$^{d}$ . . . . . | marg. | 254/2500 | 1.52 | 34/2500 | 20.1 |
| `Comm.` . . . . . . | marg. | 9/500 | <0.20 | 0/500 | <2.60 |
| `NILC` . . . . . . . | marg. | 10/500 | <0.20 | 0/500 | <3.60 |
| `SEVEM` . . . . . . | marg. | 13/500 | <0.20 | 0/500 | <4.00 |
| `SMICA` . . . . . . | marg. | 11/500 | <0.20 | 0/500 | <3.60 |
| `Comm.`$^{b}$ . . . . . | marg. | 11/500 | <0.20 | 0/500 | <3.00 |
| `NILC`$^{b}$ . . . . . | marg. | 10/500 | <0.20 | 0/500 | <3.80 |
| `SEVEM`$^{b}$ . . . . . | marg. | 12/500 | <0.20 | 0/500 | <3.40 |
| `SMICA`$^{b}$ . . . . . | marg. | 11/500 | <0.20 | 0/500 | <3.80 |
| `Comm.`$^{c}$ . . . . . | marg. | 8/500 | 0.20 | 0/500 | <4.00 |
| `NILC`$^{c}$ . . . . . | marg. | 14/500 | 0.20 | 1/500 | 7.20 |
| `SEVEM`$^{c}$ . . . . . | marg. | 17/500 | 0.20 | 1/500 | 8.40 |
| `SMICA`$^{c}$ . . . . . | marg. | 15/500 | 0.20 | 1/500 | 7.60 |

**Notes.** We indicate the actual mean/min $p$-value of the data, determined from Fig. 36 and written as a fraction of the number of simulations used to assess the values, together with the percentage of simulations with a lower mean/minimum $p$-value than the data. Unless otherwise specified, the numbers are determined from half-mission cross spectra $C_\ell\ell(\ell+1)$, for all multipoles in the range $\ell = 2$–1500, and for the common mask. $^{(a)}$ Half-ring maps instead of half-mission maps. $^{(b)}$ $C_\ell(2\ell+1)$ instead of $C_\ell\ell(\ell+1)$. $^{(c)}$ Restricted to multipoles $\ell > 100$. $^{(d)}$ Restricted to multipoles $\ell > 200$.

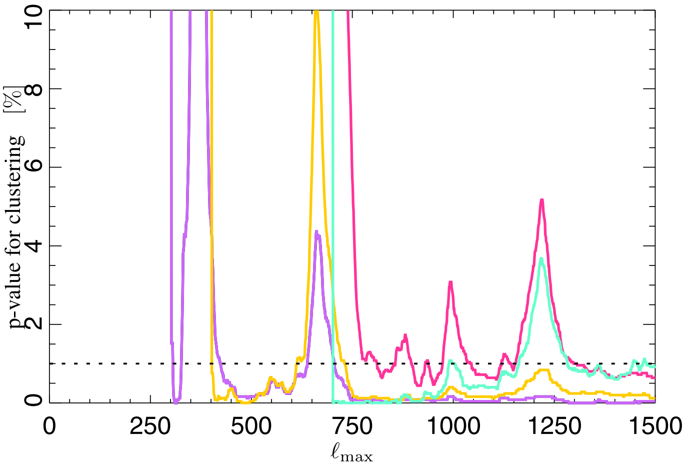

**Fig. 37.** Derived $p$-values for the angular clustering analysis as a function of $\ell_{\max}$, determined from `SMICA` based on 2500 simulations. The $p$-values are based on the fraction of simulations with a higher Rayleigh statistic up to the given $\ell_{\max}$ than in the data. The RS here is calculated over all pairs of dipole directions where one dipole in each pair is computed in the range $[\ell_{\lim}, \ell_{\max}]$, and the other is determined in the range $[2, \ell_{\lim}]$. The plot shows $p$-values for $\ell_{\lim} = 300$ (purple), $\ell_{\lim} = 400$ (yellow), $\ell_{\lim} = 500$ (pink), and $\ell_{\lim} = 700$ (cyan). The results have been marginalized over bin sizes in the range $\Delta\ell = 8$ to $\Delta\ell = 32$.

we restrict the analysis to multipoles above a minimum multipole $\ell_{\min}$. Table 26 indicates that clustering at the <1% significance level is still found when considering only those multipoles with $\ell_{\min}$ greater than 100. However, when this limit is increased to 200, no significant clustering is found. We then calculate the RS between pairs of dipoles where one dipole is determined from an $\ell$-range above a certain limiting multipole $\ell_{\lim}$, and the other dipole below this limit. Figure 37 shows the RS as a function of $\ell_{\max}$ for some selected values of $\ell_{\lim}$. The $\ell_{\lim} = 300$ curve (purple) indicates that dipole directions for $\ell > 1000$ are significantly aligned with dipoles for $\ell < 300$. Similarly, the $\ell_{\lim} = 700$ curve (cyan) indicates that the dipole directions for $\ell = 700$–$1000$ are strongly correlated with the dipole directions for $\ell < 700$.

Combining these results, we note that when using only multipoles with (i) $\ell > 200$; or (ii) $\ell < 200$, no significant clustering is found. The strong clustering significance shown to persist to high multipoles in Fig. 36 must therefore be the result of clustering of the dipole directions between low and high multipoles as supported by Fig. 37. The low $p$-values can be explained by the alignment of dipole directions for multipoles extending all the way to $\ell = 1500$ correlated with directions for $\ell < 200$. The observed asymmetry is therefore not consistent with a model based on dipole modulation or power asymmetry located in one specific multipole range or for one given direction, but rather as a correlation of the dipole directions between $\ell < 200$ and $\ell > 200$. This correlation with lower multipoles is found to persist all the way to $\ell_{\max} = 1500$.

An advantage of the directional analysis performed here is that it focuses on a central issue for tests of deviation from isotropy – whether there is a preferred direction. Indeed, Bunn & Scott (2000) noted that the CMB may exhibit a pattern that cannot be identified from the power spectrum, but which would indicate some non-trivial large-scale structure. Evidence for the close correlation and alignment of directions on different angular scales may present a signature of broken statistical isotropy, since in the standard model, these directions should all be independent random variables. In this context, we do not quote a specific direction for such asymmetry here since our results indicate a clustering of angles between different multipoles, but not necessarily that all multipoles are clustered about one specific direction. However, crucially we have shown that the measured clustering is driven by the correlations of directions between higher and lower multipoles.

Some of the analyses in other sections of the paper focus on dipolar modulation, a specific model for a dipolar power enhancement of the statistically isotropic CMB field towards a preferred direction of the sky, and use methods optimized for the detection of such a signal. While the results of Sect. 6.6 show no detection of the clustering of directions, there is no clear contradiction with the results presented here, since they are based on tests for $a_{\ell m}$ correlations between different multipoles as expected in the dipolar modulation model. The clustering analysis presented here is a model-independent test for deviations from statistical isotropy which could induce very different correlation structure. It is therefore sensitive to other forms of asymmetry, such as the addition of power in one part of the sky or more general phase correlations.

### 6.6. Rayleigh statistic: QML analysis

Results from Sect. 6.5 and in PCIS13 suggest that, beyond a dipole modulation of power on large angular scales, some form of directional asymmetry continues to small scales. There are also indications from Sect. 6.5 that the directions of dipolar asymmetry are correlated between large and small angular scales. Since the nature of the asymmetry is unknown we use the RS, a generic test for directionality that makes minimal assumptions about the nature of the asymmetry. This statistic has been used both in previous CMB studies (Stannard & Coles 2005) and other areas of cosmology (Scott 1991). In our context, for a statistically isotropic sky this statistic is identical to a three-dimensional random walk. The implementation here incorporates all information pertaining to modulation, not just the direction. The approach in this section differs from that of Sect. 6.5 in the method of reconstructing power, the choice of binning, and the choice of how to weight directions in each bin. Another important difference is that Sect. 6.5 only considers the direction of dipolar asymmetry and does not take into account its amplitude.

The statistic is cumulative and thus narrowing down the specific scales from which a signal may be originating is a non-trivial task. However, it is the case that all statistics that measure this form of asymmetry (dipole modulation or large-scale clustering of power) are in some way cumulative and so we will not worry about this issue any further. Another disadvantage of this approach is that it will generally be *less* powerful than a test that uses a specific model for the directionality. Again, this is a distinction shared when one compares any non-parametric versus parametric statistic.

The construction of the statistic is as follows.

1. Beginning with the estimator from Eqs. (44) and (45), compute the following binned quantities for the data and simulation:

$$\tilde{X}_{0,\,\ell} = \frac{6}{f_{10}} \frac{\sum_m A_{\ell m}\left(T^*_{\ell m}T_{\ell+1\,m} - \left\langle T^*_{\ell m}T_{\ell+1\,m}\right\rangle\right)}{\delta C_{\ell\ell+1}F_\ell F_{\ell+1}(\ell+1)}, \tag{60}$$

$$\tilde{X}_{1,\,\ell} = \frac{6}{f_{11}} \frac{\sum_m B_{\ell m}\left(T^*_{\ell m}T_{\ell+1\,m+1} - \left\langle T^*_{\ell m}T_{\ell+1\,m+1}\right\rangle\right)}{\delta C_{\ell\ell+1}F_\ell F_{\ell+1}(\ell+1)}. \tag{61}$$

For each $\ell$ this computes the coupling of $\ell$ to $\ell + 1$. We emphasize that this is a very natural choice of binning the estimator, since any parameter that is dipole modulated will lead to coupling of $\ell$ to $\ell \pm 1$ modes, albeit with different $\ell$-weightings (below we describe why this is not an important issue).

2. Construct a three-dimensional vector out of the three estimators for both the data and the simulations[11], as defined by Eqs. (47)–(49).
3. Compute the mean amplitude from simulations and divide all vectors (data and simulations) by this amplitude. This choice ensures that each vector is treated equally, since we have no a priori reason to weight some scales more than others.
4. Add this new vector to the previous vector. If this is the first time going through this process the previous vector is the zero vector.
5. Repeat with $\ell \rightarrow \ell + 1$. Note that the statistics of this process are identical to a three dimensional random walk.

Given that a dipole modulation amplitude of roughly $3\sigma$ significance is known to exist at low $\ell$ (before a posteriori correction), one would expect a similar level of detection of asymmetry to be determined by the RS. Indeed, we find that asymmetry is present out to $\ell \approx 240$. Figure 38 (top) presents the $p$-values derived when the RS is computed as a function of $\ell_{\rm max}$ from $\ell = 2$. The minimum $p$-value obtained by the data is 0.1–0.2%, to be compared to the value of 0.9–1.0% obtained for the dipole modulation amplitude at $\ell_{\rm max} = 67$. The direction preferred by the data for $\ell_{\rm max} \approx 240$ is $(l, b) = (208°, -29°)$, which is approximately 20° away from the dipole modulation direction determined to $\ell \approx 64$.

We correct for a posteriori statistics using the same procedure as in Sect. 6.3. Specifically, we count how often simulations find asymmetry in the range $10 \leq \ell \leq \ell_{\rm max}$ that is more significant than that found for the data. From Fig. 39 it is clear that generic asymmetry at the significance level found in our CMB sky occurs about 6% or 8% of the time (depending on the range of $\ell$ one decides to search over).

While the PTE here is not very low, it is nevertheless somewhat lower than for the usual dipole modulation test. Hence, it seems worth exploring whether any of this signal comes from higher multipoles. Therefore we compute the RS starting at $\ell_{\rm min} = 100$, to avoid the influence of asymmetry at lower $\ell$. The lower panel of Fig. 38 presents the corresponding $p$-values as a function of $\ell_{\rm max}$. There is a striking similarity with the lower panel of Fig. 30. It is clear that, even in the absence of a posteriori correction, we find no significant asymmetry at larger $\ell$. Hence most of the signal we are seeing in Fig. 38 (top) is due to the usual low-$\ell$ asymmetry.

We would like to stress that the results here are very similar to the results of the previous section. For each of the statistics used we are simply asking whether there is significant coupling of $\ell$ with $\ell \pm 1$ modes. The details of how to optimally combine these couplings for a given $\ell$ range depends on whether we are talking about dipole modulation or directionality (or some other related test, e.g., variance asymmetry). These details will change the range of scales over which the strongest signal in the data is found.

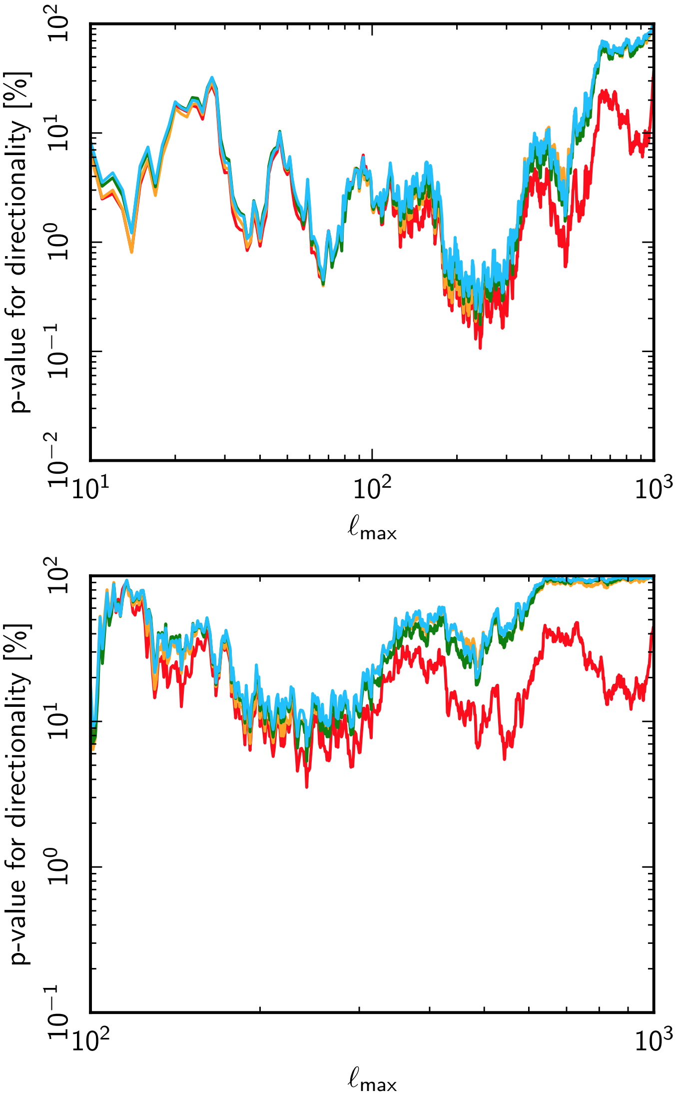

**Fig. 38.** Rayleigh statistic $p$-values determined from the QML analysis as a function of $\ell_{\rm max}$ for the `Commander` (red), `NILC` (orange), `SEVEM` (green), and `SMICA` (blue) data sets, with (*top panel*) $\ell_{\rm min} = 2$ and (*bottom panel*) $\ell_{\rm min} = 100$. The general pattern of peaks is very similar to that in Fig. 30. We emphasize that the statistic here is cumulative and as such trends in the curves can be misleading.

## 7. Sensitivity of anomalies to enhanced sky coverage

One of the critical aspects in searching for anomalous features in sky maps is to ensure that the region being investigated constitutes a fair and unbiased sample. Since many of the claimed anomalies are on large angular scales, this implies that minimal masking should be applied to the data. However, residual foregrounds then become a significant consideration. The masks applied to the four component-separated maps studied in the bulk of this paper have been defined at high resolution, and then conservatively degraded for lower resolution studies. Such a procedure inevitably reduces the sky coverage available for analysis, and can be particularly problematic if significant structures are aligned by chance with the masked regions. Indeed, the WMAP team (Bennett et al. 2011) have drawn attention to several such features in their ILC reconstruction of the CMB sky, and these are clearly also present in the *Planck* `Commander`, `NILC`, `SEVEM`, and `SMICA` sky maps. A large cold spot is seen

---

[11] Note that here we have not specified what $\delta C_{\ell\ell+1}$ is (it is fully specified by choosing a parameter $X$ to modulate). This is because we have decided to weight each $\ell$ equally and thus any strictly positive choice for $\delta C_{\ell\ell+1}$ will be equivalent, since in step 3 we force the mean length of the vectors at each $\ell$ to be equal.

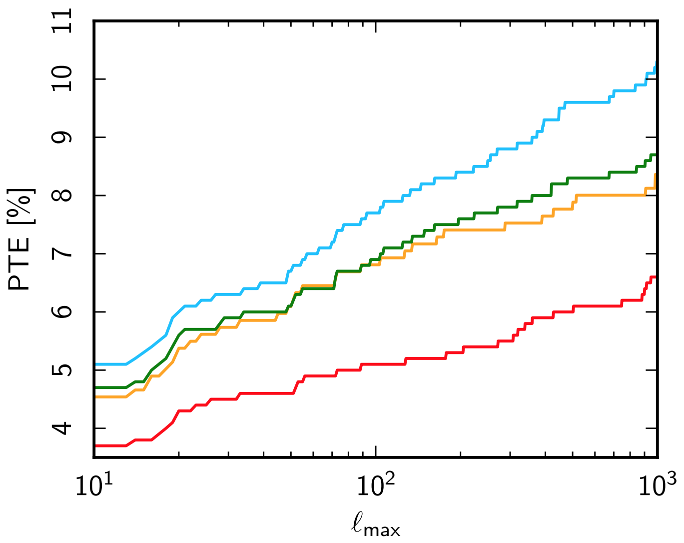

**Fig. 39.** Probability to exceed (PTE) the $p$-value of the signal from the `Commander` (red), `NILC` (orange), `SEVEM` (green), and `SMICA` (blue) data at $\ell = 230$–$240$ (which is the multipole range with the most significant deviation) when searching over a range of multipoles up to $\ell_{\rm max}$, for the RS determined from the QML analysis. Much like the equivalent curve for dipole modulation, the PTE appears to grow approximately logarithmically with $\ell_{\rm max}$.

near to the Galactic centre, a significant fraction of which lies within the common mask at any resolution. However, despite its location and visual impression, the feature is neither likely to be attributable to residual foreground emission, nor is it inconsistent with the ΛCDM model (Gott et al. 2007). In addition, four elongated cold fingers stretching from near the Galactic equator to the south Galactic pole are seen, although no equivalent features are evident in the northern sky. Bennett et al. (2011) have noted that the alignment of the $\ell = 2$ and $\ell = 3$ multipoles (Tegmark et al. 2003) seems to be intimately connected with these large-scale cool fingers and the intervening warm regions. One of the latter also corresponds to the well-known "Bianchi $\text{VII}_\text{h}$" main lobe originally found in Jaffe et al. (2005).

Although we would ideally pursue full sky analyses, we prefer to remain mindful of the influence of residual foregrounds, but still seek to minimize the extent of any mask applied for analysis. In this context, and specifically for large-angular-scale studies, we consider the properties of an additional estimate of the CMB sky, also generated using the `Commander` component separation methodology. In particular, we note that the *Planck* low-$\ell$ likelihood analysis (Planck Collaboration XI 2016) uses the temperature solution from this study, degraded to a resolution of $N_{\rm side} = 16$. The `Lkl-Commander` map, as we now refer to it, is initially derived from input data sets (32 bands) at 1° FWHM resolution and $N_{\rm side} = 256$. This includes *Planck* individual detector and detector set maps from 30–857 GHz, the 9-year WMAP observations between 23 and 94 GHz, and the 408 MHz sky survey (Haslam et al. 1982), whereas the `Commander` map described in Planck Collaboration IX (2016) includes *Planck* data alone. It is believed that the 32-band solution is better (on large angular scales) than the *Planck*-only map, because the larger number of input frequencies allows more detailed foreground modelling, and in particular the separation of the low-frequency foregrounds into synchrotron, free-free, and spinning dust components. An associated confidence mask (hereafter $\texttt{LklT}_{256}\texttt{93}$) is then defined based on a goodness-of-fit measure per pixel, corresponding to a rejection of 7.3% of the pixels on the sky. A detailed discussion of these results can be found in Planck Collaboration X (2016).

**Table 27.** Lower-tail probability for the variance, skewness, and kurtosis of the `Lkl-Commander` map.

| Mask | Probability [%] | | |
|---|---|---|---|
| | Variance | Skewness | Kurtosis |
| $\texttt{LklT}_{16}\texttt{94}$ . . . . . . . . . . . . . . . . | 7.0 | 1.5 | 94.0 |
| $\texttt{UT}_{16}\texttt{58}$ . . . . . . . . . . . . . . . . . | 0.7 | 19.9 | 82.5 |

We now consider the implications of using the `Lkl-Commander` map for studies of several large-angular-scale anomalies observed in previous sections, in particular since the larger sky coverage permitted by this data set should constitute a better sample of the Universe. Note that, at the resolutions of interest for the following analyses, the noise level is negligible (even accounting for the WMAP contribution) and should not have significant impact on the results. The exact details of the noise contribution to simulations is therefore unimportant.

### 7.1. Variance, skewness, and kurtosis

We begin by estimating the variance, skewness, and kurtosis of the CMB. We apply the unit variance estimator to the `Lkl-Commander` map, and specifically to the version used in the low-$\ell$ likelihood analysis, which is smoothed to 440′ FWHM at a resolution of $N_{\rm side} = 16$. A corresponding low-$\ell$ mask is generated by a simple degrading of the mask at $N_{\rm side} = 256$, then setting those $N_{\rm side} = 16$ pixels with a value less than 0.5 to zero and all others to unity. The resultant low-$\ell$ likelihood mask rejects only 6.4% of the sky. We compare the results for both this mask (also to be referred to as $\texttt{LklT}_{16}\texttt{94}$), and the standard common mask at this resolution ($\texttt{UT}_{16}\texttt{58}$). The results are summarized in Table 27 and show that, when using the low-$\ell$ likelihood mask, the lower tail probability for the variance is 7.0%. This value is higher than the corresponding values for the component separated maps as shown in Table 12. In addition the skewness and kurtosis are less consistent with Gaussianity than the component separated maps. However, when using the standard common mask at $N_{\rm side} = 16$, the lower tail probability of the variance, skewness, and kurtosis become more compatible with those derived earlier.

There are two possible explanations for this behaviour. Either the variance of the CMB in the region close to the Galactic plane is intrinsically high, perhaps due to the presence of the various features noted above, or the presence of residual foregrounds increases the variance of the map. In order to attempt to distinguish between these options, we again apply the unit variance estimator to the standard component-separated maps[12], but this time utilising the low-$\ell$ mask. Although the component-separated maps are likely to contain

---

[12] Note that the `SEVEM` maps used in this section have been inpainted within 3% of the sky towards the Galactic centre using a simple diffusive inpainting algorithm. This prevents residual foreground contamination from propagating to neighbouring regions when downgrading the map. The other component-separated maps are not pre-processed in this way since some form of inpainting of the most contaminated regions was already implemented as part of the component separation algorithms.

**Table 28.** Lower-tail probability for the variance, skewness, and kurtosis of the `Lkl-Commander` map compared to the component separated maps, obtained using the low-$\ell$ likelihood mask $\texttt{LklT}_{16}\texttt{94}$.

| Map | Probability [%] | | |
|---|---|---|---|
| | Variance | Skewness | Kurtosis |
| `Lkl-Commander` | 7.0 | 1.5 | 94.0 |
| `Commander` | 7.7 | 1.9 | 96.0 |
| `NILC` | 9.6 | 5.0 | 94.4 |
| `SEVEM` | 7.4 | 4.8 | 94.3 |
| `SMICA` | 7.7 | 3.7 | 93.7 |
| `SEVEM-100` | 8.4 | 0.4 | 97.9 |
| `SEVEM-143` | 7.7 | 3.7 | 95.5 |
| `SEVEM-217` | 8.3 | 0.7 | 95.2 |

some foreground contamination in the regions omitted by application of the $\mathrm{UT}_{16}58$ mask, it is appropriate to recall that this was constructed in a conservative way, and may also mask parts of the sky where the level of residual foregrounds can be considered negligible. In addition, we investigate the cleaned frequency maps produced by the `SEVEM` algorithm in order to test for the presence of frequency-dependent residual foregrounds. The results of the unit variance estimator analysis are summarized in Table 28.

All of the component separated maps show an increase in the lower tail probability from about 0.5% when the $\texttt{UT}_{16}\texttt{58}$ mask is applied to roughly 7% for the $\texttt{LklT}_{16}\texttt{94}$ mask. The small variations in results for the different maps may be attributable to the presence of residual foregrounds close to the Galactic plane. However, the increased probabilities can also be explained by the presence of CMB structures with higher variance within that region which is not rejected by the less conservative mask. Indeed, since the component-separated maps are affected by different residual foregrounds, if the source of the changes in probabilities is due only to the residual foregrounds, then we would expect a larger dispersion than what is observed. We also note that when we apply the low-$\ell$ likelihood mask the skewness and kurtosis values are shifted towards more extreme values. This implies that the sky signal is less Gaussian for the larger sky fraction, despite the results remaining compatible with the $\Lambda$CDM model assumed for the null tests. Both `Commander` maps are noteworthy in this regard.

An important issue is whether the changes in the statistics can simply be attributed to differences in the masks. We determine how many simulations show an increase in variance at least as large as that seen for the `Lkl-Commander` map when comparing the values derived for the $\mathrm{UT}_{16}58$ and low-$\ell$ likelihood masks. Similarly, we determine how many simulations have increased skewness or kurtosis values with shifts at least as large as observed. When the three statistics are considered separately, the fraction of simulations that indicate such changes are 7.6%, 4.3%, and 13.9% for the variance, skewness, and kurtosis, respectively. Of course, such subsets of the simulations also include cases where a large shift in the statistic is observed, but the statistic would not be considered anomalous for either mask. If we also impose the requirement that the simulations have these shifts for all three quantities simultaneously, then only 2 maps from 1000 are found. Of course, such a requirement is rather strong, and at this stage we are likely to be approaching the limits of what can be said based on model-independent null tests. Indeed, in order to assess whether these results are sensitive to a posteriori choices, we repeat the analysis but successively take each simulation as the reference. Thus, for each simulation the shift in the variance, skewness, and kurtosis is computed and then we determine how many times we find a case in which two or less of the remaining simulations simultaneously show larger shifts for the three moments. We find that 48 maps from 1000 satisfy these conditions. Given this, it is difficult to draw strong conclusions about the significance or otherwise of the mask-related changes in variance.

**Table 29.** Probabilities to exceed the observed values of the $\chi^2$ statistics for the `Lkl-Commander` and `Commander` maps at $N_{\mathrm{side}} = 64$.

| Function | Probability [%] | | |
|---|---|---|---|
| | `Lkl-Comm.`[a] | `Lkl-Comm.`[b] | `Comm.`[b] |
| 2-pt. | 84.3 | 97.1 | 97.2 |
| Pseudo-coll. 3-pt. | 76.8 | 92.1 | 92.1 |
| Equil. 3-pt. | 96.5 | 74.0 | 74.0 |
| Rhombic 4-pt. | 94.5 | 65.0 | 64.6 |

**Notes.** (a) low-$\ell$ mask, $\texttt{LklT}_{64}\texttt{92}$. (b) Common mask, $\texttt{UT}_{64}\texttt{67}$.

## 7.2. N-point correlation functions

The connection between sky coverage and the observed structure of the 2-point correlation function for large angular separations has previously been discussed in the literature, in particular in connection with the $S_{1/2}$ statistic discussed in Sect. 5.2. Bennett et al. (2011) consider that the use of a Galactic mask when computing these quantities is sub-optimal, and note that a full-sky computation of the 2-point correlation function from the 7-year WMAP ILC map lies within the 95% confidence region determined by simulations of their best-fit $\Lambda$CDM model over all angular separations. However, Copi et al. (2009) suggest that the origin of the inconsistencies between the full-sky and cut-sky large-scale angular correlations remains unknown, and that the observed discrepancies may indicate that the Universe is not statistically isotropic on these scales. We therefore consider the $N$-point correlation functions, and related statistics, of the `Lkl-Commander` map to contribute to this debate.

We compare results computed for both the `Lkl-Commander` and `Commander` maps at $N_{\mathrm{side}} = 64$ after smoothing to a FWHM of $160'$. A mask is constructed for the `Lkl-Commander` map by degrading the $\texttt{LklT}_{256}\texttt{93}$ mask to $N_{\mathrm{side}} = 64$ and setting all resulting pixels with a value less than 0.5 to zero, with the remainder set to unity. The $\texttt{LklT}_{64}\texttt{92}$ mask retains 92% of the sky, to be compared to the 67% usable sky coverage allowed by the $\texttt{UT}_{64}\texttt{67}$ common mask at this resolution.

The results are presented in Fig. 40 where we compare the $N$-point functions for the data and the mean values estimated from 1000 `Commander` simulations. The probabilities for obtaining values of the $\chi^2$ statistic for the *Planck* fiducial $\Lambda$CDM model at least as large as the observed values are provided in Table 29. For the estimation of the probabilities, we use the same set of 1000 `Commander` simulations for both versions of the `Commander` data. As noted previously, the details of the simulations for such highly smoothed data is essentially unimportant. We also provide an analysis of the `Lkl-Commander` map using the common mask to enable a direct comparison with the analysis of the `Commander` map. In this latter case, the results for both maps are in excellent agreement. However, the `Lkl-Commander` map is more consistent with simulations when the $\texttt{LklT}_{64}\texttt{92}$

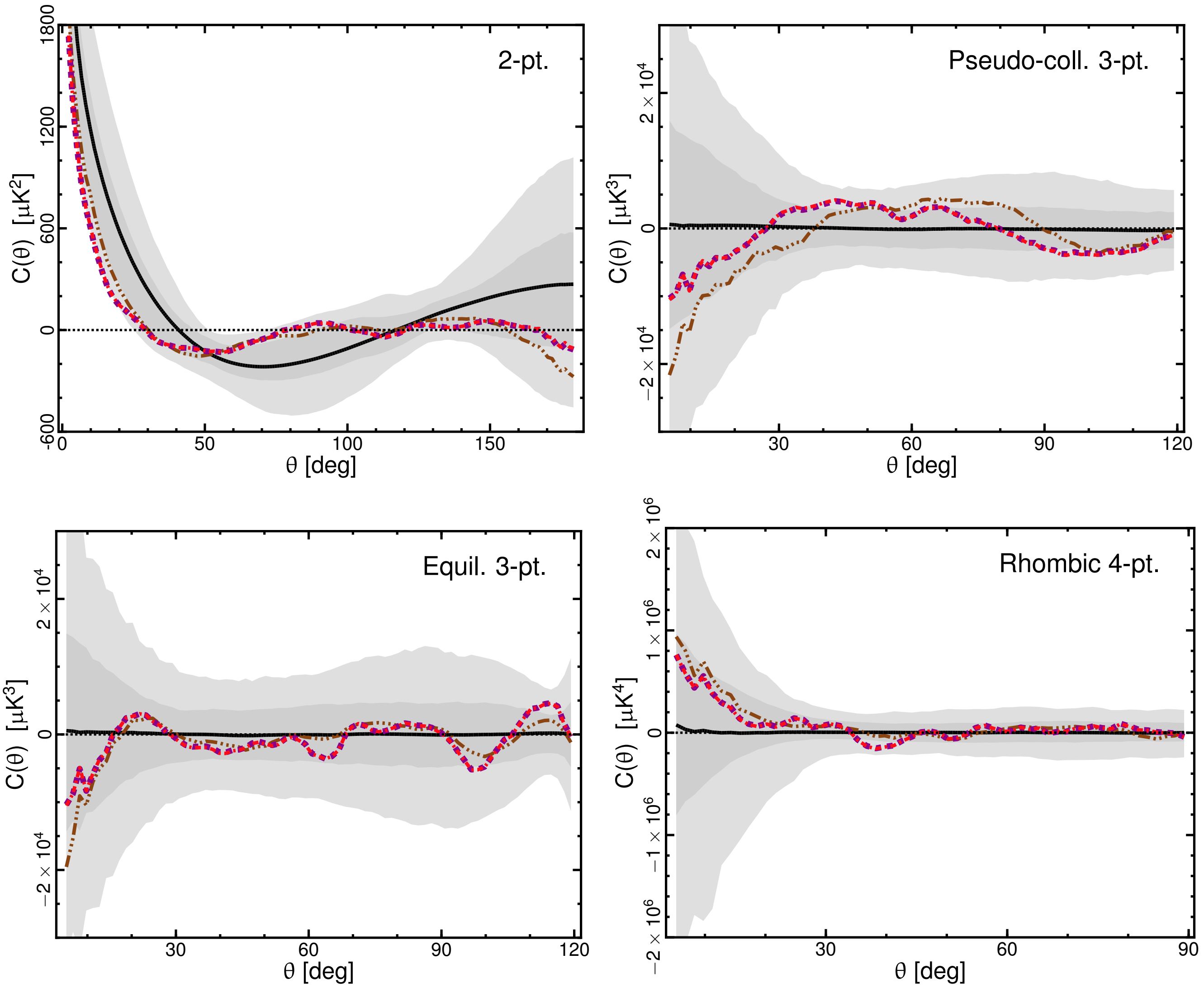

**Fig. 40.** *N*-point correlation functions determined from the $N_{\rm side} = 64$ *Planck* CMB 2015 temperature estimates. Results are shown for the 2-point, pseudo-collapsed 3-point (*upper left and right panels*, respectively), equilateral 3-point, and connected rhombic 4-point functions (*lower left and right panels*, respectively). The brown three dot-dashed, purple dashed, and red dot-dashed lines correspond to the `Lkl-Commander` map analysed using the low-$\ell$ and common masks and the `Commander` map analysed using the common mask, respectively. Note that the dashed and dot-dashed lines lie on top of each other. The black solid line indicates the mean for 1000 MC simulations. The shaded dark and light grey regions indicate the 68% and 95% confidence regions, respectively, estimated using 1000 `Commander` simulations. See Sect. 4.3 for the definition of the separation angle $\theta$.

mask is adopted for the 2-point and pseudo-collapsed 3-point functions, but less consistent for the equilateral 3-point and rhombic 4-point function results. Nevertheless, the results are generally in agreement with expectations for a Gaussian, statistically isotropic model of the CMB fluctuations.

The increased consistency of the 2-point function with simulations when analysing a larger sky fraction is consistent with the observations in Copi et al. (2009). We therefore quantify this further by determining the statistical quantities introduced in Sect. 5.2 for the `Lkl-Commander` map. In particular, we reassess the lack of correlation determined previously for large angular scales. It is evident from Table 30 that the results for the $S_{1/2}$ and $\chi^2_0$ statistics are less anomalous when the low-$\ell$ mask is applied. Moreover, the global $p$-value for the $S(x)$ statistic is substantially smaller.

**Table 30.** Probabilities for obtaining values of the $S_{1/2}$ and $\chi^2_0$ statistics for the simulations at least as large as the observed values of the statistic estimated from the `Lkl-Commander` and `Commander` maps using the `LklT`$_{64}$`92` and `UT`$_{64}$`67` masks, respectively. We also show the corresponding estimation of the global $p$-value for the $S(x)$ statistic.

| | Probability [%] | |
|---|---|---|
| Statistic | `Lkl-Comm.` | `Comm.` |
| $S_{1/2}$ . . . . . . . . . . . . . . . . . . . . | 97.1 | 99.5 |
| $S(x)$ (global) . . . . . . . . . . . . . | 90.9 | 97.7 |
| $\chi^2_0(\theta > 60°)$ . . . . . . . . . . . . . . | 95.7 | 98.1 |

We also repeat the conventional $\chi^2$ analysis but constraining the computations to the two separate ranges defined by $\theta < 60°$ and $\theta > 60°$. The results of these studies are shown in Table 31. The analysis for seperation angles $\theta > 60°$ indicates that the unusually good fit of the observed 2-point function to the mean 2-point function determined for the $\Lambda$CDM model is

**Table 31.** Probabilities for obtaining values of the $\chi^2$ statistic for the simulations at least as large as the observed values of the statistic estimated from the `Lkl-Commander` and `Commander` maps using the `LklT`$_{64}$`92` and `UT`$_{64}$`67` masks, respectively.

| Statistic | Probability [%] | |
|---|---|---|
| | `Lkl-Comm.` | `Comm.` |
| $\chi^2(\theta < 60°)$ | 52.9 | 91.5 |
| $\chi^2(\theta > 60°)$ | 96.5 | 96.8 |

**Table 32.** Probabilities for obtaining values of the $\chi^2$ statistic and ratio of $\chi^2$ of the $N$-point functions for the *Planck* fiducial ΛCDM model at least as large as the observed values of the statistic on the northern and southern ecliptic hemispheres estimated from the `Lkl-Commander` and `Commander` maps using the `LklT`$_{64}$`92` and `UT`$_{64}$`67` masks, respectively.

| Hemisphere | Probability [%] | |
|---|---|---|
| | `Lkl-Comm.` | `Comm.` |
| 2-point function | | |
| Northern | 98.7 | 89.7 |
| Southern | 29.4 | 80.5 |
| $\chi^2$-ratio | 93.3 | 22.6 |
| Pseudo-collapsed 3-point function | | |
| Northern | 99.4 | >99.9 |
| Southern | 14.9 | 35.1 |
| $\chi^2$-ratio | 98.6 | 98.8 |
| Equilateral 3-point function | | |
| Northern | 99.9 | 98.6 |
| Southern | 47.6 | 45.7 |
| $\chi^2$-ratio | 94.4 | 86.6 |
| Rhombic 4-point function | | |
| Northern | 99.8 | 99.7 |
| Southern | 24.5 | 22.8 |
| $\chi^2$-ratio | 97.8 | 97.3 |

independent of the mask used in the analysis. Conversely, the results for the angles $\theta < 60°$ indicate a strong dependence on the mask. It appears that the decreased significance of the $\chi^2$ statistic for the 2-point function of the `Lkl-Commander` map reported in Table 29 is related mainly to correlations in the data for separation angles smaller than 60°.

Our results do appear to indicate that computations made on larger sky fractions increase the consistency of the 2-point function with simulations. We therefore also test how the hemispherical asymmetry observed previously is affected. The results for the ecliptic frame are presented in Table 32. We find that the asymmetry is larger for the `Lkl-Commander` map than for the `Commander` map in the case of the 2-point function, but does not change substantially for the 3-point and 4-point functions.

## *7.3. Dipole modulation and directionality*

### 7.3.1. Variance asymmetry

Here we apply the local-variance analysis of Sect. 6.1 to the `Lkl-Commander` map and compare the results with those of the `Commander` map. Contrary to the analysis of Sect. 6.1, where full-resolution ($N_{\rm side} = 2048$) maps were used, here the `Commander` map is downgraded to $N_{\rm side} = 256$ in order to consistently compare the results for both maps. The simulations used for estimating the significance levels are also downgraded to the same resolution, and convolved with the corresponding beam function. Otherwise, the procedure is identical to the one described in Sect. 6.1, e.g., the same number of discs has been used to construct the local-variance maps. Here we only present the results when no high-pass filtering has been applied to the maps; this is to avoid confusion as our objective in this section is only to compare the general properties of the `Lkl-Commander` map to those of the standard component-separated maps.

**Table 33.** $p$-values for the variance asymmetry measured by different discs from the *Planck* 2015 `Lkl-Commander` and `Commander` temperature solutions using the `LklT`$_{256}$`93` and `UT`$_{256}$`73` masks, respectively.

| Disc radius [°] | $p$-value [%] | |
|---|---|---|
| | `Lkl-Comm.` | `Comm.` |
| 4 | 0.2 | 0.7 |
| 6 | 0.4 | 0.3 |
| 8 | 0.3 | 0.1 |
| 10 | 0.3 | 0.7 |
| 12 | 0.3 | 0.8 |
| 14 | 0.5 | 1.5 |
| 16 | 0.6 | 1.9 |
| 18 | 0.8 | 2.7 |
| 20 | 1.1 | 3.7 |

**Notes.** The values represent the fraction of simulations with local-variance dipole amplitudes larger than those inferred from the data. No high-pass filtering has been applied to the maps.

**Table 34.** Local-variance dipole directions measured by 8° discs for the *Planck* 2015 `Lkl-Commander` and `Commander` temperature solutions.

| Method | $(l, b)$ [°] |
|---|---|
| `Lkl-Comm.` | (225, −28) |
| `Commander` | (214, −24) |

Table 33 summarizes the significance levels measured by our variance asymmetry analysis using discs of different radii, for the *Planck* 2015 `Commander` and `Lkl-Commander` temperature maps. The $p$-values represent the fraction of simulations with local-variance dipole amplitudes larger than those inferred from the data. We in addition present in Table 34 the preferred variance asymmetry directions for both maps using 8° discs.

Our results show consistency between the two maps. The small change in the preferred direction is expected from the change in the mask, and agrees specifically with the directions found by the analysis of the QML dipole modulation analysis in Sect. 7.3.3. One interesting observation is that the large variance asymmetry significance is now extended to cases where larger discs are used. Note that no high-pass filtering has been applied in the present analysis, and therefore $p$-values inferred from the `Commander` map increase with the disc size. As explained in Sect. 6.1, the low observed significance levels for larger discs is due to the cosmic variance associated with the largest-scale modes. The observed increase in the significance levels for the `Lkl-Commander` map is therefore interestingly consistent with this picture; the mask in this case is smaller and therefore a larger fraction of the sky is available. This in turn provides more data on the largest scales, and therefore lowers the impact of the cosmic variance.

### 7.3.2. Dipole modulation: pixel-based likelihood

Table 35 presents constraints on the dipole modulation model as derived from the `Lkl-Commander` map and the `LklT`$_{32}$`93` mask that includes 93% of the sky, updating the results from Sect. 6.2

**Table 35.** Summary of dipole modulation results at a smoothing scale of 5° for the *Planck* 2015 `Lkl-Commander` and `Commander` temperature solutions, as derived by the brute-force likelihood given by Eq. (43).

| Method | 2013 | 2015 |
|---|---|---|
| Dipole modulation amplitude, $\alpha$ | | |
| `Lkl-Comm.` . . . . . | ··· | $0.059 \pm 0.020$ |
| `Commander` . . . . . | $0.078 \pm 0.021$ | $0.066 \pm 0.021$ |
| Dipole modulation direction, $(l, b)$ [°] | | |
| `Lkl-Comm.` . . . . . | ··· | $(223, -17) \pm 23$ |
| `Commander` . . . . . | $(227, -15) \pm 19$ | $(230, -16) \pm 24$ |
| Power spectrum amplitude, $q$ | | |
| `Lkl-Comm.` . . . . . | ··· | $0.970 \pm 0.025$ |
| `Commander` . . . . . | ··· | $0.961 \pm 0.025$ |
| Power spectrum tilt, $n$ | | |
| `Lkl-Comm.` . . . . . | ··· | $0.068 \pm 0.045$ |
| `Commander` . . . . . | ··· | $0.082 \pm 0.043$ |

**Notes.** The former results were derived using the $\texttt{LklT}_{32}\texttt{93}$ mask, whereas the latter are those determined previously in Sect. 6.2.

**Table 36.** Summary of the dipole modulation results for the range $\ell \in [2, 64]$ determined from the *Planck* 2015 `Lkl-Commander` and `Commander` temperature solutions, as derived by the QML estimator defined in Sect. 6.3 using the $\texttt{LklT}_{256}\texttt{93}$ and `UT78` masks, respectively.

| Method | $A$ | Direction<br>$(l, b)$ [°] |
|---|---|---|
| `Lkl-Comm.` . . . . . | $0.058^{+0.022}_{-0.012}$ | $(227, -28) \pm 26$ |
| `Commander` . . . . . | $0.063^{+0.025}_{-0.013}$ | $(213, -26) \pm 28$ |

for the `Commander` map. We find that all previously reported results are robust with respect to data selection and sky coverage. In particular, the best-fit dipole modulation amplitude at 5° FWHM is 5.9% in the `Lkl-Commander` map, and is thus stable to within about $0.3\sigma$ when increasing the sky fraction from 78% to 93%. Likewise, the marginal low-$\ell$ power spectrum amplitude, $q$, shifts upward by $0.4\sigma$, and the power spectrum tilt, $n$, downward by $0.3\sigma$, for the same sky fraction increases.

To assess the statistical significance of these shifts, we compare with Gaussian statistics, creating two Gaussian random vectors with 78 and 93 elements, respectively, where the first 78 elements of the latter vector are identical to the first vector. From these, we compute the difference between the two means, after normalizing each so that their individual errors in the mean are unity. Repeating this simple calculation $10^5$ times, we find that 48% of all Gaussian realizations observe shifts larger than $0.3\sigma$, and 34% observe shifts larger than $0.4\sigma$. Thus, the parameter differences due to the different data selection and sky fractions reported above are consistent with expectations from random Gaussian statistics.

#### 7.3.3. Dipole modulation: QML analysis

We also repeat the QML dipole modulation analysis of Sect. 6.3 for the `Lkl-Commander` map and corresponding mask. Table 36 summarizes the results of the low-$\ell$ dipole modulation for the `Lkl-Commander` temperature solution, compared with the `Commander` map.

The best-fit modulation amplitude for `Lkl-Commander` is 5.8% and the small 0.5% shift from the `Commander` best-fit amplitude corresponds to a decrease of approximately $0.4\sigma$. These results mirror very closely the results found above for the pixel-based likelihood approach to dipole modulation, as expected, and the observed shifts are perfectly consistent with those expected from the change in the mask.

**Table 37.** Amplitude ($A$) and direction of the dipole modulation in Galactic coordinates as estimated for the multipole range $\ell \in [2, 64]$ using the BipoSH analysis on `Lkl-Commander` and `Commander` maps. The former results were derived using the $\texttt{LklT}_{256}\texttt{93}$ mask; the latter are those determined previously in Sect. 6.4.

| Method | $A$ | Direction<br>$(l, b)$ [°] |
|---|---|---|
| `Lkl-Comm.` . . | $0.063 \pm 0.021$ | $(234, -27) \pm 31$ |
| `Commander` . . | $0.067 \pm 0.023$ | $(230, -18) \pm 31$ |

#### 7.3.4. Bipolar spherical harmonics

We next perform a dipole modulation analysis on the `Lkl-Commander` temperature map using the BipoSH formalism from Sect. 6.4. The dipole modulation amplitude inferred from the analysis is smaller that that deduced from analysing the `Commander` map as seen in Table 37. However, it should be noted that the probability for simulations to yield a dipole modulation amplitude equal to or greater than the amplitude inferred from data is 0.4%, which is smaller by a factor of approximately 2.4 as compared to the $p$-value inferred from analysis on `Commander`. The reduction in the dipole amplitude and the enhanced significance can both be attributed to the reduced power bias which is a result of the increased sky coverage.

### 7.4. Summary

Using a larger sky fraction in our analyses leads to small changes in the results related to large-angular-scale anomalies, but these are essentially consistent with expectations from random Gaussian statistics. In particular, the asymmetry in power on the sky, as parameterized by a dipole modulation model, is robust to mask changes.

## 8. Polarization analysis

As previously discussed in Sect. 2, large angular-scale CMB fluctuations in the *Planck* polarization data have been suppressed by a post-processing high-pass filter to minimize the impact of systematic artefacts. Therefore, no polarization results concerning CMB statistical anomalies on such scales are presented in this paper. In addition, a noise mismatch between simulations and data also limits our ability to study polarization more generally. Nevertheless, a local analysis of the polarization data for stacked patches of the sky can still be performed, in order to test the statistical properties of the CMB anisotropies. In this case, the stacking procedure mitigates the impact of the small-scale noise and potential systematic effects.

Traditionally, the Stokes parameters $Q$ and $U$ are used to describe the CMB polarization anisotropies (e.g., Zaldarriaga & Seljak 1997). Such quantities are not rotationally invariant, thus for the stacking analysis it is convenient to consider a local rotation of the Stokes parameters, resulting in quantities denoted by $Q_r$ and $U_r$, as described in Sect. 8.1. Additionally, several other related quantities can be defined.

The polarization amplitude $P \equiv \sqrt{Q^2+U^2}$ and polarization angle $\Psi \equiv \frac{1}{2}\arctan(U/Q)$, are commonly used quantities in, for example, Galactic astrophysics. However, unbiased estimators of these quantities in the presence of anisotropic and/or correlated noise are hard to define (Plaszczynski et al. 2014). Of course, a direct comparison of the observed (noise-biased) quantity to simulations analysed in the same manner is possible, but we elect here to defer the study of this representation of the polarization signal, using maps of the polarization amplitude only to define peaks around which stacking can be applied.

The rotationally invariant quantities referred to as $E$ and $B$ modes are commonly used for the global analysis of CMB data. Although the $E$-mode maps are not analysed in detail here, they are considered qualitatively, so that it is appropriate to recall their construction. Since the quantities $Q \pm \mathrm{i}U$, defined relative to the direction vectors $\hat{\boldsymbol{n}}$, transform as spin-2 variables under rotations around the $\hat{\boldsymbol{n}}$ axis, they can be expanded as

$$(Q \pm \mathrm{i}U)(\hat{\boldsymbol{n}}) = \sum_{\ell=2}^{\infty}\sum_{m=-\ell}^{\ell} a_{\ell m}^{(\pm 2)}\ {}_{\pm 2}Y_{\ell m}(\hat{\boldsymbol{n}}), \tag{62}$$

where ${}_{\pm 2}Y_{\ell m}(\hat{\boldsymbol{n}})$ are the spin-weighted spherical harmonics and $a_{\ell m}^{(\pm 2)}$ are the corresponding harmonic coefficients. If we define

$$a_{\ell m}^{E} = \frac{1}{2}\left(a_{\ell m}^{(2)} + a_{\ell m}^{(-2)}\right), \tag{63}$$

$$a_{\ell m}^{B} = \frac{-i}{2}\left(a_{\ell m}^{(2)} - a_{\ell m}^{(-2)}\right), \tag{64}$$

then the invariant quantities are given by

$$E(\hat{\boldsymbol{n}}) = \sum_{\ell=2}^{\infty}\sum_{m=-\ell}^{\ell} a_{\ell m}^{E} Y_{\ell m}(\hat{\boldsymbol{n}}), \tag{65}$$

$$B(\hat{\boldsymbol{n}}) = \sum_{\ell=2}^{\infty}\sum_{m=-\ell}^{\ell} a_{\ell m}^{B} Y_{\ell m}(\hat{\boldsymbol{n}}). \tag{66}$$

### 8.1. Stacking around temperature hot and cold spots

The stacking of CMB anisotropies around peaks (hot and cold spots) on the sky yields characteristic temperature and polarization patterns that contain valuable information about the physics of recombination (Komatsu et al. 2011). Statistical analysis of stacked images differs from the other tests in this paper in several respects. First, peak-related new physics may be revealed that is difficult to find in a global analysis, for example, the non-Gaussian CMB cold spots predicted by a modulated preheating model (Bond et al. 2009). Secondly, stacking is a local operation, which naturally avoids mask-induced complications. Thus stacking can be used as a transparent and intuitive method to test the robustness of anomalies found with other methods. Alternatively, it can be applied as a quality indicator of the data at the map level.

Our stacking procedure is as follows. Hot (or cold) peaks are selected in the temperature map as local extrema with negative (or positive) second derivatives, and classified relative to a given threshold $\nu$ (in rms units of the temperature map). Since the spinorial components $Q$ and $U$ are expressed in a local coordinate system, we employ a configuration in which the Stokes parameters around a peak at the direction $\hat{\boldsymbol{n}}_0$ can be superposed (Kamionkowski et al. 1997). In particular, we use a locally defined rotation of the Stokes parameters that is written as:

$$Q_{\mathrm{r}}\left(\hat{\boldsymbol{n}};\hat{\boldsymbol{n}}_0\right) = -Q\left(\hat{\boldsymbol{n}}\right)\cos\left(2\phi\right) - U\left(\hat{\boldsymbol{n}}\right)\sin\left(2\phi\right), \tag{67}$$

$$U_{\mathrm{r}}\left(\hat{\boldsymbol{n}};\hat{\boldsymbol{n}}_0\right) = Q\left(\hat{\boldsymbol{n}}\right)\sin\left(2\phi\right) - U\left(\hat{\boldsymbol{n}}\right)\cos\left(2\phi\right), \tag{68}$$

where $\phi$ is the angle between the axis aligned along a meridian (pointing to the south by convention) in the local coordinate system centred on a peak at $\hat{\boldsymbol{n}}_0$ and the great circle connecting this peak to a position $\hat{\boldsymbol{n}}$. This definition decomposes the linear polarization into radial ($Q_{\mathrm{r}} > 0$) and tangential ($Q_{\mathrm{r}} < 0$) contributions around the peaks. This definition of $Q_{\mathrm{r}}$ is equivalent to the "tangential shear" used in weak lensing studies.

For visualization purposes, a flat patch around each peak is then extracted, and the average stacked image computed from the subset. A position on the sky at an angular distance $\theta$ from the central peak is labelled with the flat-sky coordinates

$$x = \varpi\cos\phi, \quad y = \varpi\sin\phi. \tag{69}$$

Here $\varpi = 2\sin(\theta/2) \approx \theta$ is the effective flat-sky radius. For the angular scales of a few degrees considered in the stacking analyses the difference between $\varpi$ and $\theta$ is negligible. We use $\varpi$ for analyses in the flat-sky approximation, and $\theta$ for analyses directly on the sphere.

The stacking process tends to provide an image with azimuthal symmetry about its centre, due to the almost uncorrelated orientations of the temperature peaks. The stacked images of temperature patches around hot spots selected above the null threshold for both the `Commander` data and a corresponding simulation are shown in the top row of Fig. 41. The observed patterns are in excellent agreement. Stacking around cold spots yields similar patterns but with flipped sign. Given the symmetry, it is often useful to consider the radial profile obtained by averaging the stacked image over the azimuthal angle $\phi$. Figure 42 shows such a profile determined from the stacked temperature image.

At this point, it is useful to consider the underlying physics represented by the various patterns in the stacked images. During recombination, the sound horizon extends an angle $\theta_{\mathrm{s}} = r_{\mathrm{s}}/D_{\mathrm{A}} \approx 0.011$ (0.61°), where $r_{\mathrm{s}} \approx 0.15$ Gpc is the size of the sound horizon at recombination and $D_{\mathrm{A}} \approx 14$ Gpc is the angular-diameter distance to the last scattering surface. To understand the ring patterns in the stacking image, projection effects must be taken into account. Firstly, all 3D modes with wavenumber $k \geq \ell/D_{\mathrm{A}}$ contribute to a 2D $\ell$-mode. More modes contribute to, and therefore enhance, the power at lower $\ell$. For the first acoustic peak, the net effect is a $\pi/4$ phase shift towards lower $\ell$, such that $\ell_{\mathrm{s}} \approx (\pi - \pi/4)/\theta_{\mathrm{s}} \approx 220$. The projected acoustic scale on the temperature map is of order $\theta_{\mathrm{s}}^{\mathrm{2D}} = \pi/\ell_{\mathrm{s}} = 0.014$ (0.81°). Secondly, the stacked 2D modes around peaks interfere with each other. The first dark ring appears at $1.22\theta_{\mathrm{s}}^{\mathrm{2D}} \approx 0.017$ (1.0°). The factor 1.22 is the ratio of the first minimum of the projection kernel, the Bessel function $J_0$, to the first minimum of the unprojected cosine wave.

The dark ring can also be regarded as a consequence of the correlation between $T$ and $-\nabla^2 T$. At the temperature maxima $-\nabla^2 T$ is positive, with an amplitude of order $T_{\mathrm{peak}}/(\theta_{\mathrm{s}}^{\mathrm{2D}})^2$. Thus, the quadratic terms in the local expansion of the temperature field have a negative contribution that grows as $-T_{\mathrm{peak}}(\varpi/\theta_{\mathrm{s}}^{\mathrm{2D}})^2$. At $\varpi \gtrsim \theta_{\mathrm{s}}^{\mathrm{2D}}$ the quadratic terms dominate and the $T$-$(-\nabla^2 T)$ correlation becomes negative. Meanwhile, the $T$-$(-\nabla^2 T)$ correlation tends to zero on the scale $\varpi \gtrsim \theta_{\mathrm{s}}^{\mathrm{2D}}$, where the temperature autocorrelation becomes weak and the local quadratic expansion starts to fail. As shown in Fig. 42, the dark ring appears at the critical point where the $T$-$(-\nabla^2 T)$ correlation reaches its minimum and turns back toward zero.

We have discussed the projection effects that make the projected radial acoustic scale on a stacked $T$ image larger than $\theta_{\mathrm{s}}$. For $Q_{\mathrm{r}}$, the most striking patterns in the image have

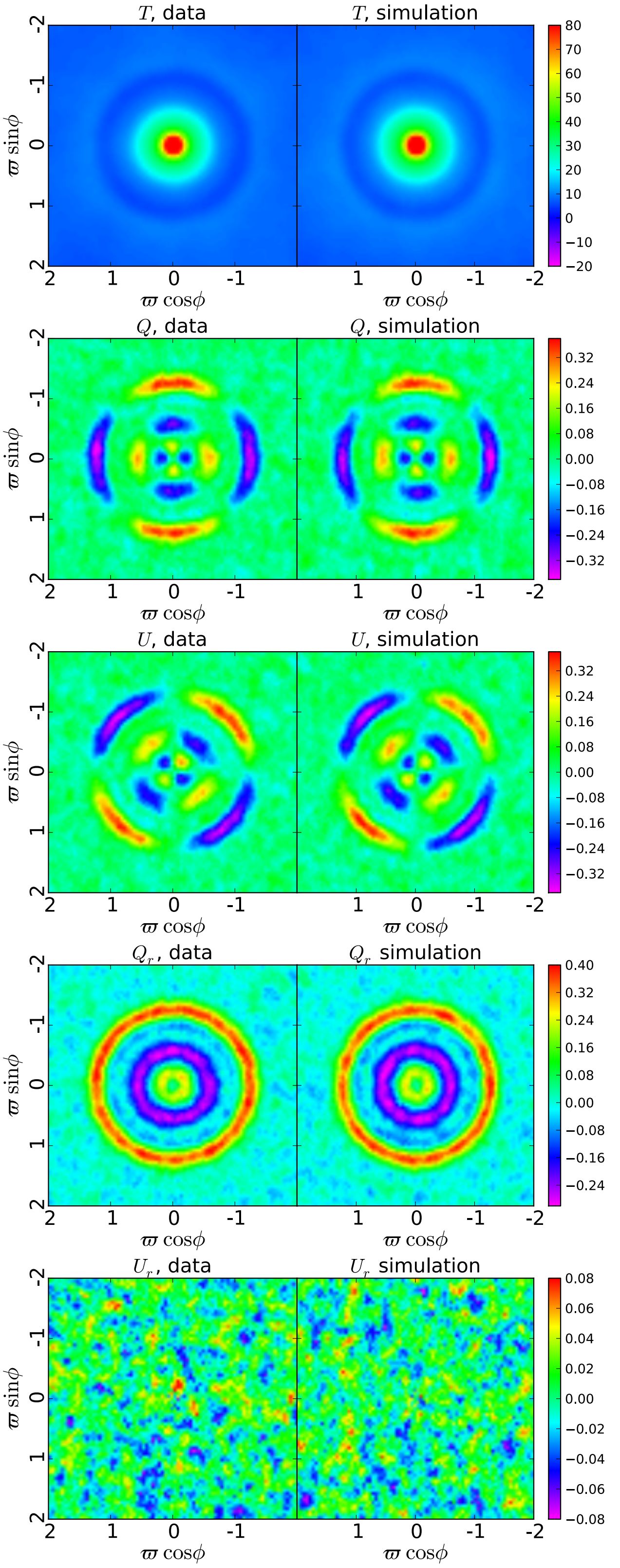

**Fig. 41.** From *top to bottom*, $T$, $Q$, $U$, $Q_r$, and $U_r$ stacked images (in $\mu$K units) extracted around temperature hot spots selected above the null threshold ($\nu = 0$) in the `Commander` sky map for data (*left column*) and an equivalent simulation (*right column*). The horizontal and vertical axes of the flat-sky projection are labelled in degrees.

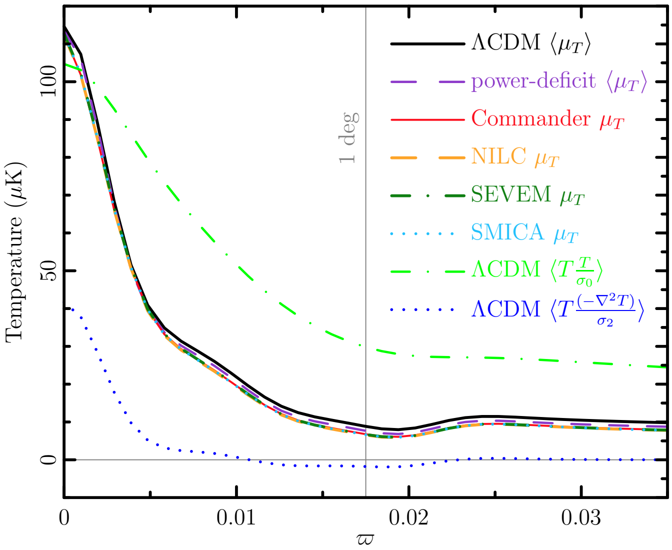

**Fig. 42.** Radial profile $\mu_T(\varpi)$ derived from the stacked temperature image (see Fig. 41 or 45). The denominators $\sigma_0$ and $\sigma_2$ are the theoretical rms values of CMB $T$ and $\nabla^2 T$, respectively. The theoretical $\langle\mu_T(\varpi)\rangle$ is a linear combination of $\langle T(\varpi)(T(0)/\sigma_0)\rangle$ (green dash-dotted line) and $\langle T(\varpi)(-\nabla^2 T(0))/\sigma_2)\rangle$ (blue dotted line). For all four component-separated maps, the deviation of $\mu_T$ from the ensemble mean $\langle\mu_T\rangle$ of the fiducial model (here the *Planck* 2015 ΛCDM best fit) is consistent with cosmic variance, and can be related to the low-$\ell$ power deficit. The example power-deficit $\langle\mu_T\rangle$ (purple dashed line) is the theoretical prediction of $\langle\mu_T\rangle$ if the fiducial model $C_\ell$s are reduced by 10% in the range $2 \le \ell \le 50$.

more intuitive simple explanations, since the stacking is essentially the real-space equivalent of the temperature polarization correlation. The projection function contains an extra $\ell^2$ factor, which enhances the high-$\ell$ power and reduces the projected radial acoustic scale, coincidentally, back to $\approx\theta_s$. The quadrupole responsible for the polarization around peaks is induced by gravity on angular scales larger than twice the size of the horizon at decoupling. In the case of an overdensity, this causes a flow of photons towards the gravitational well on these scales, inducing a quadrupolar pattern (see, e.g., Coulson et al. 1994). The spherical symmetry of the gravitational interaction causes a rotation of the quadrupole in the vicinity of the well, resulting in a radial configuration in polarization. This radial polarization pattern implies $Q_r > 0$ and an overdensity implies $T < 0$ by the Sachs-Wolfe formulae, which leads to anticorrelation on these scales. Similarily, an underdensity leads to an outward flow and induces a tangential polarization pattern, once again leading to anticorrelation on these scales. At smaller scales, the polarized contribution is dominated by the dynamics of the photon fluid. The acoustic oscillations modulate the polarization pattern, leading to the different rings in the stacked images. The most noticeable rings in the stacked $Q_r$ image are approximately at $\theta_s$ and $2\theta_s$. Thanks to the $\ell^2$ enhancement, multiple acoustic peaks in the $TE$ power spectrum may be captured and projected into ring patterns in the stacked polarization images. As photons flow towards the overdensity, they are compressed and the temperature increases, slowing the fluid descent into the well. Eventually, the radiation pressure becomes large enough to reverse the photon flow. This expansion cools the photons until they fall back towards the well. Note that the resulting inner ring was not observed in the WMAP analysis (Komatsu et al. 2011), since the resolution was too low.

Figure 41 clearly reveals all of the features described above. The two bright rings at $\theta_s \approx 0.011$ (0.6°) and $2\theta_s \approx 0.021$ (1.2°) are the predicted patterns associated with the first $C_\ell^{TE}$ acoustic

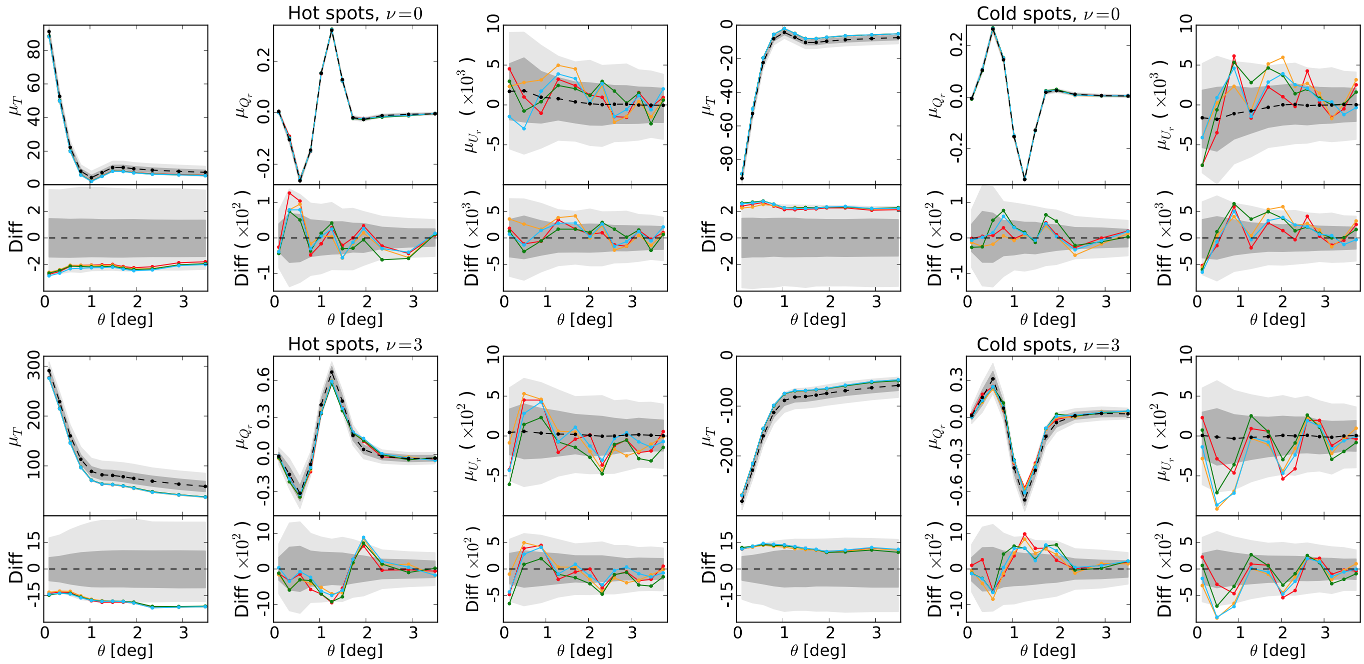

**Fig. 43.** Mean radial profiles of $T$, $Q_{\rm r}$, and $U_{\rm r}$ in $\mu$K obtained for `Commander` (red), `NILC` (orange), `SEVEM` (green), and `SMICA` (blue). Each individual panel contains (*top*) the mean radial profiles and (*bottom*) the differences (denoted "Diff") between the mean profiles of the data and those computed from the ensemble mean of the simulations. Results based on stacks around temperature hot and cold spots are shown in the *left and right columns*, respectively. *Upper plots* present results for peaks selected above the null threshold, while *lower plots* show the equivalent results for peak amplitudes above (hot spots) or below (cold spots) 3 times the dispersion of the temperature map. The black dots (connected by dashed lines) depict the mean profiles and the shaded regions correspond to the $1\sigma$ (68%) and $2\sigma$ (95%) error bars. The mean profiles and error bars are determined from `SEVEM` simulations. Note that the Diff curves for each component-separation method are computed using the corresponding ensemble average, although only the ensemble average from `SEVEM` is shown here.

peak at $\ell \approx 310$, while the two faint rings are a striking illustration of the detection of multiple acoustic peaks in the $TE$ power spectrum. The large-scale anticorrelation is suppressed due to the scale-dependent bias which results from the fact that peaks are defined by the second derivatives of the temperature field (e.g., Desjacques 2008).

We are now in a position to discuss the consistency of the *Planck* results with the predictions of a $\Lambda$CDM cosmology. For simplicity, further analysis is focused on the angular profiles, and specifically the mean, $\mu(\theta)$, estimated as the average of the angular profiles around all hot (cold) peaks above (below) a certain threshold $\nu$. This analysis is performed directly on the sphere to avoid any repixelization error. Note that the expected value of the mean temperature angular profile is proportional to $\int \ell \, {\rm d}\ell \, C_\ell^{TT} J_0(\ell\theta)$, whilst the expected values of the $Q_{\rm r}$ and $U_{\rm r}$ mean angular profiles are approximately proportional to $\int -\ell \, {\rm d}\ell \, C_\ell^{TE} J_2(\ell\theta)$ and $\int -\ell \, {\rm d}\ell \, C_\ell^{TB} J_2(\ell\theta)$, respectively. Since $T$ has even parity and $B$ has odd parity, the expectation value for $C_\ell^{TB}$ is zero, and the $U_{\rm r}$ mean angular profile is therefore expected to vanish.

A $\chi^2$ estimator is used to quantify the differences between the profiles obtained from the data and the expected values estimated with simulations:

$$\chi^2 = [\mu(\theta) - \bar{\mu}(\theta)] \, \mathbf{C}^{-1} \, [\mu(\theta) - \bar{\mu}(\theta)]^{\rm T} \, , \tag{70}$$

with the covariance matrix defined as

$$C(i,j) = \frac{1}{N-1} \sum_{k=1}^{N} [\mu_k(\theta_i) - \bar{\mu}(\theta_i)] \left[\mu_k(\theta_j) - \bar{\mu}(\theta_j)\right], \tag{71}$$

where the sum is over the $N$ simulations used to estimate this matrix and $\bar{\mu}(\theta)$ is the ensemble average. Note that although the profiles in Fig. 41 are derived from data at a resolution $N_{\rm side} = 1024$, faster convergence of the $\chi^2$ statistic is achieved using maps at a lower resolution. We have verified that the results remain unchanged when adopting data with $N_{\rm side} = 512$.

Figure 43 presents a comparison between the profiles obtained from the component-separated data and the mean value estimated from simulations processed through the `SEVEM` pipeline. Note that the error bars for the temperature profiles are asymmetric due to a bias in the selection of the peaks above a given threshold. Results for hot and cold spots are shown for two different thresholds, $\nu = 0$ and $\nu = 3$. There is generally excellent agreement between the different component-separation methods. A systematic deviation between the data and the simulations for the hot peaks in temperature ($\nu = 0$) is seen at a level greater than $1\sigma$. This discrepancy increases at higher thresholds, reaching values of about $2\sigma$ for the $\nu = 3$ case. Similar behaviour is seen for the cold spots. For the $Q_{\rm r}$ angular profiles, the most striking differences appear around $\theta = 2^\circ$ in the $\nu = 3$ case for hot peaks, and around $\theta = 1\overset{\circ}{.}5$ for the cold peaks. For the $U_{\rm r}$ angular profiles, where a null signal is expected (i.e., only noise is expected to be present), deviations at similar levels are seen.

Table 38 presents the corresponding $p$-values for this comparison. A theoretical $\chi^2$ distribution is used to determine the probability that a sky drawn from the $\Lambda$CDM cosmology has a value larger than that derived from the data. We have verified this approach by comparing the empirical $\chi^2$ distribution estimated from 100 simulations (in which the mean value and the covariance matrix are computed from a further 900 simulations) with the theoretical distribution with the corresponding degrees of freedom (see Fig. 44). The $\chi^2$ value of the data is then estimated using the mean value and the covariance matrix determined from simulations. Although some differences are found among the

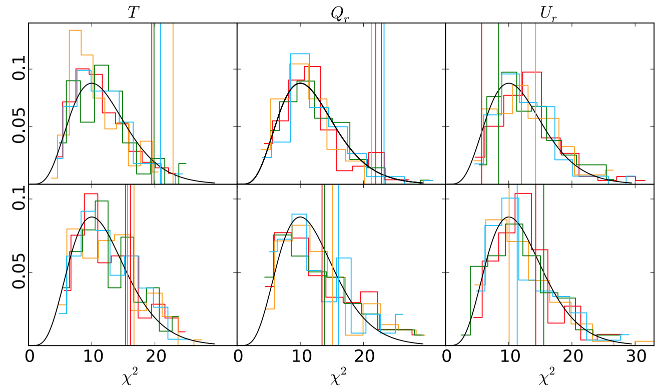

**Fig. 44.** $\chi^2$ distributions obtained from the $T$ (*left column*), $Q_r$ (*middle column*), and $U_r$ (*right column*) mean radial profiles centred on temperature hot spots selected above the null threshold (*upper row*) and three times the dispersion of the map (*bottom row*). The black lines correspond to the theoretical $\chi^2$ distribution with 12 degrees of freedom, whilst the histograms show the distributions determined from 100 simulations computed through the `Commander` (red), `NILC` (orange), `SEVEM` (green), and `SMICA` (blue) pipelines. The vertical lines represent the $\chi^2$ values obtained from the data.

**Table 38.** $p$-values of the $T$, $Q_r$, and $U_r$ angular profiles computed from the stacking of hot and cold spots selected above the $\nu = 0$ and $\nu = 3$ thresholds.

| | Probability [%] | | | |
|---|---|---|---|---|
| | `Comm.` | `NILC` | `SEVEM` | `SMICA` |
| | $\nu = 0$ (hot spots) | | | |
| $T$ . . . . . . . . . . . . | 8 | 3 | 7 | 5 |
| $Q_r$ . . . . . . . . . . . | 4 | 5 | 3 | 3 |
| $U_r$ . . . . . . . . . . . | 93 | 28 | 75 | 44 |
| | $\nu = 3$ (hot spots) | | | |
| $T$ . . . . . . . . . . . . | 18 | 16 | 22 | 21 |
| $Q_r$ . . . . . . . . . . . | 34 | 23 | 31 | 19 |
| $U_r$ . . . . . . . . . . . | 28 | 61 | 21 | 50 |
| | $\nu = 0$ (cold spots) | | | |
| $T$ . . . . . . . . . . . . | 23 | 38 | 29 | 39 |
| $Q_r$ . . . . . . . . . . . | 86 | 85 | 63 | 78 |
| $U_r$ . . . . . . . . . . . | 14 | 11 | 39 | 34 |
| | $\nu = 3$ (cold spots) | | | |
| $T$ . . . . . . . . . . . . | 24 | 21 | 23 | 20 |
| $Q_r$ . . . . . . . . . . . | 21 | 51 | 29 | 52 |
| $U_r$ . . . . . . . . . . . | 30 | 13 | 30 | 8 |

component-separation methods, a general consistency between model and data is found.

Although the $\chi^2$ test has the advantage of being sensitive to different types of deviations between model and data, does not assume prior knowledge about possible departures from the model, and can account for correlations between the various tests from which it is constructed, it can nevertheless be suboptimal under certain conditions. This appears to be the case when considering the systematic shift between data and simulations seen in the temperature profiles $\mu_T$ – the $\chi^2$ statistic is not particularly sensitive to systematic deviations of constant sign. We therefore consider an alternative quantity, the integrated profile deviation, defined as

$$\Delta\mu_T(W) = \int_0^R \left[\mu_T(\theta) - \bar{\mu}_T(\theta)\right] W(\theta)\,\mathrm{d}\theta, \tag{72}$$

**Table 39.** $p$-values of $\Delta\mu_T$ computed from the stacking of hot and cold spots selected above the $\nu = 0$ and $\nu = 3$ thresholds from the `Commander`, `NILC`, `SEVEM`, and `SMICA` maps.

| | Probability [%] | | | |
|---|---|---|---|---|
| | `Comm.` | `NILC` | `SEVEM` | `SMICA` |
| | Hot spots | | | |
| $T$ ($\nu = 0$) . . . . . . | 96.0 | 95.8 | 96.2 | 97.1 |
| $T$ ($\nu = 3$) . . . . . . | 98.6 | 98.2 | 98.3 | 98.7 |
| | Cold spots | | | |
| $T$ ($\nu = 0$) . . . . . . | 97.1 | 96.9 | 98.1 | 97.9 |
| $T$ ($\nu = 3$) . . . . . . | 92.0 | 90.6 | 90.6 | 93.0 |

where $R$, the size of stacking patches, is taken to be $3\overset{\circ}{.}5$ in this case. The weighting function is chosen to be proportional to the expected profile, but the results are robust for other choices, e.g., $W = 1$. The $p$-values obtained in this case are given in Table 39. These are consistent with what might be expected from visual inspection of the plots, i.e., the deviations are typically close to $2\sigma$. These deviations are likely to be connected to the deficit in the observed power spectrum at low multipoles, as may be seen in Fig. 42. Here, the purple dashed line indicates the reduction in $\bar{\mu}_T$ if the theoretical $C_\ell$ values are reduced by 10% over the range $2 \leq \ell \leq 50$.

### *8.2. Generalized stacking*

In this section, a much wider class of stacking methods is introduced, with particular emphasis on *oriented stacking*, a novel approach that has not previoulsy been explored in the literature. We regard the stacking as *oriented* if the orientation of the local coordinate frame, and in particular the $\phi = 0$ axis, is correlated with the map that is being stacked. Thus, the stacking methodology in Sect. 8.1 is considered unoriented, because the orientation is defined relative to the local meridian pointing towards the Galactic south, rather than any property of the data themselves. Alternative approaches to unoriented stacking can also be considered. In this subsection, the orientation of each patch is chosen randomly from a uniform distribution in $[0, 2\pi)$. The unoriented $T$ and $Q_r$ images can then be directly compared with previous sections.

For unoriented stacking, the ensemble average of stacked fields cannot result in any intrinsic $\phi$-dependence, as this would be averaged out by the uncorrelated orientation choices. The $\phi$-dependence due to a specific choice of representation can always be removed via a local rotation. For example, the ensemble averages of $Q + \mathrm{i}U$ around unoriented temperature peaks are proportional to $\mathrm{e}^{2\mathrm{i}\phi}$. A local rotation $(Q, U) \to (Q_r, U_r)$ (Kamionkowski et al. 1997) removes the $\mathrm{e}^{2i\phi}$ factor and compresses the information into a single real map $Q_r$. For oriented stacking, the $\phi$-dependence can be a mixture of a few Fourier modes ($\mathrm{e}^{\mathrm{i}m\phi}$, for integer $m$). Each $m$ mode corresponds to a radial ($\varpi$-dependent) function.

In what follows, we use the $N_{\mathrm{side}} = 1024$ component-separated maps at a resolution of $10'$ FWHM. The use of this higher resolution as compared to the $N_{\mathrm{side}} = 512$ data used in Sect. 8.1 is motivated by the smaller-scale features that are expected to result from the oriented stacking.

We also introduce the concept of the noise-free ensemble average (NFEA), which is defined as the ensemble average of stacked CMB-only maps for a fiducial cosmology. Recall that the fiducial model for the simulated sky maps, the *Planck* 2013 best-fit ΛCDM model (Planck Collaboration XVI 2014), differs from the updated *Planck* 2015 best-fit ΛCDM model (Planck Collaboration XIII 2016). In previous sections, this mismatch was partially accommodated by rescaling the CMB signal by a fixed scale factor. Here, we instead specifically adopt the 2015 best fit as a fiducial model for the data. When comparing the data to the simulations, we subtract the corresponding NFEA to minimize any bias resulting from cosmology dependence.

In the context of random Gaussian fields, the NFEA can be computed straightforwardly following Bardeen et al. (1986):

$$\langle M\rangle = \left\langle M\boldsymbol{w}^{\mathsf{T}}\right\rangle\left\langle \boldsymbol{w}\boldsymbol{w}^{\mathsf{T}}\right\rangle^{-1}\langle\boldsymbol{w}\rangle, \tag{73}$$

where $M$ is the map (around the central peak) to be stacked, and $\boldsymbol{w}$ is the collection of Gaussian variables (on the central peak) that are related to peak selection and orientation determination. Equation (73) is only valid for Gaussian random variables. If the patch is rotated before stacking, the field value evaluated at a dynamic coordinate is, in general, not a random Gaussian variable. However, statistical isotropy guarantees that the rotation of patches is equivalent to an orientation constraint on the nonzero-spin field. For example, orienting each patch in the direction where $U = 0$ and $Q > 0$ is equivalent to the unoriented stacking case where only peaks satisfying the additional constraint $-\epsilon/2 < \arg(Q + \mathrm{i}U) < \epsilon/2$ ($\epsilon \to 0^+$) are selected.

A further source of statistical bias can arise from noise mismatch between the simulations and the data. Since the effect of noise is to introduce random shifts in the peaks and hence suppress patterns in the stacked images, any noise mismatch can lead to pattern mismatch between the data and simulations. For the temperature data, the contribution due to noise mismatch is estimated to be at the sub-percent level, lower than the cosmic variance. For stacking on polarization peaks, the impact of the noise mismatch cannot be safely ignored. Thus, for quantitative comparisons in this paper, we only consider stacking on temperature peaks.

### 8.2.1. Oriented temperature stacking

The most straightforward way to orient a patch centred on a temperature peak is to align the horizontal axis with the major axis defined by a local quadratic expansion of the temperature field around the peak. The disadvantage of doing so is that the orientation is dominated by small-scale fluctuations that are noise-sensitive. A better choice is to use the major axis of the inverse Laplacian $\nabla^{-2}T$ that filters out the small-scale power. The inverse Laplacian is defined as:

$$\nabla^{-2}T\left(\hat{\boldsymbol{n}}\right) = -\sum_{\ell=2}^{\infty}\sum_{m=-\ell}^{\ell}\frac{a_{\ell m}^{T}}{\ell(\ell+1)}Y_{\ell m}\left(\hat{\boldsymbol{n}}\right), \tag{74}$$

where $a_{\ell m}^{T}$ are the harmonic coefficients of the masked temperature map. Spin-2 maps $Q_T$, $U_T$ are then defined by:

$$\left(Q_T \pm \mathrm{i}U_T\right)\left(\hat{\boldsymbol{n}}\right) = \sum_{\ell=2}^{\infty}\sum_{m=-\ell}^{\ell} a_{\ell m}^{T}\left[\,{}_{\pm 2}Y_{\ell m}(\hat{\boldsymbol{n}})\right]. \tag{75}$$

In the flat-sky limit, $Q_T \approx (\partial_x^2 - \partial_y^2)(\nabla^{-2}T)$ and $U_T \approx -2\partial_x\partial_y\nabla^{-2}T$. To align the $\nabla^{-2}T$ axes of the patches, we rotate each patch so that $U_T$ vanishes and $Q_T \geq 0$ for the central peak.

Figure 45 presents the stacked images of `SMICA` temperature patches centred on temperature hot spots selected above the threshold $\nu = 0$, in both unoriented and oriented forms. These are seen to be in excellent agreement with their accompanying NFEAs, and, in the case of the unoriented stacks, with the results shown in Fig. 41, despite the different stacking methodologies adopted (and component separation method selected for visualization purposes).

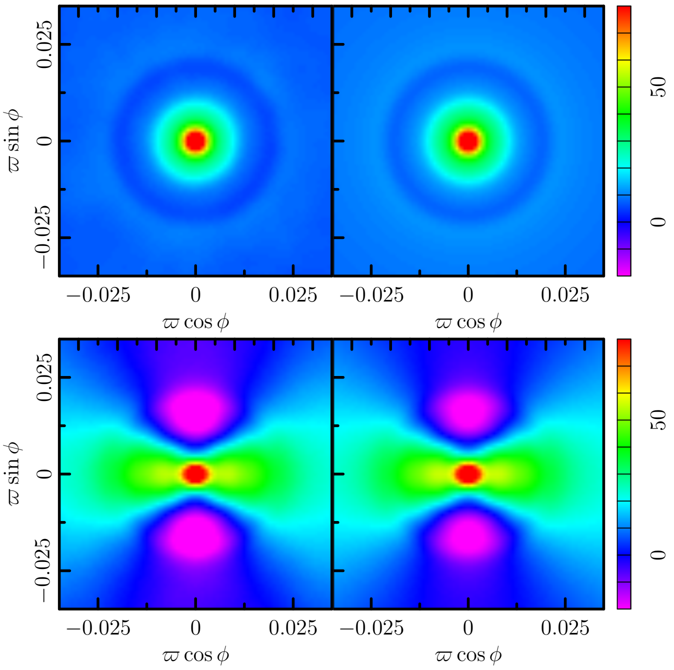

**Fig. 45.** Comparison between unoriented stacking (*upper panels*) and oriented stacking (*lower panels*) of temperature patches around temperature hot spots selected above the null threshold ($\nu = 0$). The *left panels* are the stacked `SMICA` maps, and the *right panels* their corresponding NFEAs. The image units are $\mu$K.

The oriented $T$ image is notably different from the unoriented one. The alignment between the major axis (of $\nabla^{-2}T$) and the horizontal axis results in an ellipse elongated along the horizontal axis, rather than a central disc. Moreover, the quadratic-term contribution is suppressed along the horizontal axis where the temperature profile is smoother, and enhanced along the vertical axis where the temperature profile is sharper. As a consequence, the dark ring visible in the upper panel at 1° splits into two cold blobs along the vertical axis.

To proceed with a quantitative analysis, we extract Fourier modes $T_m(\varpi)$ from the stacked map $T_{\mathrm{stack}}(\varpi, \phi)$ as follows:

$$T_m(\varpi) = \frac{1}{(1+\delta_{m0})\pi}\int_0^{2\pi} T_{\mathrm{stack}}\left(\varpi, \phi\right)\cos m\phi\,\mathrm{d}\phi, \tag{76}$$

where $\delta_{m0}$ is the Kronecker delta function. For odd $m$, the NFEA $\langle T_m\rangle$ vanishes due to statistical isotropy. For even $m$, a straightforward calculation shows that only $T_0(\varpi)$, which is equivalent to $\mu_T(\varpi)$, and $T_2(\varpi)$ have nonzero NFEAs.

As discussed previously in Sect. 8.1, there are some shortcomings of the standard $\chi^2$ procedure that is generally used to assess the consistency of the data with simulations. The problem is simplified by studying the statistics of an integrated profile deviation:

$$\mathcal{T}_m(W) = \int_0^R \left[T_m(\varpi) - \langle T_m(\varpi)\rangle\right] W(\varpi)\,\mathrm{d}\varpi, \tag{77}$$

where $R$, the size of the stacking patches, is taken to be 2° in our examples. The purpose of removing the NFEA, $\langle T_m(\varpi)\rangle$, which

**Table 40.** $\mathcal{T}_m$, as defined in Eqs. (77) and (78), for different thresholds $\nu$.

| | $\mathcal{T}_0$ | | $\mathcal{T}_2$ | |
|---|---|---|---|---|
| Method | Hot spots | Cold spots | Hot spots | Cold spots |
| | | Threshold $\nu = 0$ | | |
| `Commander` .... | $-0.03(\ 0.04^{+0.06+0.15}_{-0.04-0.07})$ | $-0.04(\ 0.04^{+0.06+0.16}_{-0.04-0.07})$ | $0.07(0.04^{+0.01+0.03}_{-0.02-0.04})$ | $0.06(0.04^{+0.01+0.03}_{-0.02-0.04})$ |
| `NILC` ......... | $-0.04(\ 0.04^{+0.06+0.15}_{-0.04-0.07})$ | $-0.05(\ 0.04^{+0.06+0.16}_{-0.04-0.07})$ | $0.06(0.03^{+0.01+0.02}_{-0.02-0.04})$ | $0.05(0.03^{+0.01+0.03}_{-0.02-0.04})$ |
| `SEVEM` ........ | $-0.03(\ 0.04^{+0.06+0.15}_{-0.04-0.07})$ | $-0.04(\ 0.04^{+0.06+0.16}_{-0.04-0.07})$ | $0.06(0.04^{+0.01+0.03}_{-0.02-0.04})$ | $0.06(0.04^{+0.01+0.03}_{-0.02-0.04})$ |
| `SMICA` ........ | $-0.03(-0.01^{+0.03+0.07}_{-0.02-0.04})$ | $-0.05(\ 0.00^{+0.03+0.07}_{-0.02-0.04})$ | $0.06(0.04^{+0.01+0.03}_{-0.02-0.04})$ | $0.06(0.04^{+0.01+0.03}_{-0.02-0.04})$ |
| | | Threshold $\nu = 1$ | | |
| `Commander` .... | $-0.06(\ 0.05^{+0.09+0.22}_{-0.05-0.10})$ | $-0.06(\ 0.05^{+0.09+0.21}_{-0.06-0.09})$ | $0.06(0.03^{+0.02+0.03}_{-0.02-0.04})$ | $0.04(0.03^{+0.02+0.03}_{-0.02-0.04})$ |
| `NILC` ......... | $-0.06(\ 0.05^{+0.09+0.22}_{-0.05-0.10})$ | $-0.07(\ 0.05^{+0.09+0.21}_{-0.05-0.09})$ | $0.06(0.02^{+0.02+0.03}_{-0.02-0.04})$ | $0.04(0.02^{+0.02+0.03}_{-0.02-0.04})$ |
| `SEVEM` ........ | $-0.06(\ 0.06^{+0.09+0.22}_{-0.05-0.10})$ | $-0.06(\ 0.06^{+0.09+0.22}_{-0.05-0.10})$ | $0.06(0.03^{+0.02+0.03}_{-0.02-0.04})$ | $0.04(0.03^{+0.02+0.03}_{-0.02-0.04})$ |
| `SMICA` ........ | $-0.06(-0.01^{+0.04+0.10}_{-0.03-0.06})$ | $-0.07(-0.01^{+0.04+0.10}_{-0.03-0.06})$ | $0.06(0.03^{+0.02+0.03}_{-0.02-0.04})$ | $0.04(0.03^{+0.02+0.03}_{-0.02-0.04})$ |

**Notes.** The expected values, together with the $1\sigma$ (68% CL) and $2\sigma$ (95% CL) ranges, determined from simulations are given in brackets.

**Table 41.** $\mathcal{T}_0$, as defined in Eqs. (77) and (78), for different thresholds $\nu$ and hemispheres.

| | "North" $\mathcal{T}_0$ | | "South" $\mathcal{T}_0$ | |
|---|---|---|---|---|
| Method | Hot spots | Cold spots | Hot spots | Cold spots |
| | | Threshold $\nu = 0$ | | |
| `Commander` ..... | $-0.02(\ 0.03^{+0.07+0.16}_{-0.04-0.07})$ | $-0.03(\ 0.03^{+0.07+0.18}_{-0.04-0.07})$ | $-0.05(\ 0.03^{+0.07+0.18}_{-0.05-0.07})$ | $-0.06(\ 0.03^{+0.07+0.18}_{-0.04-0.07})$ |
| `NILC` ......... | $-0.02(\ 0.02^{+0.07+0.16}_{-0.04-0.07})$ | $-0.03(\ 0.02^{+0.07+0.17}_{-0.04-0.07})$ | $-0.05(\ 0.02^{+0.07+0.18}_{-0.04-0.07})$ | $-0.06(\ 0.02^{+0.07+0.18}_{-0.04-0.07})$ |
| `SEVEM` ........ | $-0.02(\ 0.03^{+0.07+0.17}_{-0.04-0.07})$ | $-0.03(\ 0.03^{+0.07+0.18}_{-0.04-0.07})$ | $-0.05(\ 0.03^{+0.07+0.18}_{-0.05-0.07})$ | $-0.06(\ 0.03^{+0.07+0.18}_{-0.04-0.07})$ |
| `SMICA` ........ | $-0.02(-0.01^{+0.04+0.09}_{-0.03-0.05})$ | $-0.03(-0.01^{+0.04+0.09}_{-0.03-0.05})$ | $-0.05(-0.01^{+0.04+0.08}_{-0.03-0.05})$ | $-0.07(-0.01^{+0.04+0.08}_{-0.03-0.05})$ |
| | | Threshold $\nu = 1$ | | |
| `Commander` .... | $-0.04(\ 0.03^{+0.09+0.22}_{-0.06-0.10})$ | $-0.05(\ 0.03^{+0.09+0.23}_{-0.06-0.10})$ | $-0.08(\ 0.04^{+0.09+0.25}_{-0.06-0.11})$ | $-0.08(\ 0.04^{+0.09+0.24}_{-0.06-0.10})$ |
| `NILC` ......... | $-0.05(\ 0.03^{+0.10+0.23}_{-0.06-0.10})$ | $-0.06(\ 0.02^{+0.09+0.23}_{-0.06-0.10})$ | $-0.08(\ 0.03^{+0.09+0.25}_{-0.06-0.11})$ | $-0.08(\ 0.03^{+0.09+0.23}_{-0.06-0.10})$ |
| `SEVEM` ........ | $-0.04(\ 0.04^{+0.10+0.23}_{-0.06-0.10})$ | $-0.05(\ 0.03^{+0.10+0.23}_{-0.06-0.10})$ | $-0.08(\ 0.04^{+0.09+0.25}_{-0.07-0.11})$ | $-0.08(\ 0.04^{+0.09+0.24}_{-0.06-0.11})$ |
| `SMICA` ........ | $-0.04(-0.02^{+0.05+0.13}_{-0.04-0.07})$ | $-0.05(-0.02^{+0.05+0.13}_{-0.04-0.07})$ | $-0.08(-0.02^{+0.05+0.11}_{-0.04-0.07})$ | $-0.09(-0.02^{+0.05+0.12}_{-0.04-0.07})$ |

**Notes.** The "north" hemisphere is centred on the Galactic coordinate $(l, b) = (212^\circ, -13^\circ)$ and the "south" hemisphere in the opposite direction. The expected values, together with the $1\sigma$ (68% CL) and $2\sigma$ (95% CL) ranges, determined from simulations are given in brackets.

differs for the data and the simulations, is to minimize the impact of the cosmology dependence. A natural choice for the filter is $\langle T_m(\varpi)\rangle$ itself with a proper normalization:

$$W(\varpi) = \frac{\langle T_m(\varpi)\rangle}{\int_0^R \langle T_m(\varpi)\rangle^2 \mathrm{d}\varpi}\cdot \tag{78}$$

For the filter given by Eq. (78), the integrated profile deviation $\mathcal{T}_m$ describes the relative deviation from the NFEA. If ΛCDM is the correct model, the deviation is due to cosmic variance and noise. The distribution of $\mathcal{T}_m$ is obtained from simulations.

Table 40 presents a comparison of the $\mathcal{T}_m$ values derived from the *Planck* data and the FFP8 simulations. No inconsistencies in excess of the $3\sigma$ level have been found, although tensions around $2\sigma$ are seen.

The $m = 0$ projection kernel $J_0[(\ell + 1/2)\varpi]$ peaks at low $\ell$. Thus $\mathcal{T}_0$ is cosmic-variance sensitive and the apparent discrepancy in it could be related to a low-$\ell$ power deficit. An example is shown in Fig. 42 for illustration. To test the robustness of this result, we have tried three additional filters: a top-hat filter $W = 1$, a linear filter $W = \varpi$, and a Gaussian filter $W = \exp(-\varpi^2/\sigma_\mathrm{g}^2)$ with $\sigma_\mathrm{g} = 1^\circ$. In all cases, the power deficit remains at about the $2\sigma$ level.

Although the $\mathcal{T}_0$ deficit is not significant enough to falsify the ΛCDM model, further investigation of its properties may still be interesting and help us understand the other anomalies discussed in this paper. We consider two possibilities. Firstly the amplitude of the $\mathcal{T}_0$ deficit is of order 5–10%, which coincides with the level of hemispherical power asymmetry discussed in Sect. 6.1. To test whether the $\mathcal{T}_0$ deficit is localized on one hemisphere, we define the "north" direction to be aligned with the power asymmetry direction at $(l, b) = (212^\circ, -13^\circ)$ (Akrami et al. 2014) and compute $\mathcal{T}_0$ on the northern and southern hemispheres separately. The results are presented in Table 41. Although the $\mathcal{T}_0$ deficit is more significant for the southern hemisphere, it remains consistent with the ΛCDM prediction. Secondly, it is of interest to determine whether the $\mathcal{T}_0$ deficit is related to the Cold Spot discussed in Sect. 5.7. We therefore mask out the Cold Spot using a disc of radius 6° and repeat the calculation. The impact of this region on the $\mathcal{T}_0$ deficit is insignificant.

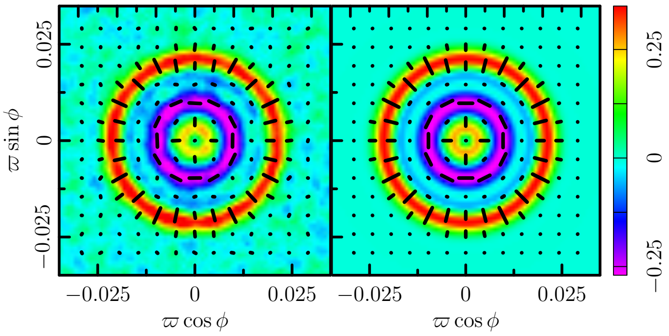

**Fig. 46.** Stacked $Q_{\rm r}$ image around temperature hot spots selected above the null threshold ($\nu = 0$) in the `SMICA` sky map. The *left panel* corresponds to the observed data and the *right panel* shows the NFEA. The image units are $\mu$K. The headless vectors (black solid lines) are the polarization directions for stacked $Q_{\rm stack}$, $U_{\rm stack}$. The lengths of the headless vectors are proportional to the polarization amplitude $P_{\rm stack}$.

Tensions at the $2\sigma$ level are also seen for $\mathcal{T}_2$. However, due to the additional $\ell^2$ factor in the projection kernel, the oriented ($m = 2$) component $\mathcal{T}_2$ is more sensitive to high-$\ell$ power where the cosmic variance is small, and an understanding of the noise properties of the data is more important. The former implies that the related uncertainty in $\mathcal{T}_2$ is, in general, smaller than that in $\mathcal{T}_0$. However, a mismatched cosmology, perhaps arising from a different primordial power amplitude $A_{\rm s}$, can then lead to significant tension between the data and the simulations. Indeed, we find that without application of our cosmology calibration (i.e., the subtraction of the NFEA in Eq. (77)) the $\mathcal{T}_2$-tension between the data and simulations increases by about $0.5\sigma$, whereas the variation of the $\mathcal{T}_0$-tension is $\lesssim 0.2\sigma$. The high-$\ell$ sensitivity of $\mathcal{T}_2$ also requires the use of an accurate noise model, and it is possible that the 1–$2\sigma$ tension in $\mathcal{T}_2$ may be alleviated once improved noise simulations are available.

### 8.2.2. Oriented polarization stacking

The stacked $Q$ and $U$ images can be decomposed into Fourier modes, $Q+{\rm i}U = \sum_{m=-\infty}^{\infty} P_m(\varpi){\rm e}^{im\phi}$. For unoriented $Q+{\rm i}U$ stacking on temperature peaks, only $P_2(\varpi)$ has a non-zero NFEA, and it can be linked to the conventional $Q_{\rm r}$ stacking via $P_2 = -Q_{\rm r}$. Figure 46 shows that the stacked $Q_{\rm r}$ image is in excellent agreement with its NFEA and the corresponding stacked image (fourth panel) in Fig. 41, despite the different stacking methodologies adopted (and component-separation method selected for visualization purposes). The length and orientation of the headless vectors represent the polarization amplitude, $P_{\rm stack} \equiv \sqrt{Q^2_{\rm stack} + U^2_{\rm stack}}$, and direction.

We next consider oriented stacking of the polarization maps, again using $Q_T$, $U_T$ to define the orientation of the patches. The stacked polarization images around temperature peaks have $m = 0, 2, 4$ Fourier components. We can also choose to stack the polarization maps on $P_T$ peaks, where $P_T = \sqrt{Q_T^2 + U_T^2}$. This picks up $m = 0, 4$ Fourier modes with no circularly symmetric ($Q_{\rm r}$, $m = 2$) mode. In Fig. 47 we compare the $(Q, U)$ images stacked centred either on $T$ peaks (top panel) or on $P_T$ peaks (bottom panel) with their corresponding NFEAs, and find excellent agreement.

For a quantitative comparison, we only consider stacking on temperature peaks and define the polarization integrated profile deviation

$$\mathcal{P}_m(W) = \int_0^R \left(P_m(\varpi) - \langle P_m(\varpi)\rangle\right) W(\varpi)\,{\rm d}\varpi, \tag{79}$$

where by default the filter is

$$W(\varpi) = \frac{\langle P_m(\varpi)\rangle}{\int_0^R \langle P_m(\varpi)\rangle^2 {\rm d}\varpi}\cdot \tag{80}$$

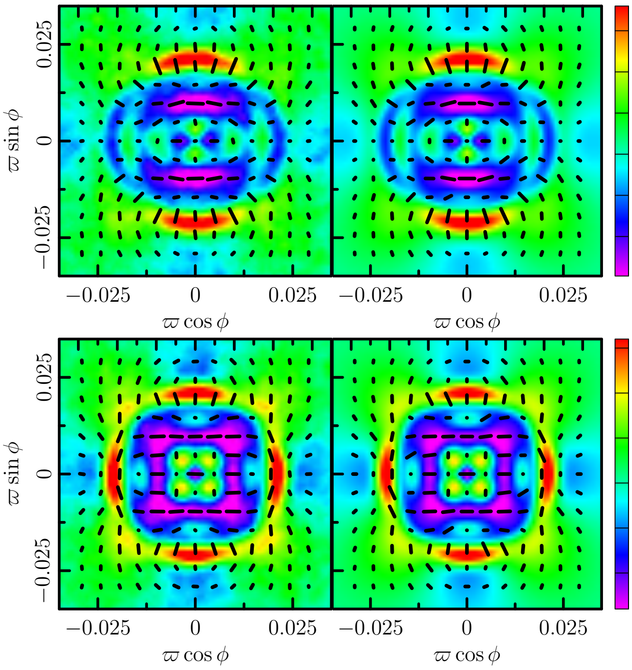

**Fig. 47.** Oriented stacking of polarization fields ($Q$, $U$) on temperature maxima (*upper panels*) and $P_T$ maxima (*lower panels*). In both cases the threshold $\nu = 0$ is used and the orientation is chosen such that $U_T = 0$ and $Q_T \geq 0$ on the central peak. The image units are $\mu$K. The *left panels* are the stacked `SMICA` maps, and the *right panels* their NFEAs. See Fig. 46 for the meaning of the headless vectors (black dashed lines).

The comparison of $\mathcal{P}_m$ ($m = 0, 2, 4$) between the data and the simulations is shown in Table 42, where the results are seen to be in excellent agreement.

Finally, we note that the peak selection does not have to be made from the temperature map. In Fig. 48 we show a few examples of stacking on polarization peaks using the $N_{\rm side} = 512$ maps. The higher-resolution polarization data are too noisy for peak selection. In the upper panels, we compare stacked images of the $E$-mode map centred around $E$-mode peaks with the corresponding NFEA. We find that the noise impact is relatively minor for 20′ FWHM maps and the plots are in qualitatively good agreement. Another possibility, shown in the lower panels, is to stack polarization maps centred on peaks determined from the corresponding polarization amplitude map. In this case the peaks are strongly biased by the quadratic noise contribution and quite visible deviation from the NFEA is observed in the stacked image.

## 9. Conclusions

In this paper, we have presented a study of the statistical isotropy and Gaussianity of the CMB using the *Planck* 2015 data, including the full mission for temperature. We do not claim that our results support or refute any particular physical model. Rather,

**Table 42.** $\mathcal{P}_m$, as defined in Eqs. (79) and (80), for different thresholds $\nu$.

| Method | $\mathcal{P}_0$ | $\mathcal{P}_2$ | $\mathcal{P}_4$ |
|---|---|---|---|
| Hot spots, threshold $\nu = 0$ | | | |
| `Commander` .... | $0.06(0.02^{+0.03+0.05}_{-0.03-0.06})$ | $-0.01(\ 0.01^{+0.01+0.02}_{-0.01-0.02})$ | $0.04(0.01^{+0.02+0.05}_{-0.02-0.05})$ |
| `NILC` ......... | $0.05(0.02^{+0.03+0.05}_{-0.03-0.06})$ | $-0.02(\ 0.00^{+0.01+0.02}_{-0.01-0.02})$ | $0.03(0.01^{+0.02+0.05}_{-0.02-0.05})$ |
| `SEVEM` ........ | $0.05(0.02^{+0.03+0.06}_{-0.03-0.06})$ | $0.01(\ 0.01^{+0.01+0.02}_{-0.01-0.02})$ | $0.04(0.01^{+0.02+0.05}_{-0.02-0.05})$ |
| `SMICA` ........ | $0.05(0.03^{+0.03+0.05}_{-0.03-0.05})$ | $-0.02(\ 0.00^{+0.01+0.02}_{-0.01-0.02})$ | $0.03(0.01^{+0.02+0.05}_{-0.02-0.05})$ |
| Cold spots, threshold $\nu = 0$ | | | |
| `Commander` .... | $0.06(0.02^{+0.03+0.05}_{-0.03-0.06})$ | $-0.01(\ 0.01^{+0.01+0.02}_{-0.01-0.02})$ | $0.03(0.01^{+0.03+0.05}_{-0.02-0.05})$ |
| `NILC` ......... | $0.06(0.02^{+0.03+0.05}_{-0.03-0.06})$ | $-0.01(\ 0.00^{+0.01+0.02}_{-0.01-0.02})$ | $0.04(0.01^{+0.02+0.04}_{-0.03-0.06})$ |
| `SEVEM` ........ | $0.06(0.03^{+0.03+0.05}_{-0.03-0.06})$ | $0.01(\ 0.01^{+0.01+0.02}_{-0.01-0.02})$ | $0.03(0.01^{+0.02+0.05}_{-0.03-0.05})$ |
| `SMICA` ........ | $0.05(0.03^{+0.03+0.05}_{-0.03-0.06})$ | $-0.02(\ 0.00^{+0.01+0.02}_{-0.01-0.02})$ | $0.03(0.02^{+0.02+0.04}_{-0.02-0.05})$ |
| Hot spots, threshold $\nu = 1$ | | | |
| `Commander` .... | $0.04(0.02^{+0.03+0.06}_{-0.04-0.07})$ | $-0.02(\ 0.00^{+0.02+0.03}_{-0.02-0.03})$ | $0.05(0.01^{+0.03+0.06}_{-0.03-0.06})$ |
| `NILC` ......... | $0.06(0.02^{+0.03+0.07}_{-0.04-0.07})$ | $-0.02(-0.01^{+0.01+0.03}_{-0.02-0.03})$ | $0.05(0.01^{+0.03+0.06}_{-0.03-0.06})$ |
| `SEVEM` ........ | $0.05(0.02^{+0.04+0.07}_{-0.04-0.07})$ | $-0.01(\ 0.00^{+0.02+0.03}_{-0.01-0.03})$ | $0.05(0.01^{+0.03+0.06}_{-0.03-0.06})$ |
| `SMICA` ........ | $0.04(0.03^{+0.03+0.07}_{-0.03-0.07})$ | $-0.02(\ 0.00^{+0.01+0.02}_{-0.01-0.03})$ | $0.06(0.01^{+0.03+0.05}_{-0.03-0.06})$ |
| Cold spots, threshold $\nu = 1$ | | | |
| `Commander` .... | $0.07(0.02^{+0.03+0.06}_{-0.03-0.07})$ | $0.00(-0.01^{+0.02+0.03}_{-0.02-0.03})$ | $0.01(0.01^{+0.03+0.06}_{-0.03-0.07})$ |
| `NILC` ......... | $0.08(0.02^{+0.03+0.06}_{-0.04-0.07})$ | $-0.01(-0.01^{+0.01+0.03}_{-0.02-0.03})$ | $0.01(0.01^{+0.03+0.06}_{-0.03-0.07})$ |
| `SEVEM` ........ | $0.09(0.02^{+0.03+0.07}_{-0.03-0.07})$ | $0.00(\ 0.00^{+0.02+0.03}_{-0.02-0.03})$ | $0.02(0.01^{+0.03+0.06}_{-0.03-0.06})$ |
| `SMICA` ........ | $0.06(0.03^{+0.03+0.06}_{-0.03-0.07})$ | $-0.01(\ 0.00^{+0.01+0.02}_{-0.01-0.03})$ | $0.02(0.01^{+0.03+0.06}_{-0.03-0.06})$ |

**Notes.** The expected values, together with $1\sigma$ (68% CL) and $2\sigma$ (95% CL) ranges, determined from simulations are given in brackets.

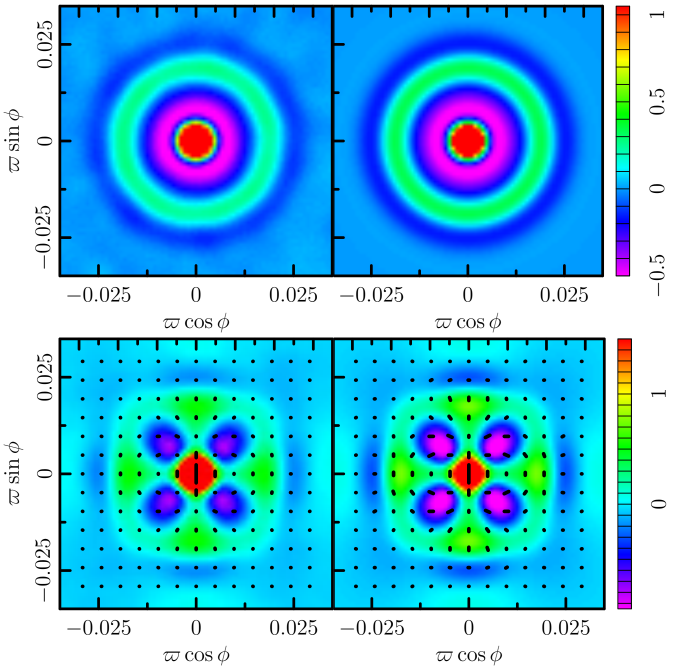

**Fig. 48.** *Top*: $E$-mode maps stacked on the unoriented $E$-mode maxima computed above the null threshold $\nu = 0$. *Bottom*: $Q$ stacked around oriented polarization amplitude ($P$) maxima. In this case, no threshold is used and the orientation is chosen such that $U = 0$ and $Q \geq 0$ on the central peak. The *left panels* are the stacked `SMICA` maps, and the *right panels* their corresponding NFEAs. See Fig. 46 for the meaning of the headless vectors (black dashed lines). The image units are $\mu$K.

we focus on null-hypothesis testing: a number of tests are performed, then $p$-values are calculated and reported. It is in the very nature of such a model-independent approach to leave the detailed interpretation to the reader. However, we do address the important subject of a posteriori correction where possible.

The statistical tests are performed on maps of the CMB anisotropy that result from the application of the four component-separation methods described in Planck Collaboration IX (2016). All of the results presented here are robust with respect to the choice of component-separated CMB map. This is important since it demonstrates the high quality and equivalence of the *Planck* component-separated data products rendered by different methodologies under varying assumptions.

We find that the CMB is largely consistent with statistical isotropy, although there are a few indications of anomalies with respect to the expectations of $\Lambda$CDM. Some of the tests we have performed are the same as those in PCIS13, in which case the results are consistent. Since many of these anomalies were also observed in the WMAP temperature data, we re-emphasize explicitly the statement we made in 2013 – that the agreement between the two independent experiments effectively rules out the possibility that the origin of these features can be found in residual systematic artefacts present in either data set. We have also performed a number of new tests, in order to try to narrow down the nature of the apparent violations of statistical isotropy. In addition, although the component-separated polarization maps contained in the *Planck* 2015 release are high-pass filtered, we have performed a stacking analysis that tests some aspects of the polarized sky while mitigating the impacts of noise and systematic effects.

In Sect. 4, we examined aspects of the Gaussianity of the CMB fluctuations. Tests of skewness, kurtosis, multi-normality, $N$-point functions, and Minkowski functionals yielded no indications of significant departures from Gaussianity, while the variance of the CMB map was found to be low, in agreement with previous studies (PCIS13). First-order moments of filtered maps also exhibit the low-variance anomaly, as well as a kurtosis excess on certain scales associated with the Cold Spot. A new study of peak statistics finds results consistent with the expectations for a Gaussian random field, although the Cold Spot is again detected.

Section 5 provides an updated study of several previously known peculiarities. We study in detail the low variance anomaly, which appears to be associated with the known low-$\ell$ deficit in the angular power spectrum. We confirm the lack of large-scale angular correlations, relatively featureless northern ecliptic hemisphere 3- and 4-point functions, and indications of violations of point- and mirror-parity symmetry, although we make little or no attempt to correct these for a posteriori effects. We place tight constraints on a quadrupolar power modulation. The Cold Spot is examined further, and, while we find variance, skewness, and kurtosis angular profiles consistent with the expectations of statistically isotropic simulations, the mean temperature profile is anomalous at roughly the 1% level, apparently due to the surrounding hot ring – the feature that deviates most from the Gaussian model.

In Sect. 6 we perform a series of tests probing the well-known large-scale dipolar power asymmetry. We detect the asymmetry via pixel-to-pixel variance, as well as by measuring power explicitly or indirectly via $\ell$ to $\ell \pm 1$ mode coupling. The latter approach lends itself to a posteriori correction, which reduces the significance of the asymmetry substantially when no model for the anomaly is assumed. In addition, we perform two independent but related tests of directionality. One finds suggestions of anomalous clustering of directions out to relatively small scales while the other does not, evidently due to being optimized for slightly different forms of directionality.

Section 7 demonstrates that the significances of several large-angular-scale anomalies are robust to the use of larger sky coverage, with the observed small changes being consistent with expectations from random Gaussian statistics.

Finally, Sect. 8 presents the results of the stacking of temperature and polarization peaks. We find results that are largely consistent with statistically isotropic simulations, both for oriented and unoriented stacking. The exception is a low unoriented temperature profile, which seems to be yet another reflection of the large-scale power deficit.

With the *Planck* 2015 release, we are probably near the limit of our ability to probe the CMB anomalies with temperature fluctuations alone. The use of large-angular-scale polarization, expected for the final *Planck* release, should enable *independent* tests of these peculiar features. Importantly, this will reduce or eliminate the subjectivity and ambiguity in interpreting their statistical significance. It is a tantalizing possibility that some of the anomalies described in this paper will take us beyond the standard model of cosmology.

*Acknowledgements.* The *Planck* Collaboration acknowledges the support of: ESA; CNES and CNRS/INSU-IN2P3-INP (France); ASI, CNR, and INAF (Italy); NASA and DoE (USA); STFC and UKSA (UK); CSIC, MINECO, JA, and RES (Spain); Tekes, AoF, and CSC (Finland); DLR and MPG (Germany); CSA (Canada); DTU Space (Denmark); SER/SSO (Switzerland); RCN (Norway); SFI (Ireland); FCT/MCTES (Portugal); ERC and PRACE (EU). A description of the Planck Collaboration and a list of its members, indicating which technical or scientific activities they have been involved in, can be found at `http://www.cosmos.esa.int/web/planck/planck-collaboration`. Some of the results in this paper have been derived using the `HEALPix` package.

## References

Ackerman, L., Carroll, S. M., & Wise, M. B. 2007, Phys. Rev. D, 75, 083502
Adhikari, S. 2015, MNRAS, 446, 4232
Akrami, Y., Fantaye, Y., Shafieloo, A., et al. 2014, ApJ, 784, L42
Aluri, P. K., Pant, N., Rotti, A., & Souradeep, T. 2015, Phys. Rev. D, 92, 083015
Axelsson, M., Fantaye, Y., Hansen, F. K., et al. 2013, ApJ, 773, L3
Baldi, P., Kerkyacharian, G., Marinucci, D., & Picard, D. 2009, Annals of Statistics, 37, 1150
Bardeen, J. M., Bond, J. R., Kaiser, N., & Szalay, A. S. 1986, ApJ, 304, 15
Ben-David, A., & Kovetz, E. D. 2014, MNRAS, 445, 2116
Bennett, C. L., Halpern, M., Hinshaw, G., et al. 2003, ApJS, 148, 1
Bennett, C. L., Hill, R. S., Hinshaw, G., et al. 2011, ApJS, 192, 17
Bennett, C. L., Larson, D., Weiland, J. L., et al. 2013, ApJS, 208, 20
Bond, J. R., & Efstathiou, G. 1987, MNRAS, 226, 655
Bond, J. R., Frolov, A. V., Huang, Z., & Kofman, L. 2009, Phys. Rev. Lett., 103, 071301
Bueno Sanchez, J. 2014, Phys. Lett. B, 739, 269
Bunn, E. F., & Scott, D. 2000, MNRAS, 313, 331
Cai, Y.-C., Cole, S., Jenkins, A., & Frenk, C. S. 2010, MNRAS, 407, 201
Cayón, L., Jin, J., & Treaster, A. 2005, MNRAS, 362, 826
Challinor, A., & van Leeuwen, F. 2002, Phys. Rev. D, 65, 103001
Copi, C. J., Huterer, D., Schwarz, D. J., & Starkman, G. D. 2007, Phys. Rev. D, 75, 023507
Copi, C. J., Huterer, D., Schwarz, D. J., & Starkman, G. D. 2009, MNRAS, 399, 295
Copi, C. J., Huterer, D., Schwarz, D. J., & Starkman, G. D. 2015, MNRAS, 451, 2978
Coulson, D., Crittenden, R. G., & Turok, N. G. 1994, Phys. Rev. Lett., 73, 2390
Cruz, M., Martínez-González, E., Vielva, P., & Cayón, L. 2005, MNRAS, 356, 29
Cruz, M., Tucci, M., Martínez-González, E., & Vielva, P. 2006, MNRAS, 369, 57
Cruz, M., Turok, N., Vielva, P., Martínez-González, E., & Hobson, M. 2007, Science, 318, 1612
Cruz, M., Martínez-González, E., Vielva, P., et al. 2008, MNRAS, 390, 913
Cruz, M., Vielva, P., Martínez-González, E., & Barreiro, R. B. 2011, MNRAS, 412, 2383
Curto, A., Aumont, J., Macías-Pérez, J. F., et al. 2007, A&A, 474, 23
Curto, A., Macías-Pérez, J. F., Martínez-González, E., et al. 2008, A&A, 486, 383
Curto, A., Martínez-González, E., & Barreiro, R. B. 2011, MNRAS, 412, 1038
Czech, B., Kleban, M., Larjo, K., Levi, T. S., & Sigurdson, K. 2010, J. Cosmol. Astropart. Phys., 12, 23
de Oliveira-Costa, A., Smoot, G. F., & Starobinsky, A. A. 1996, ApJ, 468, 457
De Troia, G., Ade, P. A. R., Bock, J. J., et al. 2007, ApJ, 670, L73
Desjacques, V. 2008, Phys. Rev. D, 78, 103503
Efstathiou, G. 2004, MNRAS, 348, 885
Eriksen, H. K., Hansen, F. K., Banday, A. J., Górski, K. M., & Lilje, P. B. 2004a, ApJ, 605, 14
Eriksen, H. K., Novikov, D. I., Lilje, P. B., Banday, A. J., & Górski, K. M. 2004b, ApJ, 612, 64
Eriksen, H. K., Banday, A. J., Górski, K. M., & Lilje, P. B. 2005, ApJ, 622, 58
Fantaye, Y. 2014, ArXiv e-prints [`arXiv:1409.1114`]
Fantaye, Y., Marinucci, D., Hansen, F., & Maino, D. 2015, Phys. Rev. D, 91, 063501
Feeney, S. M., Johnson, M. C., Mortlock, D. J., & Peiris, H. V. 2011, Phys. Rev. Lett., 107, 071301
Ferreira, P. G., & Magueijo, J. 1997, Phys. Rev. D, 56, 4578
Finelli, F., Gruppuso, A., Paci, F., & Starobinsky, A. 2012, J. Cosmol. Astropart. Phys., 1207, 049
Finelli, F., Garcia-Bellido, J., Kovacs, A., Paci, F., & Szapudi, I. 2016, MNRAS, 455, 1246
Fixsen, D. J., Cheng, E. S., Gales, J. M., et al. 1996, ApJ, 473, 576
Gay, C., Pichon, C., & Pogosyan, D. 2012, Phys. Rev. D, 85, 023011
Gordon, C. 2007, ApJ, 656, 636
Górski, K. M., Hivon, E., Banday, A. J., et al. 2005, ApJ, 622, 759
Gott, J. R., Colley, W. N., Park, C.-G., Park, C., & Mugnolo, C. 2007, MNRAS, 377, 1668
Gruppuso, A., Finelli, F., Natoli, P., et al. 2011, MNRAS, 411, 1445
Gruppuso, A., Natoli, P., Paci, F., et al. 2013, J. Cosmol. Astropart. Phys., 7, 47
Gurzadyan, V. G., Kashin, A. L., Khachatryan, H., et al. 2014, A&A, 566, A135
Hajian, A. 2007, ArXiv e-prints [`arXiv:astro-ph/0702723`]
Hajian, A., & Souradeep, T. 2003, ApJ, 597, L5
Hajian, A., & Souradeep, T. 2006, Phys. Rev. D, 74, 123521
Hansen, F. K., Banday, A. J., Górski, K. M., Eriksen, H. K., & Lilje, P. B. 2009, ApJ, 704, 1448
Hanson, D., & Lewis, A. 2009, Phys. Rev. D, 80, 063004

Hanson, D., Lewis, A., & Challinor, A. 2010, Phys. Rev. D, 81, 103003
Hartlap, J., Simon, P., & Schneider, P. 2007, A&A, 464, 399
Haslam, C. G. T., Salter, C. J., Stoffel, H., & Wilson, W. E. 1982, A&AS, 47, 1
Hikage, C., Matsubara, T., Coles, P., et al. 2008, MNRAS, 389, 1439
Hinshaw, G., Banday, A. J., Bennett, C. L., et al. 1996, ApJ, 464, L25
Hinshaw, G., Weiland, J. L., Hill, R. S., et al. 2009, ApJS, 180, 225
Hoftuft, J., Eriksen, H. K., Banday, A. J., et al. 2009, ApJ, 699, 985
Hou, Z., Banday, A. J., & Górski, K. M. 2009, MNRAS, 396, 1273
Inoue, K. T., & Silk, J. 2006, ApJ, 648, 23
Jaffe, T. R., Banday, A. J., Eriksen, H. K., Górski, K. M., & Hansen, F. K. 2005, ApJ, 629, L1
Kamionkowski, M., & Knox, L. 2003, Phys. Rev. D, 67, 063001
Kamionkowski, M., Kosowsky, A., & Stebbins, A. 1997, Phys. Rev. D, 55, 7368
Kim, J., & Komatsu, E. 2013, Phys. Rev. D, 88, 101301
Kim, J., & Naselsky, P. 2010a, ApJ, 714, L265
Kim, J., & Naselsky, P. 2010b, Phys. Rev. D, 82, 063002
Knutsson, H., & Westin, C.-F. 1993, Conf. IEEE Comput. Soc., 515
Kogut, A., Spergel, D. N., Barnes, C., et al. 2003, ApJS, 148, 161
Komatsu, E., Kogut, A., Nolta, M. R., et al. 2003, ApJS, 148, 119
Komatsu, E., Dunkley, J., Nolta, M. R., et al. 2009, ApJS, 180, 330
Komatsu, E., Smith, K. M., Dunkley, J., et al. 2011, ApJS, 192, 18
Land, K., & Magueijo, J. 2005a, Phys. Rev. Lett., 95, 071301
Land, K., & Magueijo, J. 2005b, Phys. Rev. D, 72, 101302
Larson, D. L., & Wandelt, B. D. 2004, ApJ, 613, L85
Larson, D. L., & Wandelt, B. D. 2005, ArXiv e-prints [arXiv:astro-ph/0505046]
Liu, X., & Zhang, S. N. 2005, ApJ, 633, 542
Marinucci, D., Pietrobon, D., Balbi, A., et al. 2008, MNRAS, 383, 539
Martinez-González, E., Gallegos, J. E., Argüeso, F., Cayón, L., & Sanz, J. L. 2002, MNRAS, 336, 22
Matsubara, T. 2010, Phys. Rev. D, 81, 083505
McEwen, J. D., Hobson, M. P., Lasenby, A. N., & Mortlock, D. J. 2005, MNRAS, 359, 1583
McEwen, J. D., Vielva, P., Wiaux, Y., et al. 2007, J. Fourier Analysis and Applications, 13, 495
McEwen, J. D., Feeney, S. M., Johnson, M. C., & Peiris, H. V. 2012, Phys. Rev. D, 85, 103502
Mecke, K. R., Buchert, T., & Wagner, H. 1994, A&A, 288, 697
Mikkelsen, K., Næss, S. K., & Eriksen, H. K. 2013, ApJ, 777, 172
Mitra, S., Rocha, G., Górski, K. M., et al. 2011, ApJS, 193, 5
Monteserín, C., Barreiro, R. B., Vielva, P., et al. 2008, MNRAS, 387, 209
Moss, A., Scott, D., Zibin, J. P., & Battye, R. 2011, Phys. Rev. D, 84, 023014
Nadathur, S., Lavinto, M., Hotchkiss, S., & Räsänen, S. 2014, Phys. Rev. D., 90, 103510
Notari, A., & Quartin, M. 2015, J. Cosmol. Astropart. Phys., 6, 47
Planck Collaboration I. 2014, A&A, 571, A1
Planck Collaboration XV. 2014, A&A, 571, A15
Planck Collaboration XVI. 2014, A&A, 571, A16
Planck Collaboration XVII. 2014, A&A, 571, A17
Planck Collaboration XIX. 2014, A&A, 571, A19
Planck Collaboration XXIII. 2014, A&A, 571, A23
Planck Collaboration XXVII. 2014, A&A, 571, A27
Planck Collaboration I. 2016, A&A, 594, A1
Planck Collaboration II. 2016, A&A, 594, A2
Planck Collaboration III. 2016, A&A, 594, A3
Planck Collaboration IV. 2016, A&A, 594, A4
Planck Collaboration V. 2016, A&A, 594, A5
Planck Collaboration VI. 2016, A&A, 594, A6
Planck Collaboration VII. 2016, A&A, 594, A7
Planck Collaboration VIII. 2016, A&A, 594, A8
Planck Collaboration IX. 2016, A&A, 594, A9
Planck Collaboration X. 2016, A&A, 594, A10
Planck Collaboration XI. 2016, A&A, 594, A11
Planck Collaboration XII. 2016, A&A, 594, A12
Planck Collaboration XIII. 2016, A&A, 594, A13
Planck Collaboration XIV. 2016, A&A, 594, A14
Planck Collaboration XV. 2016, A&A, 594, A15
Planck Collaboration XVI. 2016, A&A, 594, A16
Planck Collaboration XVII. 2016, A&A, 594, A17
Planck Collaboration XVIII. 2016, A&A, 594, A18
Planck Collaboration XIX. 2016, A&A, 594, A19
Planck Collaboration XX. 2016, A&A, 594, A20
Planck Collaboration XXI. 2016, A&A, 594, A21
Planck Collaboration XXII. 2016, A&A, 594, A22
Planck Collaboration XXIII. 2016, A&A, 594, A23
Planck Collaboration XXIV. 2016, A&A, 594, A24
Planck Collaboration XXV. 2016, A&A, 594, A25
Planck Collaboration XXVI. 2016, A&A, 594, A26
Planck Collaboration XXVII. 2016, A&A, 594, A27
Planck Collaboration XXVIII. 2016, A&A, 594, A28
Plaszczynski, S., Montier, L., Levrier, F., & Tristram, M. 2014, MNRAS, 439, 4048
Pogosyan, D., Gay, C., & Pichon, C. 2009, Phys. Rev. D, 80, 081301
Pontzen, A., & Peiris, H. V. 2010, Phys. Rev. D, 81, 103008
Quartin, M., & Notari, A. 2015, J. Cosmol. Astropart. Phys., 1, 008
Rudnick, L., Brown, S., & Williams, L. R. 2007, ApJ, 671, 40
Savitzky, A., & Golay, M. J. E. 1964, J. Anal. Chem., 36, 1627
Schmalzing, J., & Buchert, T. 1997, ApJ, 482, L1
Schmalzing, J., & Gorski, K. M. 1998, MNRAS, 297, 355
Scott, D. 1991, A&A, 242, 1
Spergel, D. N., Verde, L., Peiris, H. V., et al. 2003, ApJS, 148, 175
Spergel, D. N., Bean, R., Doré, O., et al. 2007, ApJS, 170, 377
Stannard, A., & Coles, P. 2005, MNRAS, 364, 929
Starobinsky, A. A. 1993, JETP Lett., 57, 622
Stevens, D., Scott, D., & Silk, J. 1993, Phys. Rev. Lett., 71, 20
Szapudi, I., Kovács, A., Granett, B. R., et al. 2015, MNRAS, 450, 288
Tegmark, M., de Oliveira-Costa, A., & Hamilton, A. 2003, Phys. Rev. D, 68, 123523
Tomita, K. 2005, Phys. Rev. D, 72, 103506
Tomita, K., & Inoue, K. T. 2008, Phys. Rev. D, 77, 103522
Vanmarcke, E. 1983, in Random Fields (Cambridge, Massachusetts, USA: The MIT Press), March (Paper), ed. E. Vanmarcke, 372
Vielva, P. 2007, in SPIE Conf. Ser., 6701
Vielva, P. 2010, Adv. Astron., 2010, 592094
Vielva, P., Martínez-González, E., Barreiro, R. B., Sanz, J. L., & Cayón, L. 2004, ApJ, 609, 22
Vielva, P., Wiaux, Y., Martínez-González, E., & Vandergheynst, P. 2007, MNRAS, 381, 932
Watson, W. A., Diego, J. M., Gottlöber, S., et al. 2014, MNRAS, 438, 412
Wick, G. C. 1950, Phys. Rev., 80, 268
Zaldarriaga, M., & Seljak, U. 1997, Phys. Rev. D, 55, 1830
Zhang, R., & Huterer, D. 2010, Astropart. Phys., 33, 69
Zhao, W. 2013, MNRAS, 433, 3498
Zibin, J. P. 2014, ArXiv e-prints [arXiv:1408.4442]

---

[1] APC, AstroParticule et Cosmologie, Université Paris Diderot, CNRS/IN2P3, CEA/lrfu, Observatoire de Paris, Sorbonne Paris Cité, 10 rue Alice Domon et Léonie Duquet, 75205 Paris Cedex 13, France

[2] Aalto University Metsähovi Radio Observatory and Dept of Radio Science and Engineering, PO Box 13000, 00076 AALTO, Finland

[3] African Institute for Mathematical Sciences, 6–8 Melrose Road, Muizenberg, Cape Town, South Africa

[4] Agenzia Spaziale Italiana Science Data Center, via del Politecnico snc, 00133 Roma, Italy

[5] Aix Marseille Université, CNRS, LAM (Laboratoire d'Astrophysique de Marseille) UMR 7326, 13388 Marseille, France

[6] Astrophysics Group, Cavendish Laboratory, University of Cambridge, J J Thomson Avenue, Cambridge CB3 0HE, UK

[7] Astrophysics & Cosmology Research Unit, School of Mathematics, Statistics & Computer Science, University of KwaZulu-Natal, Westville Campus, Private Bag X54001, 4000 Durban, South Africa

[8] CITA, University of Toronto, 60 St. George St., Toronto, ON M5S 3H8, Canada

[9] CNRS, IRAP, 9 Av. colonel Roche, BP 44346, 31028 Toulouse Cedex 4, France

[10] CRANN, Trinity College, Dublin, Ireland

[11] California Institute of Technology, Pasadena, California CA 91125, USA

[12] Centre for Theoretical Cosmology, DAMTP, University of Cambridge, Wilberforce Road, Cambridge CB3 0WA, UK

[13] Centro de Estudios de Física del Cosmos de Aragón (CEFCA), Plaza San Juan, 1, planta 2, 44001 Teruel, Spain

[14] Computational Cosmology Center, Lawrence Berkeley National Laboratory, Berkeley, California, USA

[15] Consejo Superior de Investigaciones Científicas (CSIC), Madrid, Spain

[16] DSM/Irfu/SPP, CEA-Saclay, 91191 Gif-sur-Yvette Cedex, France

[17] DTU Space, National Space Institute, Technical University of Denmark, Elektrovej 327, 2800 Kgs. Lyngby, Denmark
[18] Départment de Physique Théorique, Université de Genève, 24 Quai E. Ansermet,1211 Genève 4, Switzerland
[19] Departamento de Astrofísica, Universidad de La Laguna (ULL), 38206 La Laguna, Tenerife, Spain
[20] Departamento de Física, Universidad de Oviedo, Avda. Calvo Sotelo s/n, 33003 Oviedo, Spain
[21] Departamento de Matemáticas, Estadística y Computación, Universidad de Cantabria, Avda. de los Castros s/n, 39005 Santander, Spain
[22] Department of Astronomy and Astrophysics, University of Toronto, 50 Saint George Street, Toronto, Ontario, Canada
[23] Department of Astrophysics/IMAPP, Radboud University Nijmegen, PO Box 9010, 6500 GL Nijmegen, The Netherlands
[24] Department of Physics & Astronomy, University of British Columbia, 6224 Agricultural Road, Vancouver, British Columbia, Canada
[25] Department of Physics and Astronomy, Dana and David Dornsife College of Letter, Arts and Sciences, University of Southern California, Los Angeles, CA 90089, USA
[26] Department of Physics and Astronomy, University College London, London WC1E 6BT, UK
[27] Department of Physics, Florida State University, Keen Physics Building, 77 Chieftan Way, Tallahassee, Florida, USA
[28] Department of Physics, Gustaf Hällströmin katu 2a, University of Helsinki, 00100 Helsinki, Finland
[29] Department of Physics, Princeton University, Princeton, New Jersey NJ 08544, USA
[30] Department of Physics, University of California, Santa Barbara, California CA 93106, USA
[31] Department of Physics, University of Illinois at Urbana-Champaign, 1110 West Green Street, Urbana, Illinois, USA
[32] Dipartimento di Fisica e Astronomia G. Galilei, Università degli Studi di Padova, via Marzolo 8, 35131 Padova, Italy
[33] Dipartimento di Fisica e Scienze della Terra, Università di Ferrara, via Saragat 1, 44122 Ferrara, Italy
[34] Dipartimento di Fisica, Università La Sapienza, P. le A. Moro 2, Roma, Italy
[35] Dipartimento di Fisica, Università degli Studi di Milano, via Celoria, 16 Milano, Italy
[36] Dipartimento di Fisica, Università degli Studi di Trieste, via A. Valerio 2, Trieste, Italy
[37] Dipartimento di Matematica, Università di Roma Tor Vergata, via della Ricerca Scientifica, 1 Roma, Italy
[38] Discovery Center, Niels Bohr Institute, 17 Blegdamsvej, Copenhagen, Denmark
[39] European Space Agency, ESAC, Planck Science Office, Camino bajo del Castillo, s/n, Urbanización Villafranca del Castillo, Villanueva de la Cañada, 28692 Madrid, Spain
[40] European Space Agency, ESTEC, Keplerlaan 1, 2201 AZ Noordwijk, The Netherlands
[41] Facoltà di Ingegneria, Università degli Studi e-Campus, via Isimbardi 10, 22060 Novedrate (CO), Italy
[42] Gran Sasso Science Institute, INFN, viale F. Crispi 7, 67100 L'Aquila, Italy
[43] HGSFP and University of Heidelberg, Theoretical Physics Department, Philosophenweg 16, 69120 Heidelberg, Germany
[44] Helsinki Institute of Physics, Gustaf Hällströmin katu 2, University of Helsinki, Helsinki, Finland
[45] INAF–Osservatorio Astronomico di Padova, Vicolo dell'Osservatorio 5, Padova, Italy
[46] INAF–Osservatorio Astronomico di Roma, via di Frascati 33, Monte Porzio Catone, Italy
[47] INAF–Osservatorio Astronomico di Trieste, via G.B. Tiepolo 11, Trieste, Italy
[48] INAF/IASF Bologna, via Gobetti 101, Bologna, Italy
[49] INAF/IASF Milano, via E. Bassini 15, Milano, Italy
[50] INFN, Sezione di Bologna, via Irnerio 46, 40126 Bologna, Italy
[51] INFN, Sezione di Roma 1, Università di Roma Sapienza, Piazzale Aldo Moro 2, 00185 Roma, Italy
[52] INFN, Sezione di Roma 2, Università di Roma Tor Vergata, via della Ricerca Scientifica, 1 Roma, Italy
[53] INFN/National Institute for Nuclear Physics, via Valerio 2, 34127 Trieste, Italy
[54] IPAG: Institut de Planétologie et d'Astrophysique de Grenoble, Université Grenoble Alpes, IPAG; CNRS, IPAG, 38000 Grenoble, France
[55] IUCAA, Post Bag 4, Ganeshkhind, Pune University Campus, 411 007 Pune, India
[56] Imperial College London, Astrophysics group, Blackett Laboratory, Prince Consort Road, London, SW7 2AZ, UK
[57] Infrared Processing and Analysis Center, California Institute of Technology, Pasadena, CA 91125, USA
[58] Institut Néel, CNRS, Université Joseph Fourier Grenoble I, 25 rue des Martyrs, Grenoble, France
[59] Institut Universitaire de France, 103 bd Saint-Michel, 75005 Paris, France
[60] Institut d'Astrophysique Spatiale, CNRS (UMR 8617) Université Paris-Sud 11, Bâtiment 121, 91440 Orsay, France
[61] Institut d'Astrophysique de Paris, CNRS (UMR 7095), 98 bis Boulevard Arago, 75014 Paris, France
[62] Institut für Theoretische Teilchenphysik und Kosmologie, RWTH Aachen University, 52056 Aachen, Germany
[63] Institute for Space Sciences, Bucharest-Magurale, 077125 Romania
[64] Institute of Astronomy, University of Cambridge, Madingley Road, Cambridge CB3 0HA, UK
[65] Institute of Theoretical Astrophysics, University of Oslo, Blindern, 0371 Oslo, Norway
[66] Instituto de Astrofísica de Canarias, C/Vía Láctea s/n, La Laguna, 38205 Tenerife, Spain
[67] Instituto de Física de Cantabria (CSIC-Universidad de Cantabria), Avda. de los Castros s/n, 39005 Santander, Spain
[68] Istituto Nazionale di Fisica Nucleare, Sezione di Padova, via Marzolo 8, 35131 Padova, Italy
[69] Jet Propulsion Laboratory, California Institute of Technology, 4800 Oak Grove Drive, Pasadena, California, USA
[70] Jodrell Bank Centre for Astrophysics, Alan Turing Building, School of Physics and Astronomy, The University of Manchester, Oxford Road, Manchester, M13 9PL, UK
[71] Kavli Institute for Cosmological Physics, University of Chicago, Chicago, IL 60637, USA
[72] Kavli Institute for Cosmology Cambridge, Madingley Road, Cambridge, CB3 0HA, UK
[73] Kazan Federal University, 18 Kremlyovskaya St., 420008 Kazan, Russia
[74] LAL, Université Paris-Sud, CNRS/IN2P3, Orsay, France
[75] LERMA, CNRS, Observatoire de Paris, 61 Avenue de l'Observatoire, 75014 Paris, France
[76] Laboratoire AIM, IRFU/Service d'Astrophysique – CEA/DSM – CNRS – Université Paris Diderot, Bât. 709, CEA-Saclay, 91191 Gif-sur-Yvette Cedex, France
[77] Laboratoire Traitement et Communication de l'Information, CNRS (UMR 5141) and Télécom ParisTech, 46 rue Barrault, 75634 Paris Cedex 13, France
[78] Laboratoire de Physique Subatomique et Cosmologie, Université Grenoble-Alpes, CNRS/IN2P3, 53 rue des Martyrs, 38026 Grenoble Cedex, France
[79] Laboratoire de Physique Théorique, Université Paris-Sud 11 & CNRS, Bâtiment 210, 91405 Orsay, France
[80] Lawrence Berkeley National Laboratory, Berkeley, California, USA
[81] Lebedev Physical Institute of the Russian Academy of Sciences, Astro Space Centre, 84/32 Profsoyuznaya st., GSP-7, 117997 Moscow, Russia
[82] Leung Center for Cosmology and Particle Astrophysics, National Taiwan University, 10617 Taipei, Taiwan
[83] Max-Planck-Institut für Astrophysik, Karl-Schwarzschild-Str. 1, 85741 Garching, Germany

[84] McGill Physics, Ernest Rutherford Physics Building, McGill University, 3600 rue University, Montréal, QC, H3A 2T8, Canada
[85] National University of Ireland, Department of Experimental Physics, Maynooth, Co. Kildare, Ireland
[86] Nicolaus Copernicus Astronomical Center, Bartycka 18, 00-716 Warsaw, Poland
[87] Niels Bohr Institute, Blegdamsvej 17, 2100 Copenhagen, Denmark
[88] Optical Science Laboratory, University College London, Gower Street, London, UK
[89] SISSA, Astrophysics Sector, via Bonomea 265, 34136 Trieste, Italy
[90] School of Physics and Astronomy, Cardiff University, Queens Buildings, The Parade, Cardiff, CF24 3AA, UK
[91] School of Physics and Astronomy, University of Nottingham, Nottingham NG7 2RD, UK
[92] Simon Fraser University, Department of Physics, 8888 University Drive, Burnaby BC, Canada
[93] Sorbonne Université-UPMC, UMR 7095, Institut d'Astrophysique de Paris, 98 bis Boulevard Arago, 75014 Paris, France
[94] Space Research Institute (IKI), Russian Academy of Sciences, Profsoyuznaya Str, 84/32, 117997 Moscow, Russia
[95] Space Sciences Laboratory, University of California, Berkeley, California, USA
[96] Special Astrophysical Observatory, Russian Academy of Sciences, Nizhnij Arkhyz, Zelenchukskiy region, 369167 Karachai-Cherkessian Republic, Russia
[97] Stanford University, Dept of Physics, Varian Physics Bldg, 382 via Pueblo Mall, Stanford, California, USA
[98] Sub-Department of Astrophysics, University of Oxford, Keble Road, Oxford OX1 3RH, UK
[99] Theory Division, PH-TH, CERN, 1211, Geneva 23, Switzerland
[100] UPMC Univ Paris 06, UMR 7095, 98 bis Boulevard Arago, 75014 Paris, France
[101] Université de Toulouse, UPS-OMP, IRAP, 31028 Toulouse Cedex 4, France
[102] University of Granada, Departamento de Física Teórica y del Cosmos, Facultad de Ciencias, 18071 Granada, Spain
[103] University of Granada, Instituto Carlos I de Física Teórica y Computacional, 18071 Granada, Spain
[104] University of Heidelberg, Institute for Theoretical Physics, Philosophenweg 16, 69120 Heidelberg, Germany
[105] Warsaw University Observatory, Aleje Ujazdowskie 4, 00-478 Warszawa, Poland

## Appendix A: Generalized Savitzky-Golay polynomials

In the construction of optimal linear filters, one needs to combine information about the (statistically isotropic) CMB signal, anisotropic instrumental noise, masking to be applied for the elimination of foreground contributions, and a model for any non-Gaussian signal for matched filtering. These can be combined in a general framework of normalized convolutions (Knutsson & Westin 1993), where the filtered field is defined as

$$U = \frac{a\boldsymbol{B} \star w\boldsymbol{T}}{a\boldsymbol{B} \star \boldsymbol{B}^{\dagger} w}, \tag{A.1}$$

where $\boldsymbol{B}$ is the (multiscale) filtering beam function, $\boldsymbol{T}$ is the temperature, $a$ and $w$ their respective weights, and $\star$ denotes the usual convolution operation

$$\{a\boldsymbol{B} \star w\boldsymbol{T}\}(\boldsymbol{\xi}) = \sum_{\boldsymbol{x}} a(\boldsymbol{x})\boldsymbol{B}(\boldsymbol{x}) \cdot w(\boldsymbol{\xi} - \boldsymbol{x})\boldsymbol{T}(\boldsymbol{\xi} - \boldsymbol{x}). \tag{A.2}$$

In the absence of a specific model for the non-Gaussian signal, the beam functions can be taken to be orthogonal polynomials on a disc, weighted by some smoothing function, while the weights applied to the temperature maps are determined by the CMB and noise covariance.

In a simple approach, the information about the CMB signal can be utilized by pre-whitening the map by convolving it with an isotropic beam function $w_\ell = C_\ell^{-1/2}$ derived from the isotropic best-fit CMB power spectrum combined with a diagonal approximation to the instrumental noise covariance. After the component-separated CMB maps are pre-whitened, and the corresponding mask is applied to the resulting map, the multiscale filtering kernel $b_\ell$ is applied at various scales.

In this paper, the maps are pre-whitened with the 2013 best-fit cosmological parameter CMB spectrum (Planck Collaboration XV 2014), co-added to an isotropic noise power spectrum derived from the half-mission, half-difference noise maps appropriate for each component-separation method. No adjustment is made either for the recalibration of the 2015 data relative to the nominal results that the cosmological spectrum is derived from, or for the mismatch in noise level between the half-mission, half-difference and full-mission maps. This implies that the filtering is sub-optimal, but the data and simulations are treated consistently so there should be no significant impact on the results. The resulting pre-whitening beam function $w_\ell$ for the `SMICA` temperature map is shown in Fig. A.1.

The peak detector wavelets are taken to be Savitzky-Golay polynomials (Savitzky & Golay 1964), generalized to be defined on a disc with a polynomial smoothing weight function applied, as shown in Fig. A.1. A generalized spherical Savitzky-Golay kernel of order $n$ and smoothing weight $k$ (referred to as `SSGnk` in the text) is defined by a polynomial function of a radial variable $x = \sin(\theta/2)/\sin(\theta_{\max}/2)$,

$$F_{n,k}(x) = \left(\sum_{i=0}^{n/2} a_i x^{2i}\right)\left(1 - x^2\right)^k, \tag{A.3}$$

which is normalized to have unit mean on a disc and is orthogonal to all non-constant polynomials up to order $n$,

$$\int_0^1 x F_{n,k}(x)\,\mathrm{d}x = 1, \qquad \int_0^1 x^{i+1} F_{n,k}(x)\,\mathrm{d}x = 0. \tag{A.4}$$

These are essentially high-order low-pass filters in harmonic space, but have compact support on the sphere. A few representative Savitzky-Golay polynomials are compared to a Gaussian kernel in Fig. A.1. Combined with pre-whitening, the total effect of the filters applied is described by the composite beam functions shown in Fig. A.1.

One should note a slight $\ell$-space bandwidth mismatch between differently shaped kernels with the same FWHM value in real space, which is clear from the lower left panel of Fig. A.1. While not a problem in general, some care should be exercised when directly comparing results for different shape kernels. In particular, the $\ell$ value at which the filter kernel coefficient reaches $b_\ell = b_{\max}/2$ differs by a factor of 1.58 between the `GAUSS` and `SSG84` kernels of the same FWHM.

## Appendix B: Doppler boosting

The main effect of our relative motion with respect to the CMB rest frame is a dominant contribution to the CMB dipole ($C_1$); this is boosting of the monopole and has been detected previously (Kogut et al. 2003; Fixsen et al. 1996; Hinshaw et al. 2009). A subtler consequence of our motion is the boosting of all other multipoles. In fact, there are really two effects at work. The first is a modulation effect which increases power by approximately 0.25% in the direction of our motion and decreases it by the same amount in the opposite direction. This can equivalently be thought of as coupling between the multipoles $\ell$ and $\ell \pm 1$. The second is an aberration effect which shifts the apparent direction in which CMB photons arrive at our detectors toward the velocity direction.

Planck Collaboration XXVII (2014) reported a detection of this Doppler boosting, and an associated measurement of its velocity signature of $384 \pm 78$ (statistical) $\pm\ 115$ (systematic) $\mathrm{km\,s^{-1}}$ in the known dipole direction, $(l, b) = (264°, 48°)$. Here, we demonstrate that the *Planck* 2015 data release remains in agreement with this result, by considering the angular scales $500 \leq \ell \leq 2000$. However, since the simulations employed in the analysis partially contain the effects of Doppler boosting (as noted in Sect. 3 the aberration contribution was erroneously omitted), we report a consistency check rather than a detection.

It is useful to perform a harmonic transform on the peculiar velocity vector,

$$\beta_{\mathrm{LM}} = \int \mathrm{d}\hat{\boldsymbol{n}}\, Y^*_{\mathrm{LM}}(\hat{\boldsymbol{n}})\boldsymbol{\beta} \cdot \hat{\boldsymbol{n}}, \tag{B.1}$$

where only the $L = 1$ modes are non-zero. Following the convention in Planck Collaboration XXVII (2014), we rotate to an orthonormal basis, labelled $\boldsymbol{\beta}_{\parallel}$ (along the expected velocity direction), $\boldsymbol{\beta}_{\times}$ (parallel to the Galactic plane), and $\boldsymbol{\beta}_{\perp}$ (the remaining vector).

The peculiar velocity is detected using estimators that pick out the off-diagonal components of the CMB covariance matrix

$$\langle T_{\ell_1 m_1} T_{\ell_2 m_2} \rangle_{\mathrm{CMB}} = \sum_{\mathrm{LM}} (-1)^M \begin{pmatrix} \ell_1 & \ell_2 & L \\ m_1 & m_2 & M \end{pmatrix} \times \sqrt{\frac{(2\ell_1 + 1)(2\ell_2 + 1)(2L + 1)}{4\pi}}\, W^{\beta_v}_{\ell_1 \ell_2 L} \beta_{\mathrm{LM}}. \tag{B.2}$$

The weight function $W^{\beta_v}$ is a sum of the modulation ($b_v W^{\tau}$) and aberration ($W^{\phi}$) effects. We quote results based on orthogonalized weight matrices,

$$W^{\hat{\phi}} = W^{\phi} - W^{\tau}\mathcal{R}^{\phi\tau}/\mathcal{R}^{\tau\tau} \tag{B.3}$$

$$W^{\hat{\tau}} = W^{\tau} - W^{\phi}\mathcal{R}^{\tau\phi}/\mathcal{R}^{\phi\phi}. \tag{B.4}$$

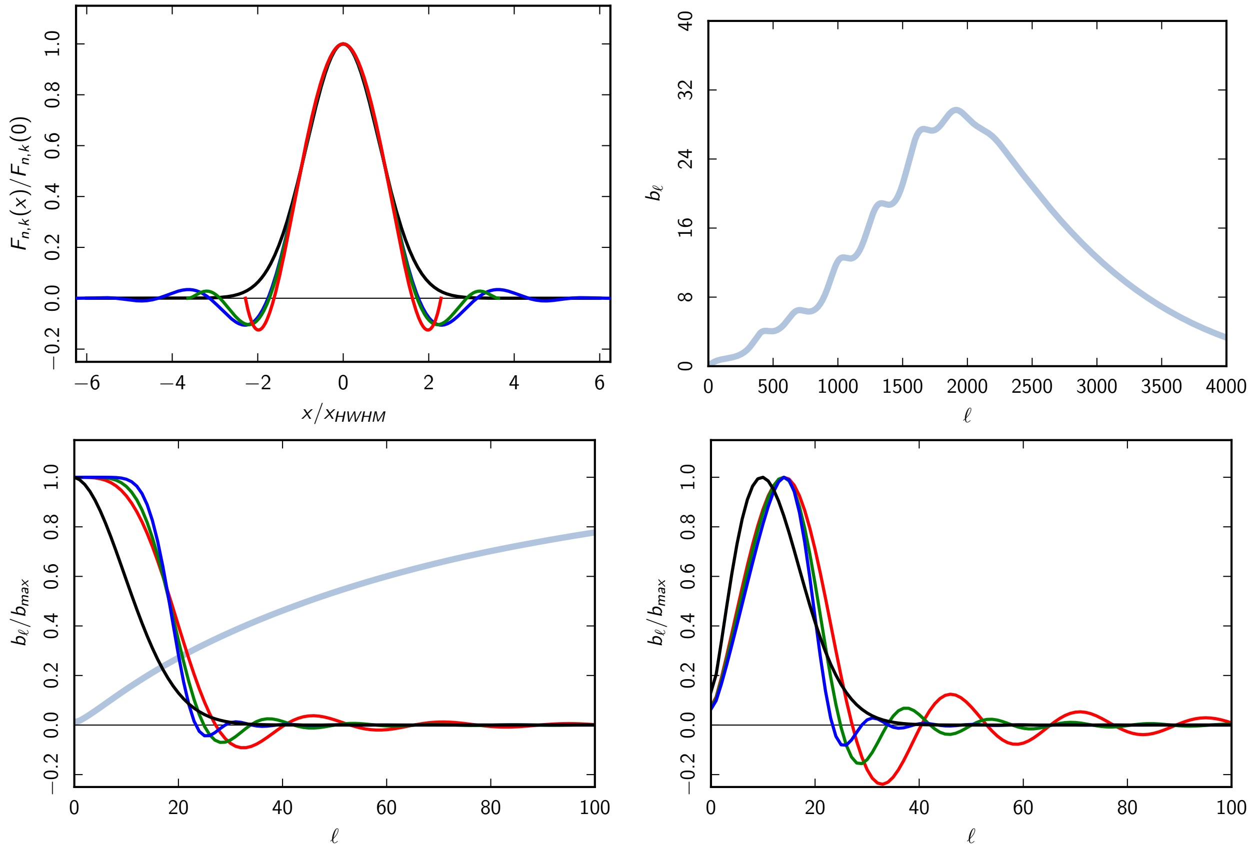

**Fig. A.1.** Generalized Savitzky-Golay polynomials are orthogonal to polynomials up to degree $n$ on a disc, with smoothing weight applied. *Upper left panel* shows a few representative polynomial kernels (`SSG21` in red, `SSG42` in dark green, `SSG84` in blue) and Gaussian (in black) as a function of radius (scaled to the same FWHM of 800′), *lower left* shows their harmonic space representation. *Right column* shows the pre-whitening kernel for the `SMICA` temperature map on the *top* (in light blue), and the corresponding composite kernels (`WHITE*SSG21`, etc.) on the *bottom* (in the same colours).

**Table B.1.** Significance measures for the $\boldsymbol{\beta}$ estimates for the 143 × 217 data set.

| Estimator | $\chi^2$ | PTE [%] |
|---|---|---|
| $\hat{\beta}_\parallel$ . . . . . . . . . . . . . | 3.28 | 7.01 |
| $\hat{\beta}_\perp$ . . . . . . . . . . . . . | 0.21 | 64.39 |
| $\hat{\beta}_\times$ . . . . . . . . . . . . . | 0.08 | 77.53 |
| $\hat{\boldsymbol{\beta}}$ . . . . . . . . . . . . . | 3.38 | 33.70 |

**Notes.** $\chi^2$ is formed from the three modes of $\boldsymbol{\beta}$ using the covariance matrix measured from Doppler boosted simulations.

Due to the clear connection between the velocity estimators and those used for the lensing analysis, we adopt the same data (143 GHz and 217 GHz sky maps, with dust foregrounds removed using the 857 GHz data as a template) and mask as used in Planck Collaboration XV (2016). The results summarized in Table B.1 show a slight excess of signal in the dipole direction of the data compared to simulations. This is due to the simulations used containing the modulation, but not aberration, part of the Doppler boost signal.

## Appendix C: Generalized modulation estimator

Consider a parameter $X$ that the (primary) CMB power spectrum is dependent on. Let $X$ have a dipolar dependence of the form $X(\hat{\boldsymbol{n}}) = X_0 + \Delta X \hat{\boldsymbol{n}} \cdot \hat{\boldsymbol{m}}$ (this could correspond to a gradient in $X$ across our observable volume), where $X_0$ is the average value, $\hat{\boldsymbol{n}}$ is the direction to the last scattering surface, and $\hat{\boldsymbol{m}}$ is the gradient direction. To linear order in $\Delta X/X$, the measured spherical harmonics coefficients are given by

$$a_{\ell m} = a^{\rm iso}_{\ell m} + \sum_M \Delta X_M \sum_{\ell' m'} \frac{{\rm d}a^{\rm iso}_{\ell' m'}}{{\rm d}X} \xi^M_{\ell m \ell' m'}, \tag{C.1}$$

where the $a^{\rm iso}_{\ell m}$ are the unmodulated statistically isotropic modes. The $\xi^M_{\ell m \ell' m'}$ are coupling coefficients given by

$$\xi^0_{\ell m \ell' m'} = \delta_{m' m} \left( \delta_{\ell' \ell-1} A_{\ell-1\, m} + \delta_{\ell' \ell+1} A_{\ell m} \right), \tag{C.2}$$

$$\xi^{\pm 1}_{\ell m \ell' m'} = \delta_{m' m \mp 1} \left( \delta_{\ell' \ell-1} B_{\ell-1\, \pm m-1} - \delta_{\ell' \ell+1} B_{\ell\, \mp m} \right), \tag{C.3}$$

where

$$A_{\ell m} = \sqrt{\frac{(\ell+1)^2 - m^2}{(2\ell+1)(2\ell+3)}}, \tag{C.4}$$

$$B_{\ell m} = \sqrt{\frac{(\ell+m+1)(\ell+m+2)}{2(2\ell+1)(2\ell+3)}}. \tag{C.5}$$

From Eq. (C.1) we can find the covariance matrix to first order in the components $\Delta X_M$:

$$C_{\ell m \ell' m'} = C_\ell \delta_{\ell \ell'} \delta_{m m'} + \frac{\delta C_{\ell \ell'}}{2} \sum_M \Delta X_M \xi^M_{\ell m \ell' m'}, \tag{C.6}$$

where $\delta C_{\ell\ell+1} = \mathrm{d}C_\ell/\mathrm{d}X + \mathrm{d}C_{\ell+1}/\mathrm{d}X$. To determine the best-fit parameters, we proceed by maximizing the CMB likelihood function

$$\mathcal{L} = \frac{1}{\sqrt{2\pi|C|}}\exp(-\boldsymbol{d}^\dagger C^{-1}\boldsymbol{d}/2), \tag{C.7}$$

where $\boldsymbol{d}$ is the CMB temperature data. Equation (C.7) is maximized for the $\Delta X_M$ that satisfy

$$\boldsymbol{d}^\dagger C^{-1}\frac{\mathrm{d}C}{\mathrm{d}\Delta X_M}C^{-1}\boldsymbol{d} = \mathrm{Tr}\left[\left(C^{-1}\frac{\mathrm{d}C}{\mathrm{d}\Delta X_M}\right)\right]. \tag{C.8}$$

From Eq. (C.6) it is clear that the CMB covariance can be decomposed into an isotropic part ($C_\ell$) and a small anisotropic part proportional to $\Delta X_M$. By inverting Eq. (C.6) and using the orthogonality of the $\xi^M_{\ell m\ell' m'}$, we can determine the best-fit parameters

$$\Delta X_0 = \frac{6\sum_{\ell m}\frac{\delta C_{\ell\ell+1}}{C_\ell C_{\ell+1}}A_{\ell m}a^*_{\ell m}a_{\ell+1\,m}}{\sum_\ell \frac{\delta C^2_{\ell\ell+1}}{C_\ell C_{\ell+1}}(\ell+1)}, \tag{C.9}$$

$$\Delta X_{+1} = \frac{6\sum_{\ell m}\frac{\delta C_{\ell\ell+1}}{C_\ell C_{\ell+1}}B_{\ell m}a^*_{\ell m}a_{\ell+1\,m+1}}{\sum_\ell \frac{\delta C^2_{\ell\ell+1}}{C_\ell C_{\ell+1}}(\ell+1)}, \tag{C.10}$$

and $\Delta X_{-1} = -\Delta X^*_{+1}$, to first order in the anisotropy. These estimators are the full-sky, no-noise versions of Eqs. (44) and (45).

Errors can easily be found by expanding the log-likelihood about the best-fit parameters. The Fisher matrix is defined as

$$F_{MM'} \equiv \frac{1}{2}\mathrm{Tr}\left[\left(\frac{\partial C}{\partial\Delta X_M}C^{-1}\frac{\partial C}{\partial\Delta X_{M'}}C^{-1}\right)\right]. \tag{C.11}$$

Upon switching bases, we find

$$F_{0,0} = \frac{1}{4}\sum_{\ell m}\frac{\delta C^2_{\ell\ell+1}}{C_\ell C_{\ell+1}}A^2_{\ell m}, \tag{C.12}$$

$$F_{\Re(\Delta X_{+1}),\Re(\Delta X_{+1})} = \frac{1}{2}\sum_{\ell m}\frac{\delta C^2_{\ell\ell+1}}{C_\ell C_{\ell+1}}B^2_{\ell m}. \tag{C.13}$$

We can then assign the standard errors, $\sigma = \sqrt{F^{-1}}$.

## Appendix D: Weighted-variance modified shape function estimator

The BipoSH representation characterizes the off-diagonal elements in the covariance matrix and is a generalization of the angular power spectrum, $C_\ell$,

$$A^{\mathrm{LM}}_{\ell_1\ell_2} = \sum_{m_1 m_2}\langle a_{\ell_1 m_1}a_{\ell_2 m_2}\rangle C^{\mathrm{LM}}_{\ell_1 m_1 \ell_2 m_2}. \tag{D.1}$$

In general, it is not possible to analyse the full sky even for component-separated maps, due to the presence of residual contributions from diffuse Galactic emission and point sources. However, the application of a mask leads to coupling between the spherical harmonic modes. Hence, the correlation function is no longer described only by $C(\theta)$ or the power spectrum $C_\ell$, and other quantities are required to completely quantify the statistical field.

We obtain an analytic expression for the observed BipoSH coefficients after the application of a mask in terms of the corresponding coefficients of the unmasked sky, and those of the mask itself,

$$\begin{aligned}\tilde{A}^{\mathrm{LM}}_{\ell_1\ell_2} = {} & \sum_{\ell_3\ell_4}\frac{\Pi_{\ell_3\ell_4}}{\sqrt{4\pi}}\sum_{\ell_5\ell_6}\frac{\Pi_{\ell_5\ell_6}}{\sqrt{4\pi}}C^{\ell_1 0}_{\ell_3 0\ell_5 0}C^{\ell_2 0}_{\ell_4 0\ell_6 0} \\ & \times\sum_{L_1 M_1 JK}\begin{Bmatrix} L & \ell_1 & \ell_2 \\ L_1 & \ell_3 & \ell_4 \\ J & \ell_5 & \ell_6 \end{Bmatrix}\Pi_{L_1}\Pi_J A^{L_1 M_1}_{\ell_3\ell_4}W^{JK}_{\ell_5\ell_6}C^{\mathrm{LM}}_{L_1 M_1 JK}\end{aligned} \tag{D.2}$$

where $\Pi_\ell = \sqrt{2\ell+1}$, $\tilde{A}^{\mathrm{LM}}_{\ell_1\ell_2}$ are the BipoSH coefficients of the masked sky map, $A^{\mathrm{LM}}_{\ell_1\ell_2}$ correspond to the BipoSH coefficients of the unmasked sky, $W^{\mathrm{LM}}_{\ell_1\ell_2}$ are the BipoSH coefficient of the mask itself, $C^{\mathrm{LM}}_{lml'm'}$ are the Clebsch-Gordon coefficients, and the term $\{\}$ in Eq. (D.2) is the $9j$–symbol. This quantifies the coupling between the BipoSH coefficients of the CMB sky map and those of the mask itself.

The underlying CMB sky may have deviations from statistical isotropy, as discussed in Sect. 6.4, due either to a dipole modulation ($L = 1$) of unknown origin, or to Doppler boosting ($L = 1$) of the temperature field. The BipoSH coefficients of such statistical isotropy-violating fields can be given by

$$A^{\mathrm{LM}}_{\ell_1\ell_2} = \bar{A}^{\mathrm{LM}}_{\ell_1\ell_2} + \phi_{\mathrm{LM}}G^{\mathrm{L}}_{\ell_1\ell_2}. \tag{D.3}$$

Here $\bar{A}^{\mathrm{LM}}_{\ell_1\ell_2}$ corresponds to the BipoSH coefficients of the unknown but statistically isotropic CMB field. This couples with BipoSH coefficients of the mask to introduce a mean field linear bias $\langle\mathcal{A}^{\mathrm{LM}}_{\ell_1\ell_2}\rangle_{\mathrm{mask}}$, which is estimated from simulations and subtracted from the BipoSH coefficients obtained from the masked sky. The $\phi_{\mathrm{LM}}$ are the spherical harmonic coefficients of the field that breaks statistical isotropy, and $G^{\mathrm{L}}_{\ell_1\ell_2}$ is the shape function. Shape functions for dipole modulation and Doppler boosting are given in Eqs. (54) and (56), respectively.

Due to symmetries of the mask, which is largely defined by foreground residuals towards the Galactic plane, the dominant BipoSH modes of the mask correspond to $J = \{0, 2\}, K = 0$. Hence, for all practical purposes, signal is retained in the $L = 1$ mode itself, although masking modifies the shape function, now defined as the modified shape funtion in the rest of the text. A weighted variance modified shape function is defined as

$$\hat{\phi}_{\mathrm{LM}} = \sum_{\ell_1\ell_2}w^{\mathrm{LM}}_{\ell_1\ell_2}\frac{\hat{A}^{\mathrm{LM}}_{\ell_1\ell_2}}{K^{\mathrm{LM}}_{\ell_1\,\ell_2}}, \tag{D.4}$$

where $\hat{A}^{\mathrm{LM}}_{\ell_1\ell_2} = \tilde{A}^{\mathrm{LM}}_{\ell_1\ell_2} - \langle\mathcal{A}^{\mathrm{LM}}_{\ell_1\ell_2}\rangle_{\mathrm{mask}}$ and the weights are chosen such that $\sum_{\ell_1\ell_2}w^{\mathrm{LM}}_{\ell_1\ell_2} = 1$.

Here $K^{\mathrm{LM}}_{\ell_1\,\ell_2}$ is the MSF, which can be evaluated as

$$\begin{aligned}K^{\mathrm{LM}}_{\ell_1\,\ell_2} = {} & \sum_{\ell_3\ell_4}\Pi_L G^{\mathrm{L}}_{\ell_3\ell_4}\frac{\Pi_{\ell_3\ell_4}}{\sqrt{4\pi}}\sum_{\ell_5\ell_6}\frac{\Pi_{\ell_5\ell_6}}{\sqrt{4\pi}}C^{\ell_1 0}_{\ell_3 0\ell_5 0}C^{\ell_2 0}_{\ell_4 0\ell_6 0} \\ & \times\sum_{JK}\begin{Bmatrix} L & \ell_1 & \ell_2 \\ L & \ell_3 & \ell_4 \\ J & \ell_5 & \ell_6 \end{Bmatrix}\Pi_J W^{JK}_{\ell_5\ell_6}C^{\mathrm{LM}}_{LMJK}.\end{aligned} \tag{D.5}$$

The weights are then given by

$$w_{\ell_1\ell_2}^{\mathrm{LM}} = \frac{1}{\sum_M \left(\sigma_{\mathcal{A}_{\ell_1\ell_2}^{\mathrm{LM}}} / K_{\ell_1\ell_2}^{\mathrm{LM}}\right)^2} \times \left[\sum_{\ell_1'\ell_2'} \frac{1}{\sum_M \left(\sigma_{\mathcal{A}_{\ell_1'\ell_2'}^{\mathrm{LM}}} / K_{\ell_1'\ell_2'}^{\mathrm{LM}}\right)^2}\right]^{-1} . \tag{D.6}$$